MEASUREMENT OF THE HALF-LIFE OF ^{60}FE FOR STELLAR AND EARLY SOLAR SYSTEM MODELS USING THE DIRECT DECAY OF ^{60m}CO AND ACCELERATOR MASS SPECTROMETRY

A Dissertation

Submitted to the Graduate School
of the University of Notre Dame
in Partial Fulfillment of the Requirements
for the Degree of

Doctor of Philosophy

by

Karen Marie (Chamberlin) Ostdiek

Philippe Collon, Director

Graduate Program in Physics
Notre Dame, Indiana

July 2016

MEASUREMENT OF THE HALF-LIFE OF ^{60}FE FOR STELLAR AND EARLY SOLAR SYSTEM MODELS USING THE DIRECT DECAY OF ^{60m}CO AND ACCELERATOR MASS SPECTROMETRY

Abstract

by

Karen Marie (Chamberlin) Ostdiek

Radioisotopes, produced in stars and ejected through core collapse supernovae (SNe), are important for constraining stellar and early Solar System (ESS) models. The presence of these isotopes (specifically ^{60}Fe) can identify progenitors of SNe, give evidence for nearby SNe, and can be used as a chronometer for ESS events. The ^{60}Fe half-life, which has been in dispute in recent years, can impact calculations for the timing of ESS events, the distance to nearby SNe, and the brightness of individual, non-steady state ^{60}Fe γ ray sources in the Galaxy. To measure such a long half-life, one needs to simultaneously determine the number of atoms in, and the activity of, an ^{60}Fe sample. We have undertaken a half-life measurement at the University of Notre Dame. This thesis gives results of both an activity measurement and an Accelerator Mass Spectrometry (AMS) measurement on an ^{60}Fe sample. This is the first time that the AMS technique is coupled with the direct isomeric day of ^{60}Co instead of the ground state decay of ^{60}Co. The resulting half-life from this work is (2.55 ± 0.15) million years, agreeing with the two most recent measurements. This is substantially longer than the previously accepted value of (1.49 ± 0.27) million years published in 1984.

"They're fireflies. Fireflies that, uh... got stuck up on that big bluish-black thing."

-Timon

"Oh, gee. I always thought they were balls of gas burning billions of miles away."

- Pumbaa

J.M.J.

Saint Albert, patron of scientists, pray for us.

To my parents and my husband.

CONTENTS

FIGURES v

TABLES xv

CHAPTER 1: INTRODUCTION TO RELEVANT NUCLEAR ASTROPHYSICS AND ^{60}FE 1
1.1 The Birth of Nuclear Astrophysics 1
1.2 Nucleosynthesis Beyond the Iron Peak 2
1.2.1 S-Process 7
1.2.2 R-Process 11
1.3 Observations and Implications of ^{60}Fe in the Galaxy 13
1.3.1 γ-ray Emission Lines 14
1.3.2 Low ^{60}Ni Abundances in early Solar System Meteorites 16
1.3.3 Spike in ^{60}Fe Concentration in Ocean Crust, Lunar, and Microfossil Samples 16
1.4 Past Half-Life Measurements 17
1.5 Measuring Half-Lives on the Order of Millions of Years 22

CHAPTER 2: FIRST ATTEMPT WITH MSU-PRODUCED ^{60}FE SAMPLE 27
2.1 ^{60}Fe Sample Production 27
2.2 Determining Isotopic Concentrations of the MSU Sample 34
2.3 Activity Measurement 38

CHAPTER 3: PRODUCTION OF THE PSI ^{60}FE SAMPLE 43

CHAPTER 4: ACCELERATOR MASS SPECTROMETRY FOR ^{60}FE 48
4.1 Beginnings of Accelerator Mass Spectrometry 48
4.2 AMS at University of Notre Dame 50
4.2.1 Source of Negative Ions via Cesium Sputtering (SNICS) Ion Source 50
4.2.2 Low Energy (LE) Magnet 55
4.2.3 FN Van de Graaff Tandem Accelerator 56
4.2.4 Analyzing Magnet 61
4.2.5 Wien Filter and the Second Carbon Stripper Foil 61
4.2.6 Gas Filled Magnet (GFM) Mode 65

4.2.7 Particle Identification . . . 68
4.2.7.1 Parallel Grid Avalanche Counter (PGAC) . . . 69
4.2.7.2 Ionization Chamber (IC) . . . 72
4.2.8 GFM and Detector Settings . . . 75
4.2.8.1 Optimizing for Spatial Separation . . . 76
4.2.8.2 Optimizing for Energetic Separation . . . 78
4.3 Measurement Method and Results for the November 2015 Experiment 84
4.3.1 Second Attempt during the May 2016 Experiment . . . 88

CHAPTER 5: GAMMA RAY ACTIVITY MEASUREMENT . . . 98
5.1 Decay Scheme for ^{60}Fe . . . 98
5.2 Experimental Setup . . . 101
5.2.1 Gamma Ray Interactions . . . 101
5.2.2 High Purity Germanium Detectors . . . 105
5.2.3 Low Background Counting Station . . . 108
5.2.3.1 Selection of Lead Brick . . . 109
5.2.3.2 Efficiency Measurements . . . 111
5.3 Background Considerations . . . 112
5.4 Measurement Method and Analysis . . . 117
5.4.1 Measurement Method . . . 117
5.4.2 Example Spectra and Results . . . 118

CHAPTER 6: CONCLUSION . . . 120

APPENDIX A: ELECTRONICS . . . 125
A.1 Signals from LL, LR, RL, and RR . . . 125
A.2 Signals from the Left and Right Anodes . . . 125
A.3 Gate and Delay Generator . . . 126
A.4 Pile Up Rejection (PUR) . . . 126

APPENDIX B: CHEMISTRY AND TIMELINE FOR MSU PRODUCED ^{60}FE SAMPLE . . . 134

APPENDIX C: ACCELERATOR MASS SPECTROMETRY DATA . . . 139

APPENDIX D: ACTIVITY DATA . . . 142

BIBLIOGRAPHY . . . 144

FIGURES

1.1 Binding Energy per nucleon as a function of mass number. It is energetically favorable to move toward the largest binding energy per nucleon possible. Stellar burning processes will fuse lighter nuclei up toward the iron peak. The iron peak refers to the mass region around iron that has the highest binding energy per nucleon. Figure from [26]. 3
1.2 Hydrogen burning cycles including the pp chains and the CNO cycles. 4
1.3 Stable isotopes and approximate nucleosynthesis paths as proton number, Z, versus neutron number, N. Stable and metastable elements are shown as black circles. The line of stable isotopes forms a valley which unstable nuclei will decay back towards. This valley is then referred to as the valley of nuclear stability. The s-process path is shown as a black line near the stable isotopes and ends at ^{209}Bi. The limit of the r-process is shown with lined-regions. Various magic numbers are indicated along with the respective proton and neutron numbers. Figure from [26]. 6
1.4 Evolution of an Asymptotic Giant Branch star.[3] Luminosity in solar units is plotted along the y-axis and the temperature of the star is plotted along the x-axis. The approximate time spent in each stage for our Sun is shown above the diagram. 7
1.5 Qualitative cross sections of a star in different stages. The top left is a star on the main sequence, burning hydrogen in its core. The top right is a Red Giant star that has built up an inert helium core from the ashes of the hydrogen shell burning. The bottom left is a star on the horizontal branch and is burning helium in the core and hydrogen in a shell around the core. The bottom right is an AGB star that has amassed an inert carbon-oxygen core from the ashes of helium burning [2]. 8
1.6 Thermal Pulses in an AGB star, including the ^{13}C pocket that is set up between thermal pulses [22]. The y-axis is mass, moving out from the core of the AGB star. The x-axis is time in the star's cycle. The different layers and burning processes are highlighted. TP refers to the Thermal Pulse and TDU refers to the Third Dredge Up process that pulls carbon from the core to the region between the helium and hydrogen burning shells. It is in this region that the reaction $^{13}\mathrm{C}(\alpha,\mathrm{n})^{16}\mathrm{O}$ can take place and act as a neutron source for the s-process. 10

1.7 Structure and evolution for a 25 $M_\odot$ star of solar metallicity [22]. The left side of the image shows the star before the core collapse and the right side is after the explosion. Main layer constituents are shown with minor constituents in black boxes and nucleosynthesis processes in thick green boxes. Layers are separated by thin blue lines and the burning process for each layer is shown along the bottom. The subscripts for each layer are as follows: C is core burning, S is shell burning, and X is explosive burning. The inner dashed black line is the predicted boundary of mass that falls in on the core. The outer dashed line is the boundary between mass that is ejected and mass that is retained after the supernova explosion. The mass that is retained becomes part of the eventual neutron star that is left over. 11
1.8 Solar System abundances normalized to silicon as a function of mass number, A. [22]. Some isotopes are highlighted at abundance peaks. . 12
1.9 Proton number, Z, as a function of neutron number, N. Figure from [13]. Boxes indicate elements that are stable or metastable. The s-process path is shown in blue and the r-process in red. Some isotopes can only be reached, or created, via the s-process and some only by the r-process. As isotopes made during the r-process decay back toward stability, they will end at the most neutron-rich stable isotope. These isotopes can be far enough away that the s-process can not reach them. There are many isotopes that can be produced by both however, shown in purple. There are also isotopes on the proton-rich side of the valley of nuclear stability. The process to create these isotopes, called the p-process, is not fully understood and is beyond the scope of this thesis. 13
1.10 Combined spectra of the ^{60}Fe signal in the inner Galaxy. This is a superposition of single and multiple events in the spectrometer on INTEGRAL for both 1173 and 1332 keV emission lines in the decay of ^{60}Fe [49]. 15
1.11 Image of the distribution of the emission line of ^{26}Al (1805-1813 keV) as measured by the spectrometer aboard the spacecraft INTEGRAL. Figure from [9]. The image resolution is 6 degrees full width at half the maximum. The emission lines of ^{26}Al are mostly confined to inner Galaxy disk with an estimated flux of 3.5×10^{-4} photons per centimeter squared per second. 15
1.12 ^{60}Fe/Fe concentration versus the ocean crust layer age [23]. The background level is at 2.4×10^{-16} as indicated by the dashed line. Horizontal error bars are the time interval covered by the layer and the vertical error bars are a confidence level of 68.3%. 17
1.13 Mass relationships and energy levels of isobars at mass number 60 as suggested by [39] in 1957. 18

1.14 Currently accepted, full decay scheme for ^{60}Fe. Thick white arrows indicate decays that happen more prevalently (100% or almost 100% for each) and grey dashed arrows indicate other possible decays that occur. The decay of the 2+ state in ^{60}Co was used for the first experiment [39]. The two γ ray lines in the excited states of ^{60}Ni were used for all other past measurements [28] [40] [47]. 19
1.15 Flow chart of the plan for the sample produced at Michigan State University (MSU). In the end, the concentration of ^{60}Fe would be measured at the University of Notre Dame and the concentration of ^{55}Fe at the Vienna Environmental Research Accelerator Laboratory. This experiment ultimately failed due to the activity of the MSU sample. 25
1.16 Flow chart of the plan for the sample produced at the Paul Scherrer Institute (PSI). This sample has been measured both by our group and the group from the Australian National University (ANU) lead by Anton Wallner who published in 2015 [47]. 26

2.1 The A1900 mass fragment separator at the National Superconducting Cyclotron Laboratory at Michigan State University for magnetically filtering unwanted particles out of the beam. The elements in red are 40 different multipole magnets and the elements in green are four dipole magnets. The production target is located at "TA." Images 1, 2, and 3 are denoted with "I1", "I2", and "I3" respectively. The focal plane is located at "FP." [19]. 28
2.2 Energy loss as a function of time of flight as measured at the focal place of the A1900 mass fragment separator using LISE++ simulations. Each peak represents a different isotope that is produced by the reaction of a high energy ^{64}Ni beam on a beryllium target. By setting the beam elements of the A1900 mass fragment separator, one isotope can be selected and all others filtered out of the beam. 29
2.3 Detector Set-up at the Focal Plane of the A1900 mass fragment separator. This includes position (with the parallel plate avalanche counters, PPACs), time of flight (timing scintillator), energy loss (PIN detector), and total energy (scintillator). Each component from the schematic is also pointed out in a picture on the bottom left. 30
2.4 The silicon detector, located on the right side of this picture, used to monitor scattered light particles from the stopper. The beam comes from the right side of the picture and the silicon detector is at backwards angles. 32
2.5 Schematic of the facilities at the Vienna Environmental Research Accelerator Laboratory. Source 2 was used for the ^{55}Fe measurement and a small ionization chamber was placed on the PIXE-ART beam line for particle identification. 37

2.6 Four hour backgrounds with the 50% HPGe detector with (red) and without (blue) two layers of lead bricks to reduce the room background radiation. The expected count rate for the MSU sample is shown in black at energies of 1173 keV and 1332 keV. This count rate from the MSU sample, assuming a detection efficiency of 1%, would be less than one count per four hours. 40
2.7 Zoomed in version of the Figure 2.6 on the region of interest. The background over a four hour time period is shown in red and the expected counts from the sample are in black. The expected count rate from the MSU sample is below the background rate for this detector and lead castle setup. 40

3.1 Evaporation process for the liquid Fe-1 Sample to make it into a point source for the activity measurement. 45

4.1 Differences in mass spectrometry and accelerator mass spectrometry. The major difference comes from the use of a particle accelerator which boosts the particles of interest to higher energies than attained in mass spectrometry. This allows experimenters to use other filtering and detection techniques not available at lower energies in order to make particle identification in terms of mass and proton number. Illustration edited from [1]. 50
4.2 A schematic of the layout at the Nuclear Science Laboratory on the campus of the University of Notre Dame. Only components important to Accelerator Mass Spectrometry experiements are shown. Inset: A detailed internal view of the accelerator, courtesy Bradley Mulder. . . 51
4.3 Drawing of an aluminum cathode used in the SNICS ion source. The desired material is pressed tightly into the cavity shown which has a depth of 0.125 inches and a diameter of 0.075 inches. 52
4.4 Schematic of the Source of Negative Ions via Cesium Sputtering (SNICS) ion source, courtesy of National Electrostatics Corporation. 53
4.5 Technical schematic of the FN accelerator at the NSL. Inset is a zoomed in portion focused in on the midplane, halfway between the terminal and the high energy base where the second stripper compartment is located. 57
4.6 Percent Abundance for each charge states at a given accelerator terminal voltage for ^{56}FeO which breaks up in the first carbon stripper foil. As the terminal voltage increases the peak of the distribution of charge states also increases. The 2nd Stripper data set is the probability of available charge states when the 9+ charge state from the first stripper is selected for a terminal voltage of 8.3 MV. By using the second carbon foil, higher charge states are available but the overall percentage of the beam in those charge states is lower, therefore sacrificing total beam current. 59

4.7 Final probability of possible beam energies from the second carbon stripper foil in the Tandem accelerator for ^{56}FeO which breaks up in the first carbon stripper foil. Each set of data is the distribution of energy for a given charge state from the first carbon foil. For example the solid black line is the final probability for a beam with a 9+ charge state from the first carbon foil. For comparison, single stripper data is shown in blue and uses the right y-axis. 60

4.8 Schematic of the principles of a Wien Filter. An electric and magnet field are perpendicular to each other and to the direction of the particle's velocity. Particles that pass through this region will feel a force. If the particle's velocity is equal to the electric field divided by the magnetic field, the particle will pass through undeflected. Otherwise, the particle will be pushed up or down out of the beam, where it can be blocked by slits further downstream. Image taken from [38]. 62

4.9 An example spectra from the silicon detector in the scattering chamber on the AMS beamline using a second stripped beam. The y-axis is counts per bin and the x-axis is energy deposited in the silicon detector in channels. The Wien filter is off. Each peak is a different charge state combination that pass through the analyzing magnet. The peak centered around channel number 3000 is our peak of interest at an energy of 112.86 MeV. 64

4.10 An example spectra from the silicon detector in the scattering chamber on the AMS beamline using a second stripped beam with the Wien filter turned on. The y-axis is counts per bin and the x-axis is energy deposited in the silicon detector in channels. The Wien filter will only allow one combination of charge states to pass through. The other combinations are bent away and filtered out of the beam. 64

4.11 Illustration of the Gas-Filled Magnet Technique used to filter out isobaric contaminants. When two isobars pass through the magnetic field of the spectrograph magnet, both will follow a similar path as they have the same charge state, mass, and energy (A). When the isobars pass through a thin mylar plastic window, they undergo charge exchange and split into several different charge states. However, they still follow similar path through the magnetic field (B). Further, when the magnetic field region is filled with a low pressure gas (N_2) as well, then the two isobars undergo more charge exchange with the gas and coalesce around a mean charge state (C). The resulting mean charge state for each isobar is related to the number of protons and therefore each isobar would take a different path through the magnet. Figure courtesy Matthew Bowers. 68

4.12 Schematic of the Parallel Grid Avalanche Counter and Ionization Chamber used for Accelerator Mass Spectrometry measurements. a) Approximate positions for grids, anodes, cathodes, and mylar windows for both detectors. b) Dimensions for both detectors in centimeters. Note: The IC and PGAC are separated by an extra 0.635 cm by an addition aluminum piece that isolates the two with a mylar foil [38]. . 71
4.13 How the PGAC generates a position signal [38]. The anode is used as the start signal and the delayed signals from the position grid are used as the stop signal. The signal generated in the position grid is sent in two separate directions, to the right and to the left as shown. The difference in the time for each of these two signals results in the position of the event. As shown here, the event generates a signal that goes to the right, with a delay of 95 nanoseconds and a second signal going to the left, with a delay of 85 nanoseconds plus an additional 180 nanoseconds to return to the right. The difference then relates to the physical position of the event. 72
4.14 Example of a typical Bragg Curve, where dE/dx, the rate of the energy loss, is plotted as a function of distance into an absorbing medium [24]. The plot shows the behavior of a single particle and a beam of particles of the same initial energy. The difference in the two is due to energy straggling, which comes from the statistically random energy loss due to interactions between the beam particles and the absorbing medium. 74
4.15 Placement of Anode, Cathode, and Frisch Grid for an Ionization Chamber. This configuration ensures that all incoming particles pass between the Frisch Grid and the Cathode. All of the electrons will cross the Frisch grid, held at ground, and travel the same voltage drop from the Frisch grid to the anode where the signal is generated. This makes the signal independent of the original position of the event. [24] . . . 75
4.16 Energy loss in the first anode, dE1, (y-axis) versus position (x-axis), both in channels, for ^{58}Ni and ^{58}Fe. By using the GFM technique, nickel and iron will take slightly different paths through the spectrograph magnet and will register different positions on the PGAC detector. The gap in the ^{58}Ni beam comes from the gap between the two halves of the PGAC detector. 76

4.17 Focal-plane position spectra for ^{58}Ni ions with an incident energy of 350 MeV measured with an Enge split-pole magnetic spectrograph at Argonne National Laboratory filled with nitrogen at different pressures as specified. Image taken from [36]. Following the individual plots from (a) in the upper left corner to (k) in the lower right corner, the pressure in the spectrograph magnet is increased. Once the pressure is high enough (d), the individual charge states will coalesce around a mean charge state. Increasing the gas pressure further will narrow the peak as the charge is more focused around the mean charge state. The peak will begin to broaden again as shown in (k). This results from the competition between narrowing due to the higher number of collisions with the gas particles, causing a better statistical averaging of the trajectories and the broadening due to small angle scattering and energy loss straggling. 78
4.18 Simulated Bragg curves from the program SRIM for nickel and iron in the IC with an incoming energy near 60 MeV. Energy loss is on the y-axis in units of MeV/mg/cm^2 and distance through the gas in millimeters is on the x-axis. Nickel is shown in orange and iron is shown in blue. The thickness of the lines indicate the errors in the simulation. Toward the lower ranges of energy, the simulation from SRIM is not as accurate and errors are large. From this, we can expect nickel to have a higher rate of energy loss in the first part of the IC and iron to have a higher rate later in the IC. This leads to the concept of crossover, or the point where nickel and iron are losing at the same rate. 79
4.19 Example spectra showing the crossover technique. For both spectra, the y-axis is energy loss in channels and the x-axis is position in channels. The left spectra is the energy loss in anode 1 (dE1) and the right spectra is the energy loss in anode 3 (dE3). In dE1, nickel is losing energy faster than iron and in dE3, iron is losing faster than nickel. Note, that the gains for the preamplifiers are different between dE1 and dE3, so the energy loss is not to scale. This example is for mass 58 but this is a good approximation of the behavior observed at mass 60. 80
4.20 Example background spectra from a blank sample (material that contains no ^{60}Fe). Top: Spectrum for dE1 (y) versus position (x) of blank material. Part of the ^{60}Ni peak is blocked by an aluminum plate, located before the PGAC. The location for ^{60}Fe is highlighted. Middle: Spectrum for dE3 (y) versus position (x) for the same material. The location of ^{60}Fe is highlighted. Bottom: Spectrum of the energy loss in dE1 plus dE2 (y) versus the energy loss in dE3 (x). The cuts from dE1 and dE3 have been applied and only four counts pass these cuts for this sample. The background concentration is measured as approximately 2×10^{-12}. The regions of interest for each spectrum were determined from the Fe-1 sample as illustrated in Figure 4.21. 82

4.21 Example spectra for the Fe-1 sample, which contains the highest $^{60}Fe/^{56}Fe$ concentration of all of our samples. Top:Spectrum for dE1 (y) versus position (x) of the Fe-1 sample. Part of the ^{60}Ni peak is blocked by an aluminum plate, located before the PGAC. The location of the ^{60}Fe is highlighted. Middle: Spectrum for dE3 (y) versus position (x) for the same material. The location of ^{60}Fe is again highlighted. Bottom: Spectrum of the energy loss in dE1 plus dE2 (y) versus the energy loss in dE3 (x). The locations of the ^{60}Ni and the ^{60}Fe peaks are highlighted. The cuts used for the analysis are based off of runs on the Fe-1 sample due to the prevalence of the ^{60}Fe peaks. 83

4.22 Example spectra showing the crossover technique. For the top two spectra, the y-axis is energy loss in channels and the x-axis is position in channels. The left spectra is the energy loss in anode 1 (dE1) and the right spectra is the energy loss in anode 3 (dE3). In dE1, nickel is losing energy faster than iron and in dE3, iron is losing faster than nickel. Note, that the gains for the preamplifiers are different between dE1 and dE3, so the energy loss is not to scale. The bottom spectrum is the energy loss in anode 1 and anode 2 (dE1 + dE2) versus the energy loss in anode 3 (dE3). 93

4.23 Example spectra for the Fe-4 sample. For the top two spectra, the y-axis is energy loss in channels and the x-axis is position in channels. The left spectra is the energy loss in anode 1 (dE1) and the right spectra is the energy loss in anode 3 (dE3). Bottom: Spectrum of the energy loss in dE1 plus dE2 (y) versus the energy loss in dE3 (x). The locations of the ^{60}Ni and the ^{60}Fe peaks are highlighted. The cuts used for the analysis are based off of runs on the Fe-1 sample due to the prevalence of the ^{60}Fe peaks. 94

4.24 Example spectra for the Fe-1 sample, which contains the highest $^{60}Fe/^{56}Fe$ concentration of all of our samples. For the top two spectra, the y-axis is energy loss in channels and the x-axis is position in channels. The left spectra is the energy loss in anode 1 (dE1) and the right spectra is the energy loss in anode 3 (dE3). The location of ^{60}Fe is highlighted. Bottom: Spectrum of the energy loss in dE1 plus dE2 (y) versus the energy loss in dE3 (x). The locations of the ^{60}Ni and the ^{60}Fe peaks are highlighted. The cuts used for the analysis are based off of runs on the Fe-1 sample due to the prevalence of the ^{60}Fe peaks. 95

5.1 Decay Scheme of ^{60}Fe. Thick open lines indicate the most probable decays, both β decays and gamma ray decays. Dotted lines indicate other possible decays that occur with a branching ratio of less than 0.25% [10]. 99

5.2 Relative Importance of the three major γ ray interactions, minus Coherent Scattering [24]. Solid lines indicate where the neighboring interactions are equivalent. 103

5.3 The effects of a junction between n-(donor) and p-(acceptor) types of semiconductor material. Top: the concentrations of the both types in a p-type semiconductor that has been exposed to a vapor of an n-type material. N_D is the resulting donor profile and N_A is the resulting acceptor profile. The variation of equilibrium charge carrier concentration is labeled as n and p for conduction electron and hole concentration respectively. n_i and p_i are for an intrinsic material, or one where the holes and conduction electrons are equal. Bottom: profiles for the space charge $\rho(x)$, electric potential $\varphi(x)$, and the electric field $\varepsilon(x)$. The effects of the charge diffusion across the junction lead to these profiles [24]. 106

5.4 Lead Castle Construction with Interior View. The dark blue bricks are the bottom two layers. The green bricks are the side layers. The bricks surround the detector stems had half circles cut out in order to surround the detector stems fully. The dark- and light-gray bricks are the top two layers, supported in place by an aluminum sheet (not shown). The light-gray bricks are connected together for easy access to the inside. 110

5.5 1 day runs on the Fe-1 ^{60}Fe sample and the background. Counts per bin are on the y-axis and energy in keV is on the x-axis. For the sample data, the background continuum is shifted slightly upward. The background subtraction technique described later in this section, accounts for this shift. 113

5.6 Full spectra of Fe-1 sample, with and without plastic for a beta absorber. Measurements were taken for one day each. Counts per bin are on the y-axis and the energy in keV is on the x-axis. Note the reduction specifically in the lower energy gamma rays and X rays (below 20 keV). 114

5.7 Zoomed in on the region of interest for the Fe-1 sample, with and without the plastic beta absorber. Counts per bin are on the y-axis and energy in keV is on the x-axis. The measurement of each was taken over one day. The difference between the two spectra is subtle however the spectra without the plastic (orange) has slightly higher counts per bin on either side of the peak of interest at 58 keV than the spectra with the plastic (blue). 114

5.8 Continuum Subtraction Example on 48 hour measurement on the Fe-1 Sample shown as counts (y) as a function of energy in keV (x). Each panel contains the same data. The progression of the panels illustrates the subtraction technique. In A, the max of the peak is defined as the centroid. The full peak is ±1.5 keV from the max. The background continuum is defined from ± 1.5 keV to ± 3.0 keV from the max. In B, the average counts per channel on the left and the right is found (solid line) and a line is defined between the two averages (dashed line). In C, the area below the line connecting the two averages is subtracted out from the total area in the full peak. This, then, gives the corrected counts in the peak. 116
5.9 24-hour runs on the Fe-1 sample (in red) and the background (in blue). Counts per bin are on the y-axis and energy in keV is on the x-axis. Note the background peak at 63 keV. This peak is from the decay of ^{234}Th in the ^{238}U decay chain. This peak is well separated from our peak of interest but can act as a good test of the background subtraction technique. 118

6.1 The previous four ^{60}Fe half-life measurements, including this work in grey. Our work overlaps with Rugel, et al. in blue with a half-life of (2.62 ± 0.04) million years and with Wallner, et al. in green with a half-live of (2.50 ± 0.12) million years. Our work also does not agree with the previously accepted value from Kutschera, et al. in orange of (1.49 ± 0.27) million years. 121

A.1 Position Signals and Scalers schematic for the Accelerator Mass Spectrometry (AMS) electronics set up. Shown here are the position signals and the PGAC anode signals used for online scalers and timing. Figure courtesy William Bauder. 128
A.2 Gating and Energy Signals for the AMS electronics set up. Shown here are the gates based on the position and Silicon detector signals. Also shown are the energy signals from the Ionization Chamber. Figure courtesy William Bauder. 130
A.3 Pile Up Rejection schematic for the AMS electronics set up. Figure courtesy William Bauder. 132

TABLES

2.1 SAMPLES PRODUCED AT THE MSU NSCL IN JANUARY 2009 . 33
2.2 EXPECTED AND MEASURED ^{55}FE/^{56}FE CONCENTRATIONS FOR THE STANDARD, A0, AND TWO UNKNOWN SAMPLES 38
2.3 TEST OF THE BACKGROUND RADIATION WITH TWO NAI(TL) DETECTORS 42

3.1 DILUTION SERIES FOR ^{55}FE BETA ACTIVITY (LSC) AND THE ^{55}FE/^{56}FE ATOM-RATIO MEASUREMENTS (AMS) 47

4.1 SETTINGS FOR SNICS DURING THE NOVEMBER 2015 EXPERIMENT 55
4.2 MULTIPLE TERMINAL VOLTAGE AND CHARGE STATE COMBINATIONS WERE TESTED GIVING A VARIETY OF ENERGIES FOR MASS 60 61
4.3 WIEN FILTER SETTINGS FOR THE ELECTRIC PLATES AND THE MAGNETIC FIELD FOR EACH OF THE THREE MASSES OF IRON ISOTOPES 65
4.4 SPECTROGRAPH MAGNET SPECIFICATIONS 66
4.5 GFM AND DETECTOR NOVEMBER 2015 SETTINGS INCLUDING GAS PRESSURES AND DETECTOR VOLTAGES 84
4.6 RAW DATA FROM THE EXPERIMENT IN NOVEMBER 2015 . . 87
4.7 SETTINGS FOR SNICS DURING THE MAY 2016 EXPERIMENT 90
4.8 WIEN FILTER SETTINGS DURING THE MAY 2016 EXPERIMENT FOR THE ELECTRIC PLATES AND THE MAGNETIC FIELD FOR EACH OF THE THREE MASSES OF IRON ISOTOPES . . . 91
4.9 GFM AND DETECTOR FINAL SETTINGS DURING THE MAY 2016 EXPERIMENT INCLUDING GAS PRESSURES AND DETECTOR VOLTAGES 92
4.10 RAW DATA FROM THE EXPERIMENT IN MAY 2016 97

5.1 SPECIFICATIONS FOR BOTH HPGE PLANAR DETECTORS . . 108

6.1 QUANTITIES AND PERCENT ERRORS FOR THE ACTIVITY AND AMS MEASUREMENTS 122

C.1 RAW ACCELERATOR MASS SPECTROMETRY DATA FROM NOVEMBER 2015 140

C.2 RAW ACCELERATOR MASS SPECTROMETRY DATA FROM MAY 2016 141

D.1 DATA FOR THE ^{241}AM EFFICIENCY AND THE FE-1 ^{60}FE SOURCES143

CHAPTER 1

INTRODUCTION TO RELEVANT NUCLEAR ASTROPHYSICS AND ^{60}Fe

1.1 The Birth of Nuclear Astrophysics

Mankind has always seemed to have a fascination with celestial bodies. Our pursuit of knowledge about stars, planets, and galaxies, though fruitful, has led us to additional questions - none more important than "How did we get here?" A logical next question would involve the origin of the elements that make up the Sun, the Earth, and our own selves. With advances in science and technology, we are able to answer some of the questions surrounding the synthesis of the elements, creating more questions at the same time.

In 1920, it was proposed that the Sun's energy generation came from converting hydrogen to helium. The quantum mechanical probability for particles to tunnel through potential barriers was calculated in 1928 by Gamow and would later explain how stars are able to fuse elements at lower, observed stellar temperatures. From this, reactions of protons on lithium (1932) and carbon (1934) would be the first tested reactions of processes called the pp chain and the CNO cycle respectively. Further work in the late 1930s would establish both processes and calculate their energy generation. In 1952, Salpeter would suggest the triple α-process (^{8}Be + α) to bypass the gap in the stable elements between masses 5 and 8, and to produce ^{12}C. Due to the low probability of this reaction, Hoyle suggested that there must be a low lying 0+ excited state in ^{12}C for this reaction to happen at a significant rate. This state would be confirmed a year later. Further evidence of nucleosynthesis was found in peaks in

the solar system elemental abundances and in the discovery of technetium in red giant stars. Review papers such as the one published by Burbidge, Burbidge, Fowler, and Hoyle [12] (B^2FH) in 1957 gave a view of the current understanding of the processes to produce elements in the stars. During the next two decades after the B^2FH paper, over one hundred papers were published identifying the effects of nucleosynthesis in stellar spectra. Thus, the field of nuclear astrophysics was established.

This thesis aims to answer one of the many questions in nuclear astrophysics, namely "what is the half-life of the isotope ^{60}Fe." Motivation for answering that question is given in the remainder of this introductory chapter, concluding with a general overview of how an experiment can be performed to determine the half-life of ^{60}Fe.

1.2 Nucleosynthesis Beyond the Iron Peak

Isotopes with masses below iron are believed to have been made in the Big Bang (hydrogen, helium, and some lithium) and during the burning processes of stars (isotopes heavier than lithium). It is energetically favorable for these lighter mass elements to be fused together (i.e. an increase in binding energy per nucleon) as shown in Figure 1.1. Initially these burning processes will convert four protons into one helium atom. This conversion can happen with protons and other mass-one or mass-two isotopes (see Figure 1.2a) called the pp chain, or can involve heavier elements (such as carbon, nitrogen, and oxygen) reacting with protons (see Figure 1.2b), called the CNO cycle.

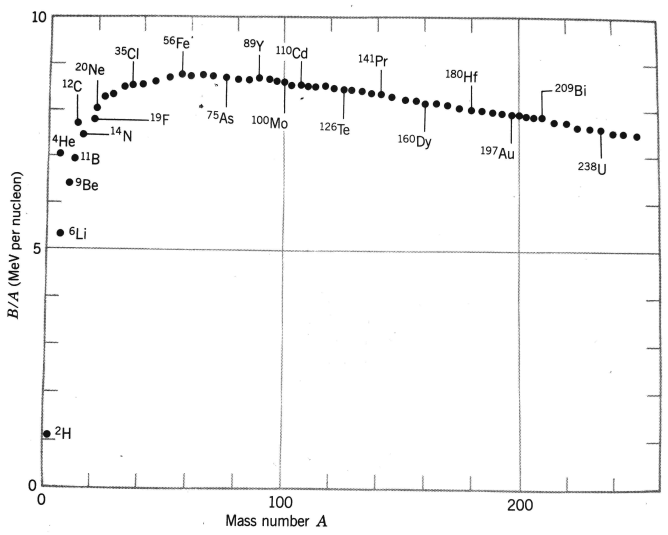

Figure 1.1. Binding Energy per nucleon as a function of mass number. It is energetically favorable to move toward the largest binding energy per nucleon possible. Stellar burning processes will fuse lighter nuclei up toward the iron peak. The iron peak refers to the mass region around iron that has the highest binding energy per nucleon. Figure from [26].

Nucleosynthesis processes beyond these initial burning cycles will begin to fuse together heavier isotopes, such as two carbon atoms or two oxygen atoms. Other processes will fuse α particles with heavier isotopes such as neon, sodium, and magnesium. The last burning process is silicon burning, where photodisintegration dominates over further fusion. In photodisintegration, an isotope absorbs a γ ray creating an excited state and then immediately decays by emitting a light particle (p, α, n). These liberated light particles will be recaptured, creating heavier, more tightly-bound elements with proton numbers around 24-26. This mass region is called the iron peak as it is has the highest binding energy per nucleon for any mass, as shown in Figure 1.1.

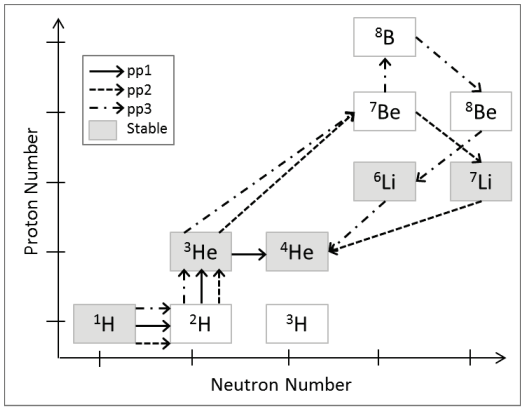

(a) pp chains which converts four protons into one helium atom. There are three proposed ways to complete this and they are referred to as the pp1, pp2, and pp3 chains. Stable elements are shown in grey boxes. Proton number is plotted on the y-axis with neutron number on the x-axis. Arrows mark the reactions that occur in the cycle and can be deduced from the change in proton and neutron number.

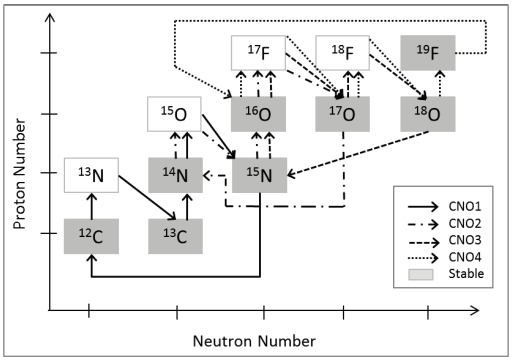

(b) CNO chains for converting four protons into one helium atom, four of which are illustrated here. Proton number is plotted on the y-axis and the neutron number is plotted on the x-axis. Stable elements are shown as grey boxes and arrows indicate the reactions that occur.

Figure 1.2. Hydrogen burning cycles including the pp chains and the CNO cycles.

Detailed descriptions of these processes below the iron peak can be found in standard textbooks such as [21]. Moving to heavier masses beyond the iron peak, energy is no longer gained by fusing nuclei together. Therefore, it is energetically unfavorable to make heavier elements by fusion.

Simplistically, heavier mass isotopes are produced through the addition of a proton or a neutron. Nuclei are made of protons and neutrons and therefore have an intrinsic positive charge. In order for an additional proton to move close enough to the nucleus, it must overcome a Coulomb barrier and to allow the strong force to dominate and capture the proton. Neutrons, however, are impervious to the Coulomb barrier because of their neutral charge. As the transmission for protons and alpha particles through the Coulomb barrier decreases drastically above the iron peak, the cross section, proportional to the probability of capture, for a neutron is unaffected.

The neutron has a finite amount of time to react and create heavier nuclei because of its 10.183 minute half life [42]. Because of this, there are not many free neutrons in the Interstellar Medium (ISM), the virtually empty space between stars. In the interior of stars, a nuclei-rich environment, neutrons have a higher chance of reacting and pushing the abundances past the iron peak. This can lead away from the valley of nuclear stability, or the stable isotopes that follow along a semi-straight line when plotted on a graph of proton number as a function of neutron number for all known isotopes.

The nuclear astrophysics community agrees that isotopic abundances suggest several different categories for neutron capture processes. The two dominant ones are the slow neutron capture process (s-process) and the rapid neutron capture process (r-process), each making roughly half of the elements heavier than iron.

The s-process occurs when it is more likely that a nucleus will decay via beta decay before capturing a neutron. There are two possible types of beta decay. In beta minus ($\beta-$) decay, a neutron decays to a proton plus an electron (historically called a beta

particle) and an antineutrino. Conversely, a beta plus ($\beta+$) decay transforms a proton into a neutron plus a positron (also referred to as a beta particle) and a neutrino. For both β- and $\beta+$ decays, the mass number stays the same. In the r-process, the nucleus is more likely to capture another neutron before beta decaying, with the possibility of pushing the abundance pattern far from stability. The approximate paths of these two processes are shown in Figure 1.3. The line of stable and metastable isotopes forms a valley that exotic nuclei decay back towards. In the next two sections, further details are given for both of these process.

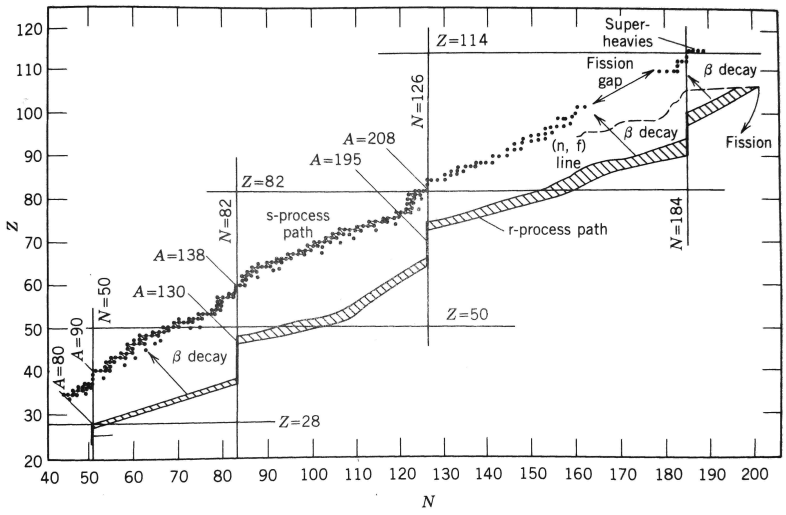

Figure 1.3. Stable isotopes and approximate nucleosynthesis paths as proton number, Z, versus neutron number, N. Stable and metastable elements are shown as black circles. The line of stable isotopes forms a valley which unstable nuclei will decay back towards. This valley is then referred to as the valley of nuclear stability. The s-process path is shown as a black line near the stable isotopes and ends at ^{209}Bi. The limit of the r-process is shown with lined-regions. Various magic numbers are indicated along with the respective proton and neutron numbers. Figure from [26].

1.2.1 S-Process

The s-process follows the valley of nuclear stability, building upon seed nuclei from the iron peak. This process eventually terminates at ^{209}Bi as it is the heaviest stable isotope. The s-process occurs when the beta decay constant, or the probability per unit time for the decay of the nucleus, is large compared to the neutron capture constant, or the probability per unit time for the nucleus to capture another neutron. This causes the path of the s-process to run close to stable isotopes.

One of the astrophysical sites for the s-process is believed to be in Thermal-Pulsing (TP) low-mass (1.5-3 $M_\odot$, where $M_\odot$ is the mass of our Sun) Asymptotic Giant Branch (AGB) stars. AGB stars start out as main sequence stars as shown in Figure 1.4, burning hydrogen in the core of the star through either the pp chains or the CNO cycle described above.

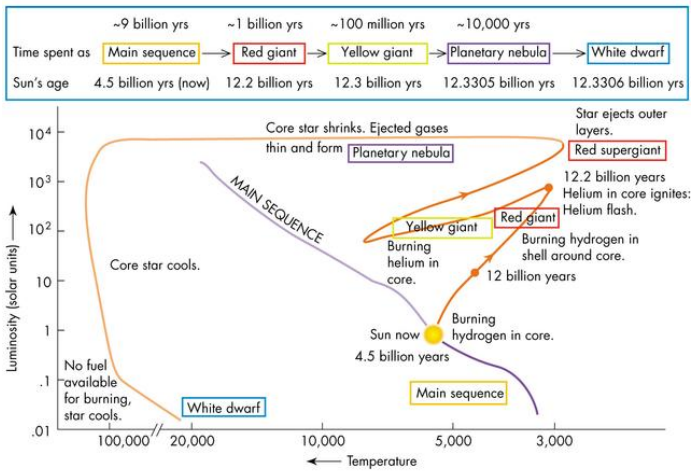

Figure 1.4. Evolution of an Asymptotic Giant Branch star.[3] Luminosity in solar units is plotted along the y-axis and the temperature of the star is plotted along the x-axis. The approximate time spent in each stage for our Sun is shown above the diagram.

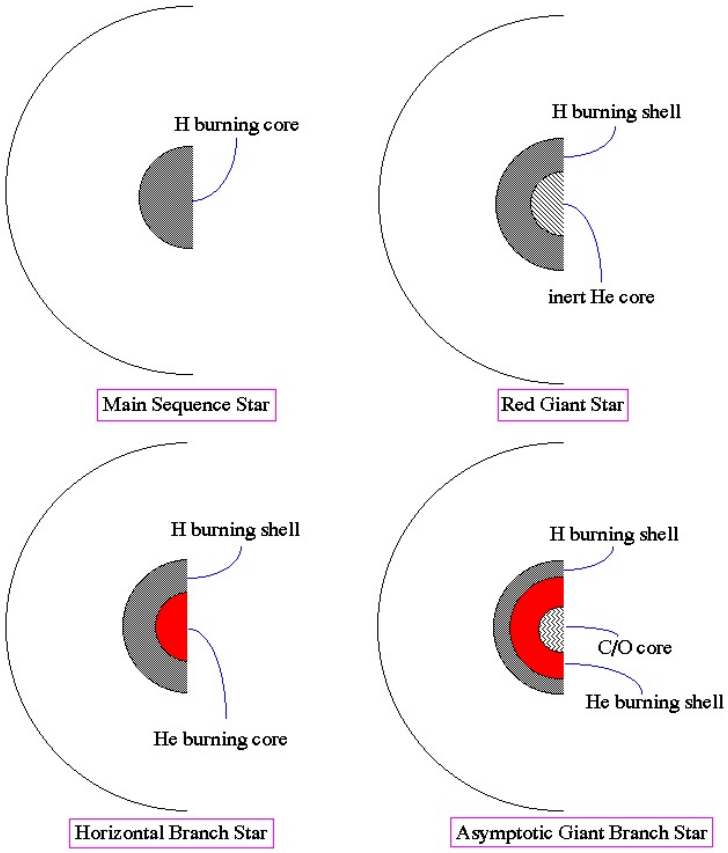

Figure 1.5. Qualitative cross sections of a star in different stages. The top left is a star on the main sequence, burning hydrogen in its core. The top right is a Red Giant star that has built up an inert helium core from the ashes of the hydrogen shell burning. The bottom left is a star on the horizontal branch and is burning helium in the core and hydrogen in a shell around the core. The bottom right is an AGB star that has amassed an inert carbon-oxygen core from the ashes of helium burning [2].

The ashes of hydrogen shell burning are helium and as they are dumped on the inert helium layer below the hydrogen shell, the mass of the helium layer will increase and the star is classified as a red giant star. Once the temperature is high enough in the inert helium core, the helium will ignite and start to burn. This burning will

expand the hydrogen shell outward, cooling it down and turning off the burning in the hydrogen shell. The main source of energy is then the burning from the helium layer. As the helium shell burning diminishes, the temperature will decrease and the hydrogen shell can begin burning again.

The back and forth between the two burning processes can keep repeating periodically until the star has exhausted its nuclear fuel. Each repeat is referred to as a thermal pulse (TP). Because of the energy flux of each TP, it is hypothesized that a convective zone will set up between the hydrogen and helium burning shells in the star. This zone will extend down into the star which has, by this time, become an AGB star and its core contains carbon as the product of helium burning. The convective zone can pull carbon closer to the star's surface (Figure 1.6). This sets up a ^{13}C pocket where the reaction $^{13}\mathrm{C}(\alpha, \mathrm{n})^{16}\mathrm{O}$ can take place, providing a neutron source for the s-process. AGB stars typically lose much of their outer envelope and end their cycle as a white dwarf (a small dense star) once the star runs out of nuclear fuel.

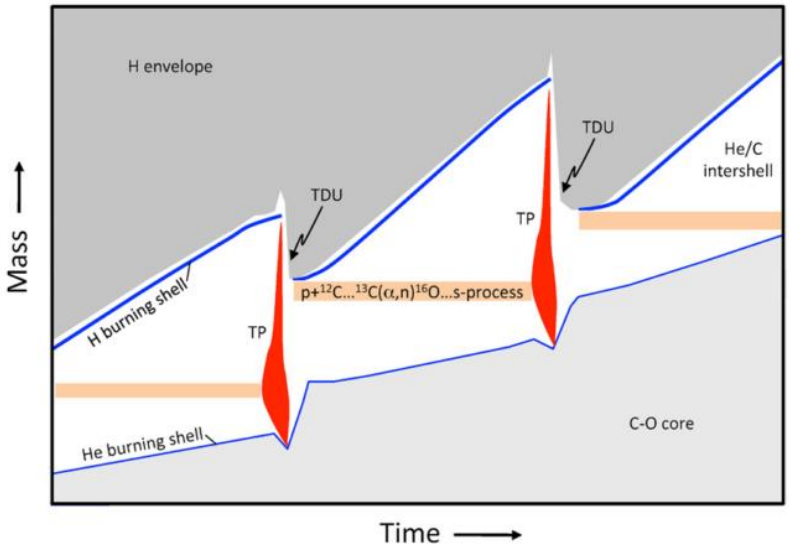

Figure 1.6. Thermal Pulses in an AGB star, including the ^{13}C pocket that is set up between thermal pulses [22]. The y-axis is mass, moving out from the core of the AGB star. The x-axis is time in the star's cycle. The different layers and burning processes are highlighted. TP refers to the Thermal Pulse and TDU refers to the Third Dredge Up process that pulls carbon from the core to the region between the helium and hydrogen burning shells. It is in this region that the reaction $^{13}\mathrm{C}(\alpha,\mathrm{n})^{16}\mathrm{O}$ can take place and act as a neutron source for the s-process.

Another possible site for the s-process is the core helium burning and carbon shell burning in massive stars, as shown in Figure 1.7 where the mass is M$\geq$ 13M$_\odot$ and the star has a high metalicity. Metalicity refers to the amount of "metals", elements heavier than hydrogen, present in a star. Stars built from the ashes of previous generations of stars typically have a higher metalicity. The higher the metalicity, the more likely the star is to have seed nuclei for the s-process. Here the reaction $^{22}\mathrm{Ne}(\alpha,\mathrm{n})^{25}\mathrm{Mg}$ will act as the neutron source for the s-process.

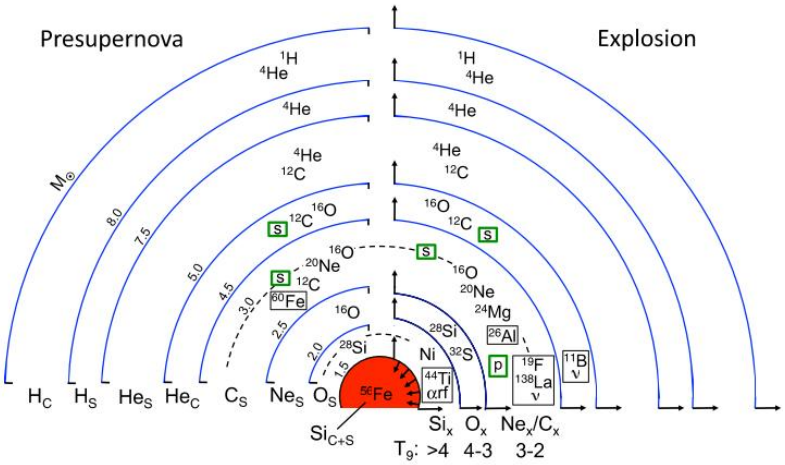

Figure 1.7. Structure and evolution for a 25 $M_{\odot}$ star of solar metallicity [22]. The left side of the image shows the star before the core collapse and the right side is after the explosion. Main layer constituents are shown with minor constituents in black boxes and nucleosynthesis processes in thick green boxes. Layers are separated by thin blue lines and the burning process for each layer is shown along the bottom. The subscripts for each layer are as follows: C is core burning, S is shell burning, and X is explosive burning. The inner dashed black line is the predicted boundary of mass that falls in on the core. The outer dashed line is the boundary between mass that is ejected and mass that is retained after the supernova explosion. The mass that is retained becomes part of the eventual neutron star that is left over.

1.2.2 R-Process

The Solar System isotopic abundances show two peaks near mass, A=130 and A=195 (see Figure 1.8) which can not be produced from the s-process as these nuclei are shielded (see Figure 1.9) from the s-process by radionuclei with short half-lives. However these peaks could be explained with another process, the r-process. With very high neutron densities ($N_n \geq 10^{21}$ cm^{-3}) and high temperatures (T$\geq$ 1 GK), elements can be produced far from stability on the neutron-rich side of the valley of

nuclear stability. When the flux of neutrons ends, the nuclei will beta decay back to the most neutron-rich stable (or metastable) isotope. As illustrated in Figure 1.9, the isotopes that the r-process decays to are farther enough from the valley of stability that the s-process could not reach them. These r-only isotopes are also about ten units of mass lower than the s-only isotopes. This could be an explanation for the dual peaks in abundance for all isotopes, specifically around A=130 with ^{118}Sn and ^{138}Ba and around A=195 with ^{195}Pt and ^{208}Pb. Producing r-process nuclides is hypothesized to occur by neutrino-driven wind from a neutron star resulting from a Type II SN, during a neutron star merger, or by the ejection of neutronized material in magnetized jets from asymmetric massive star explosions. However, these sites also have arguments against them. Much of the information about the r-process is still unknown as the necessary information such as masses, capture cross sections, and beta decay rates are currently inaccessible by experiment. Thus the r-process relies heavily on comparing theoretical models with observed abundances.

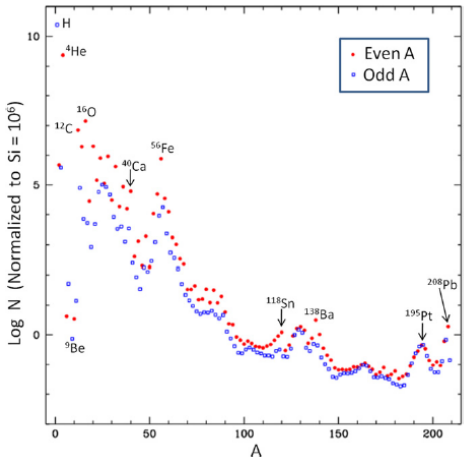

Figure 1.8. Solar System abundances normalized to silicon as a function of mass number, A. [22]. Some isotopes are highlighted at abundance peaks.

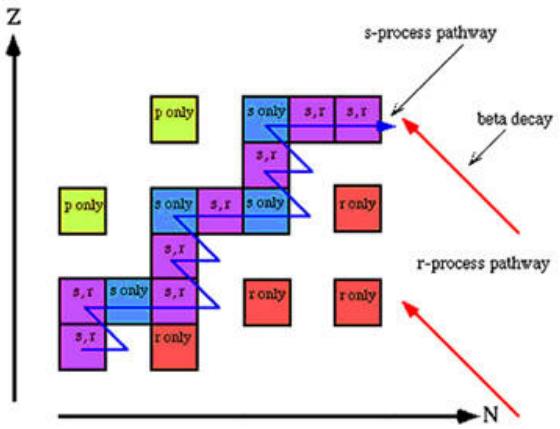

Figure 1.9. Proton number, Z, as a function of neutron number, N. Figure from [13]. Boxes indicate elements that are stable or metastable. The s-process path is shown in blue and the r-process in red. Some isotopes can only be reached, or created, via the s-process and some only by the r-process. As isotopes made during the r-process decay back toward stability, they will end at the most neutron-rich stable isotope. These isotopes can be far enough away that the s-process can not reach them. There are many isotopes that can be produced by both however, shown in purple. There are also isotopes on the proton-rich side of the valley of nuclear stability. The process to create these isotopes, called the p-process, is not fully understood and is beyond the scope of this thesis.

1.3 Observations and Implications of ^{60}Fe in the Galaxy

One isotope beyond the iron peak that is of interest is ^{60}Fe, which is classified as a s-process nuclide (described above in Section 1.2.1). It lies close to the valley of stability but is separated from its nearest stable iron isotope by radioactive ^{59}Fe. The neutron flux to create ^{60}Fe must be high enough to overcome the decay of ^{59}Fe but not so high as to immediately and completely destroy ^{60}Fe, creating ^{61}Fe. Such neutron densities are expected in massive stars, that end their cycles as a core collapse

supernova (CCSN), and AGB stars as discussed above in Section 1.2.1. CCSNe end their cycles in a violent explosion when the star's burning processes can no longer generate sufficient thermal pressure to resist the gravitational collapse. AGB stars will slowly lose their envelopes through hypothesized processes such as stellar winds. Therefore ^{60}Fe's natural production being exclusively isolated to within stars provides the opportunity to see ^{60}Fe throughout our Galaxy as both core collapse supernovae and AGB stars lose much of their total mass to the surrounding Interstellar Medium. The following are brief descriptions of three such observations of ^{60}Fe.

1.3.1 γ-ray Emission Lines

A first place we can observe the presence of ^{60}Fe is through the gamma rays that are emitted when it decays. In the decay of ^{60}Fe to the stable ground state of ^{60}Ni (described in more detail later, see Figure 1.14 or Chapter 5 for a detailed discussion of the decay scheme), two γ rays are emitted from the excited states in ^{60}Ni. These two lines are at energies of 1173 and 1332 keV and can be measured using High Purity Germanium (HPGe) detectors. By placing such detectors on a spacecraft, it is possible to observe the decay of isotopes such as ^{60}Fe and ^{26}Al in our Galaxy. One such spacecraft named INTEGRAL was launched in 2002, containing 19 HPGe detectors, with a scientific mission that included measuring the activity levels of ^{26}Al and ^{60}Fe in our own Galaxy. By looking back at our own Galactic plane where massive stars are formed, the INTEGRAL mission is able to see these emission lines above background, giving flux rates for both isotopes [49]. An example spectrum for ^{60}Fe is shown in Figure 1.10. With enough data, the Galactic plane can be mapped as was done with ^{26}Al. The flux rates of ^{26}Al are shown in Figure 1.11 from [9].

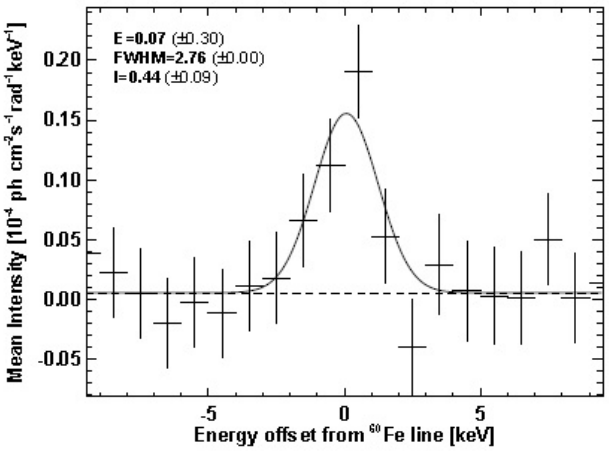

Figure 1.10. Combined spectra of the ^{60}Fe signal in the inner Galaxy. This is a superposition of single and multiple events in the spectrometer on INTEGRAL for both 1173 and 1332 keV emission lines in the decay of ^{60}Fe [49].

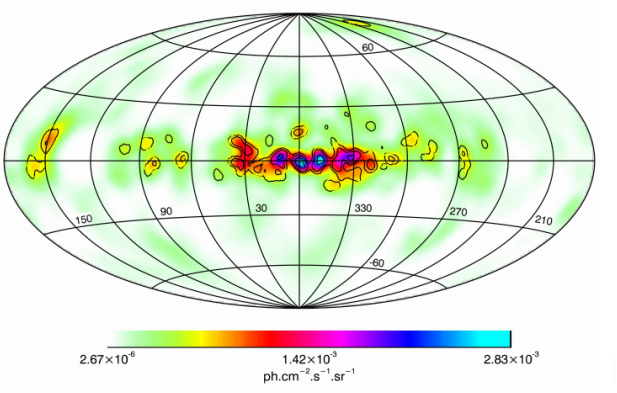

Figure 1.11. Image of the distribution of the emission line of ^{26}Al (1805-1813 keV) as measured by the spectrometer aboard the spacecraft INTEGRAL. Figure from [9]. The image resolution is 6 degrees full width at half the maximum. The emission lines of ^{26}Al are mostly confined to inner Galaxy disk with an estimated flux of 3.5×10^{-4} photons per centimeter squared per second.

1.3.2 Low ^{60}Ni Abundances in early Solar System Meteorites

A second place we see evidence of ^{60}Fe is in samples from Earth and Mars as compared to meteorites that would have formed within the first one million years of the Solar System (SS) formation. These old meteorite samples have ∼25 parts per million lower concentration of ^{60}Ni relative to ^{58}Ni than the younger samples from Earth and Mars [8]. As ^{60}Ni is the stable granddaughter product of the decay of ^{60}Fe, finding evidence of higher levels of ^{60}Ni in younger samples has suggested that ^{60}Fe was injected into the protoplanetary disk after SS formation.

1.3.3 Spike in ^{60}Fe Concentration in Ocean Crust, Lunar, and Microfossil Samples

A third place we observe ^{60}Fe is in ocean crust samples, as well as lunar samples and microfossils. Possible hints [6] [14] [15] [30] [31] [43] at a nearby SN explosion in the past several million years were recently confirmed by evidence of a spike in the concentration of ^{60}Fe in terrestrial samples. In ocean crust samples, a spike in the concentration of ^{60}Fe was observed [23]. The sample was dated to be approximately 2.8 million years old using ^{10}Be as the dating tool. Further work has been undertaken to measure ^{60}Fe in other ocean crust samples [17] [48] (the later finding an excess dating to 6.5-8.7 million years ago as well), lunar samples [16] and microfossil records [7]. Lunar samples are of interest as the Moon would have been exposed to the same ^{60}Fe debris from a nearby SN. However, the conditions of the Moon (a lack of an atmosphere means that meteorites will not burn up but will strike the surface of the Moon causing a mixing of the surface soil), the ^{60}Fe concentration can be more uniform over the depth of the material. Microfossils from Earth would provide a similar signature as ocean crust material as the fossils tested in [7] had been trapped in glaciers.

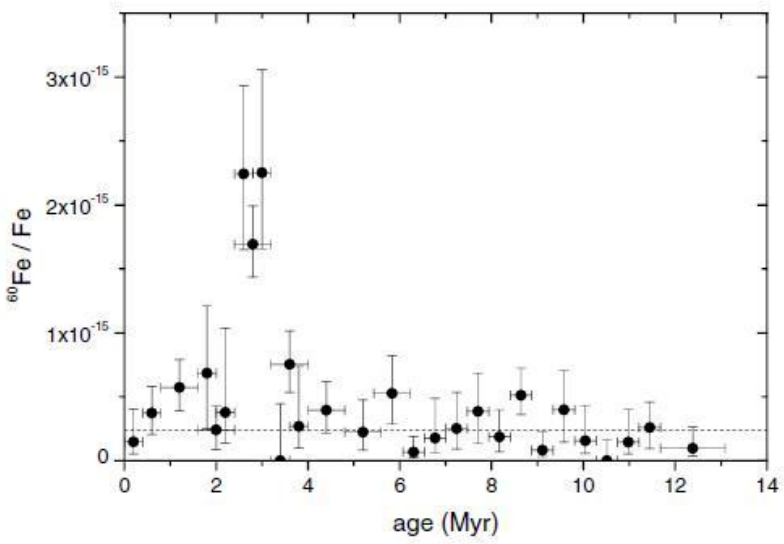

Figure 1.12. ^{60}Fe/Fe concentration versus the ocean crust layer age [23]. The background level is at 2.4×10^{-16} as indicated by the dashed line. Horizontal error bars are the time interval covered by the layer and the vertical error bars are a confidence level of 68.3%.

1.4 Past Half-Life Measurements

With the possibility of using long-lived radioisotopes as chronometers for ESS events and to further understand stars and their lifecycles, there was interest in measuring the half-life of ^{60}Fe as early as the 1950's as it was suspected to have a long half-life. Details of the exact decay scheme were not known then, but were only speculations in [39] and are shown in Figure 1.13. Those speculations were mostly correct and the full decay scheme as it is known today is shown in Figure 1.14. Details of the experimental methods for each of the past measurements can be found in their references, [39], [28], [40], and [47]. Similar techniques were used for this work and details can be found in Chapters 4 and 5.

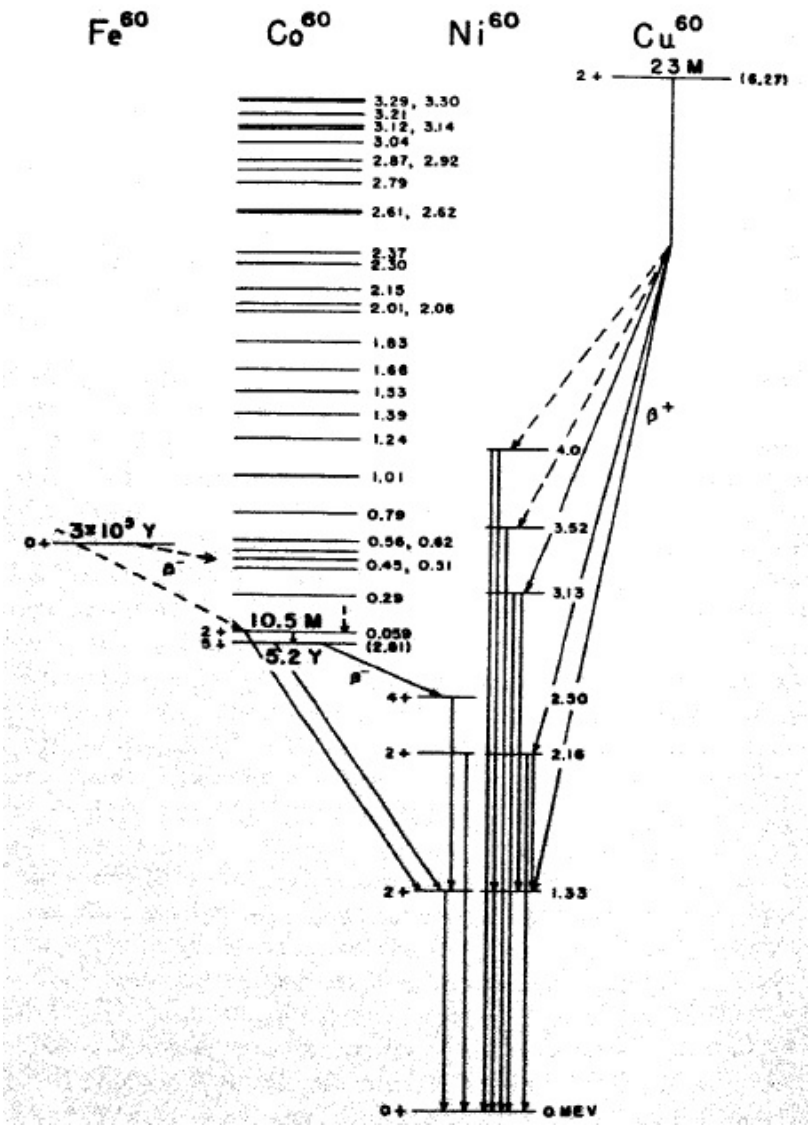

Figure 1.13. Mass relationships and energy levels of isobars at mass number 60 as suggested by [39] in 1957.

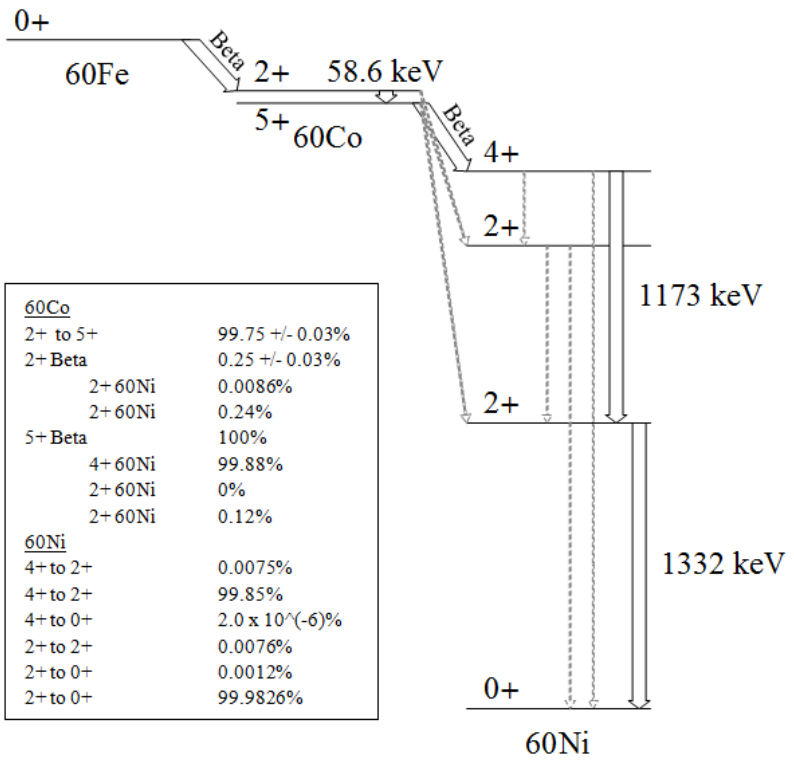

Figure 1.14. Currently accepted, full decay scheme for ^{60}Fe. Thick white arrows indicate decays that happen more prevalently (100% or almost 100% for each) and grey dashed arrows indicate other possible decays that occur. The decay of the 2+ state in ^{60}Co was used for the first experiment [39]. The two γ ray lines in the excited states of ^{60}Ni were used for all other past measurements [28] [40] [47].

The sample used for the very first experiment [39] was a copper target from the Carnegie synchrocyclotron. The copper was bombarded for 6 months with ~400 MeV protons. It was predicted that the yield of ^{60}Fe would be 0.3 times that of the yield of ^{59}Fe. Therefore, after the iron was chemically removed from the target, the activities of both ^{59}Fe and ^{60}Fe were measured. Specifically for the ^{60}Fe activity, the

gamma ray from the isomeric state in ^{60}Co was measured, as it is well known [34]. Relative to the well known half-life of ^{59}Fe, the half-life of ^{60}Fe was estimated to be 3×10^5 years, with an uncertainty of a factor of 3.

However, as pointed out by Kutschera, et al. [28], the questionable assumption of the production of ^{60}Fe relative to the production of ^{59}Fe from the first experiment could not rule out the possibility of a longer half-life [25]. Therefore, in 1984 a second experiment was done [28]. The activity and the ^{60}Fe concentration, relative to stable iron, were measured. The sample used was a copper disk that had been irradiated with 191 MeV protons at the Brookhaven Linac Isotope Producer for 28 days. The technique of accelerator mass spectrometry was used to measure the concentration of ^{60}Fe, and was performed at Argonne National Laboratory. The activity was determined through the decays of the excited states of ^{60}Ni. Kutschera, et al. [28] reported a half-life of $(1.49 \pm 0.27) \times 10^6$ years.

In an effort to make this half-life more accurate, the authors of [40] sought to remeasure it in 2009. A similar method was used: the activity was measured with the decay of the excited states of ^{60}Ni as in [28], and the number of ^{60}Fe atoms was measured using multicollector inductively coupled plasma mass spectrometry (MC-ICPMS). This also relied on a full removal of all mass 60 isobars as MC-ICPMS would not be able to discriminate between ^{60}Fe and its isobars. For this specific measurement, a new sample was available with an expected order of magnitude more ^{60}Fe than the sample used by [28]. The sample was again made out of a copper target, this time from a copper beam stop from the Paul Scherrer Institute. The copper material, used to stop beam particles, was bombarded with 590 MeV protons during a period of 12 years. Besides making the half-life more accurate and precise, Rugel, et al. [40] in fact measured a half-life of almost two times longer ($(2.62 \pm 0.04) \times 10^6$ years) than Kutschera, et al. [28]. This wide discrepancy inspired several new measurements to determine which half-life was correct and to minimize the error.

One such measurement was recently published in 2015 by Wallner, et al. [47]. This experiment used material from the same copper beam stop as the previous measurement by Rugel, et al. The activity was measured from the ^{60}Ni excited states and the number of ^{60}Fe atoms was measured with AMS at the Australian National University. For this, the concentration of ^{60}Fe was measured relative to a known amount of ^{55}Fe that was added to the sample, removing any dependence on an ^{60}Fe standard sample. Typically for AMS measurements, a standard reference material of the isotope of interest is also measured, along with the unknown material. Measuring a known sample back to back with an unknown sample removes any unquantifiable losses in the experiment. The results from Wallner, et al. [47] confirms the new, longer half-life, reporting a half-life of $(2.50 \pm 0.12) \times 10^6$ years, and suggests a weighted value of $(2.60 \pm 0.05) \times 10^6$ years.

The past three measurements relied on the decay of the ground state of ^{60}Co. This presents the problem of removing all ^{60}Co contamination in the sample at the start. Any ^{60}Co ground state decays that are not from the decay of ^{60}Fe would inflate the results and give a shorter half-life for ^{60}Fe. ^{60}Co can be removed from a sample using chemical treatment as done in the past measurements. However, in an attempt to completely bypass any chemical procedures and to reduce the error on the [28] value of $(1.49 \pm 0.27) \times 10^6$ years, Sam Austin from Michigan State University proposed a different method for producing an ^{60}Fe sample in collaboration with the AMS group at the University of Notre Dame (UND). The proposal, submitted in 2006, was for sample production at Michigan State University (more details are found in Chapter 2). Then in 2009, with the $(2.62 \pm 0.02) \times 10^6$ year half-life found by [40], the UND measurement found a second purpose of confirming or denying this longer half-life. Details of the experiment can be found in Chapters 4 (AMS measurement) and 5 (activity measurement).

1.5 Measuring Half-Lives on the Order of Millions of Years

Typically with shorter half-lives, it is experimentally easy to measure the activity as a function of time. Doing this and fitting the resulting exponentially decreasing curve, one can deduce the half-life with the following equation.

$$\mathrm{A(t)} = \mathrm{A_o} \cdot e^{-\lambda \mathrm{t}} \tag{1.1}$$

where $\mathrm{A_o}$ is the initial value of the activity of the sample, λ is referred to as the decay constant (the probability that a radioactive atom will decay), and t is time since the initial activity was measured.

However, with longer half-lives, as in the case of ^{60}Fe, it becomes virtually impossible to measure a change in activity. The half-life is so long that the activity of the sample effectively remains constant over the course of any measurement. For example, for a half-life of 2 million years, it would take 150,000 years to measure a change in the activity of 5%. The experimental method must find a way around this issue.

Expressing the decay constant, λ, instead with the equation

$$\mathrm{dN/dt} = -\lambda \mathrm{N} \tag{1.2}$$

where N is the number of radioactive atoms of interest, dN is the number of decayed radioactive atoms, and dt is the time period in which the atoms decayed, the expression can be then made more general. Furthermore, (-dN/dt) can be written as the the activity, A, of a radioactive sample, or the rate of decay and λ can also be written

as ln $2/t_{1/2}$. Plugging these into Equation 1.2 and rearranging for $t_{1/2}$ gives:

$$t_{1/2} = \frac{\ln 2}{A} N. \tag{1.3}$$

Therefore, the half-life can be calculated by knowing the number of radioactive atoms in, and the activity of, a sample. As mentioned earlier, experimental details for both the Accelerator Mass Spectrometry measurements (to measure the number of atoms) and the activity measurement are reserved for Chapter 4 and Chapter 5, respectively. Details about the artificially produced samples used for this experiment are found in Chapters 2 and 3. Two separate sample sets were produced and tested for this thesis work, and the direction of the project has changed multiple times since its conception. The following is a brief overview of the time line and overarching experiment thought process.

In 2006, a proposal was accepted at the National Superconducting Cyclotron Laboratory on the Michigan State University (MSU) campus to produce a new ^{60}Fe sample. This sample would be different from previously used samples because ^{60}Fe would be implanted into a foil instead of harvested from irradiated copper. The benefit of producing a sample this way is that no contaminant ^{60}Co would be implanted in the sample. As ^{60}Fe decays through ^{60}Co and measuring the direct decay of ^{60}Fe is difficult, previous measurements have measured the decay of the ground state of ^{60}Co as a proxy. Therefore if the sample contains any ^{60}Co not from the decay of ^{60}Fe, this would artificially inflate the activity of ^{60}Fe, giving an incorrect, lower half-life. As described in Chapter 2, ^{60}Co was not implanted but it was produced by reactions between the high energy ^{60}Fe and the aluminum catcher foil. During the chemistry steps to remove the produced ^{60}Co from the MSU sample, the new half-life value from Rugel, et al. [40] was published. With the half-life of ^{60}Fe in question, the method to measure the number of ^{60}Fe atoms in a sample (which relies on standard material,

which in turn relies on the half-life) needed to be revised. This is discussed in more detail in Section 2.2 and involves measuring ^{60}Fe/^{56}Fe and ^{55}Fe/^{56}Fe in an unknown sample and an ^{55}Fe sample.

With the new method, the plan for the MSU sample evolved to measure ^{60}Fe and ^{55}Fe in the sample at the University of Notre Dame (UND). As discussed later in Section 2.2, the ^{55}Fe could not be measured at UND but was measured by our collaborators at the Vienna Environmental Research Accelerator (VERA) Laboratory who had measured the concentration of ^{55}Fe in other samples. Ultimately the ^{55}Fe and the ^{60}Fe experiments went well but the activity of the sample was too low and was overwhelmed by background, which is discussed in Section 2.3.

At the same time, our collaborators at VERA, including Anton Wallner received one of the irradiated copper samples from the Paul Scherrer Institute (PSI). Details of this sample production are in Chapter 3. Wallner's original plan was to measuring the sample at VERA but the ^{60}Fe measurement could not be done there as the ^{60}Fe signal was overwhelmed by the contaminant stable isobar ^{60}Ni. Our group was approached to measure the concentration of ^{60}Fe in the PSI sample and we received sample material from VERA. However, due to the limitations of the low-energy injection system and the lack of dedicated equipment at UND, our ^{60}Fe measurement would not have been precise enough to keep the errors under 10% at the time. Wallner eventually moved to the Australian National University (ANU) and, with the dedicated system there, was able to measure the PSI sample very precisely and published in 2015.

With Wallner's switch to ANU, our group received one of the remaining PSI samples in liquid and began working on measuring the activity of ^{60}Fe in a new way. This is discussed in more detail in Chapter 5. Our measurement of the number of ^{60}Fe atoms then follows from Wallner's work and is discussed in Chapter 4, including the beam development that was done over the course of several years.

The evolution of these experiments is shown in Figures 1.15 and 1.16 for the MSU

sample and PSI sample, respectively.

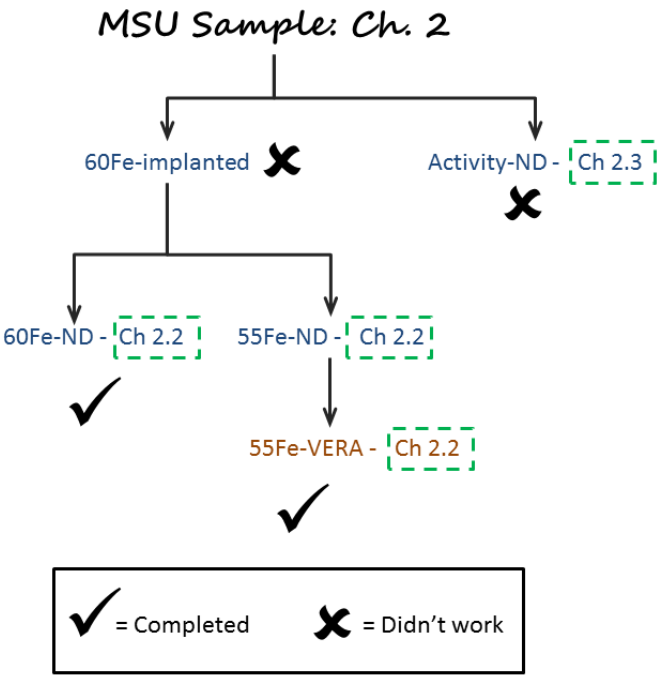

Figure 1.15. Flow chart of the plan for the sample produced at Michigan State University (MSU). In the end, the concentration of ^{60}Fe would be measured at the University of Notre Dame and the concentration of ^{55}Fe at the Vienna Environmental Research Accelerator Laboratory. This experiment ultimately failed due to the activity of the MSU sample.

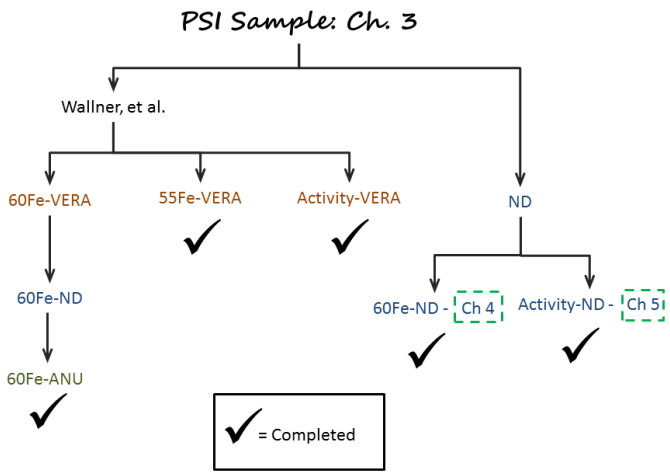

Figure 1.16. Flow chart of the plan for the sample produced at the Paul Scherrer Institute (PSI). This sample has been measured both by our group and the group from the Australian National University (ANU) lead by Anton Wallner who published in 2015 [47].

CHAPTER 2

FIRST ATTEMPT WITH MSU-PRODUCED ^{60}Fe SAMPLE

In 2006, even before the Rugel, et al. paper [40], a second measurement of the half-life of ^{60}Fe was planned. The Kutschera, et al. experiment [28] involved chemical procedures to remove any ^{60}Co in the sample originally. To avoid the need for chemical separation, an experiment was proposed at Michigan State University (MSU). This production method would implant ^{60}Fe into an aluminum foil, as opposed to harvesting ^{60}Fe from an irradiated target wich would include a host of other isotopes including the contaminant ^{60}Co. With implanting ^{60}Fe specifically, the only possible contamination from ^{60}Co would come from reactions between the high energy ^{60}Fe and the aluminum. Assuming that this rate was low, then no chemical separation would be needed. Therefore, by bypassing the complex chemistry and accurately knowing the amount of implanted ^{60}Fe, this method of production would be able to give an accuracy in the half-life of $\pm$ 5%.

The production of the ^{60}Fe at MSU is discussed in Section 2.1. The AMS measurement for both ^{60}Fe and ^{55}Fe is described briefly in Section 2.2. Detailed information about the facilities and the experiment at the University of Notre Dame (UND) is found later in Chapter 4. Section 2.3 is about the activity measurement where this first attempt ultimately failed.

2.1 ^{60}Fe Sample Production

The production took place at the National Superconducting Cyclotron Laboratory (NSCL) on the campus of MSU. A 140 MeV/A ^{64}Ni beam was impinged on a

700 mg/cm^2 thick beryllium target, "TA", shown in Figure 2.1. In theory, nuclear spallation reactions with high energy particles, such as ^{64}Ni on beryllium, produce masses up to and including the combined mass of the projectile (in this case, ^{64}Ni), and the target (beryllium). One of the products, among the many that can be produced by this reaction, is ^{60}Fe. Figure 2.2 illustrates the number of possible products of the reaction, as plotted as energy deposited versus time of flight at the focal plane of the A1900 mass fragment separator [19], when no filtering occurs.

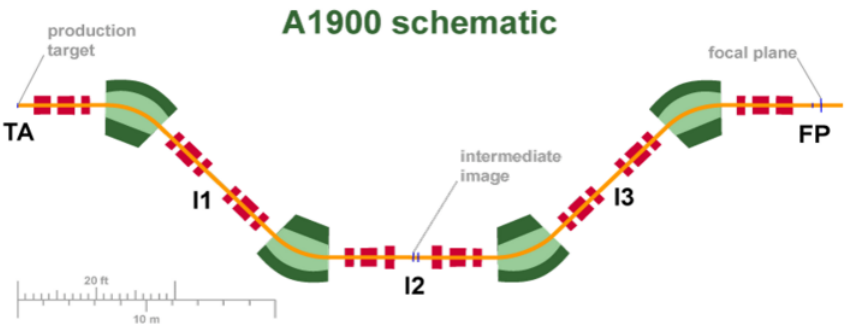

Figure 2.1. The A1900 mass fragment separator at the National Superconducting Cyclotron Laboratory at Michigan State University for magnetically filtering unwanted particles out of the beam. The elements in red are 40 different multipole magnets and the elements in green are four dipole magnets. The production target is located at "TA." Images 1, 2, and 3 are denoted with "I1", "I2", and "I3" respectively. The focal plane is located at "FP." [19].

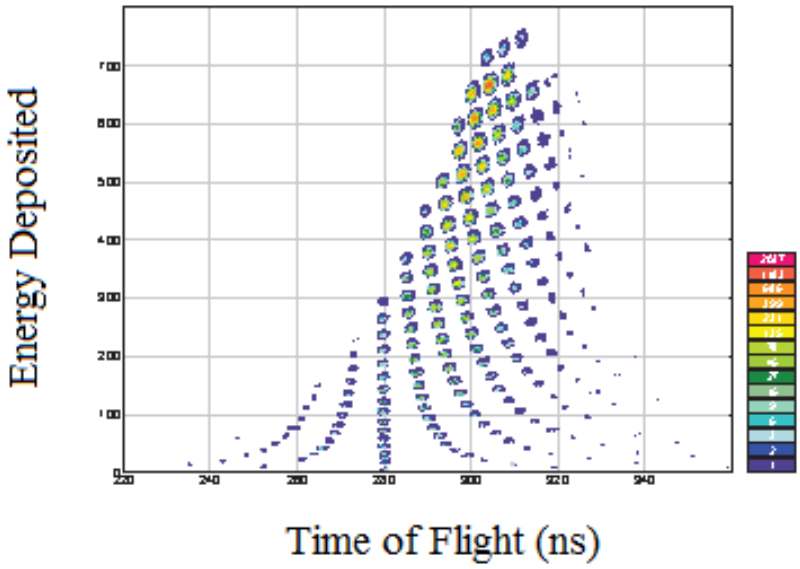

Figure 2.2. Energy loss as a function of time of flight as measured at the focal place of the A1900 mass fragment separator using LISE++ simulations. Each peak represents a different isotope that is produced by the reaction of a high energy ^{64}Ni beam on a beryllium target. By setting the beam elements of the A1900 mass fragment separator, one isotope can be selected and all others filtered out of the beam.

After the ^{64}Ni beam hits the beryllium target at position TA, the unreacted beam particles and the resulting products pass through the A1900 mass fragment separator which can magnetically filter out unwanted isotopes. The A1900, shown in Figure 2.1, consists of 40 large-diameter superconducting multipole magnets (red) and four 45° dipole magnets (green). Achromatic foil degraders were placed at Image 1 (150 mg/cm^2 thick aluminum degrader) and at Image 2 (200 mg/cm^2 thick aluminum degrader). These degraders, in the shape of wedges, were added to help with the energy loss. Particles that pass through thinner or thicker parts of the wedge will experience different amounts of energy loss. Therefore as the particles pass through

the four dipole magnets, they are bent differently in the magnetic field, helping to reject background contaminants. A more pronounced effect on the particles in the dipole magnets allows for greater amount of filtering. A stack of three silicon PIN photodiode detectors were put at the focal plane to identify the beam particles by measuring time of flight, energy loss, and total energy, see Figure 2.3.

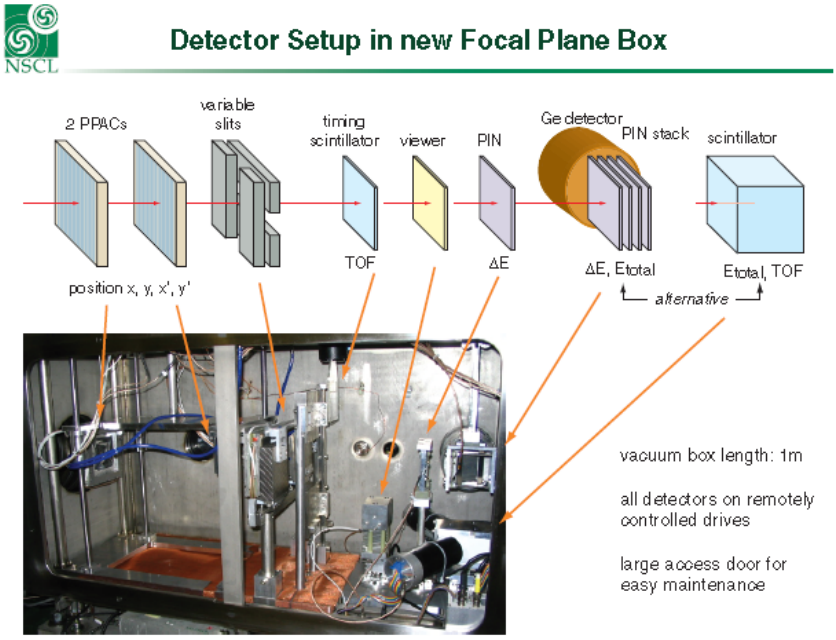

Figure 2.3. Detector Set-up at the Focal Plane of the A1900 mass fragment separator. This includes position (with the parallel plate avalanche counters, PPACs), time of flight (timing scintillator), energy loss (PIN detector), and total energy (scintillator). Each component from the schematic is also pointed out in a picture on the bottom left.

Based on LISE++ Monte Carlo simulations for the A1900, approximately 1×10^6 ^{60}Fe particles per second per particle nanoampere of the incoming ^{64}Ni beam

(pps/pnA) would make it to the focal plane.

The resulting filtered beam was implanted into a stack of four ultra pure aluminum foils (thicknesses of 0.5 mm, 0.5 mm, 2.0 mm, and 0.5 mm in that order). The thicknesses of the foils were chosen so that nearly all ^{60}Fe was stopped in the third foil. Several detectors were used to monitor the beam production and to get an accurate reading of the amount of ^{60}Fe implanted. A scintillator detector telescope was used to monitor light particles emitted from the beryllium production target. At the aluminum foil stack, a silicon detector was used to monitor scattered light particles at backwards angles as shown in Figure 2.4. Both of these were calibrated with lower intensity beams throughout the experiment. With the calibration done at several difference intensities of the incoming ^{64}Ni beam, it is possible to determine the amount of implanted ^{60}Fe as a function of the original ^{64}Ni beam.

Three samples in total were produced. Table 2.1 describes the characteristics of each sample including implantation time and intended purpose for each sample.

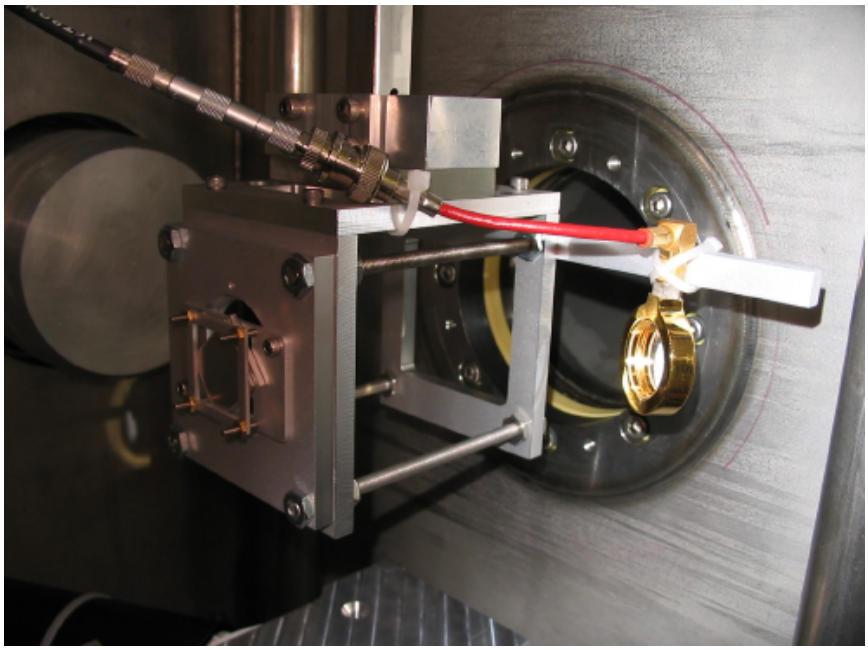

Figure 2.4. The silicon detector, located on the right side of this picture, used to monitor scattered light particles from the stopper. The beam comes from the right side of the picture and the silicon detector is at backwards angles.

TABLE 2.1

SAMPLES PRODUCED AT THE MSU NSCL IN JANUARY 2009

Sample #/Name	Time Implanted	Purpose
#1-^{60}Fe Sample	∼2 days	Split into 2, one for AMS and one for γ spec.
#2-AMS Sample	∼1 hour	A test of the experimental setup.
#3-^{60}Co Sample	∼ 2 hours	To track ^{60}Co reduction, if chemistry was needed.

Despite the fact that ^{60}Co was separated by the mass fragment separator and not implanted, some ^{60}Co was produced within the stopper from nuclear reactions between the high energy ^{60}Fe particles and the stopper itself. The presence of ^{60}Co in the samples was confirmed through γ ray spectroscopy done after the sample production. It was determined that the sample contained too much ^{60}Co and therefore ^{60}Co reduction chemistry was performed at Argonne National Laboratory to remove the contaminant. The chemistry involved dissolving the aluminum foils in ferric chloride hexahydrate with a natural iron spike aliquot which also set the concentration of the sample. The iron was separated from aluminum and cobalt by anion exchange chromatography. Then the iron was precipitated with ammonia and collected on a filter. In a fused silica beaker, it was combusted to produced Fe_2O_3. The iron oxide was then transferred to glass vials.

By comparing the ^{60}Co activity of the samples before and after the chemical steps, ^{60}Co was reduced by only a factor of 30 when a factor of 10^4 was needed. Therefore the samples went through a second set of chemistry. During this step, the sample was also spiked with ^{55}Fe so that measurements could be made of the concentrations of ^{60}Fe and ^{55}Fe relative to ^{56}Fe. The reason for this is found in the next section, 2.2.

Full details of the chemistry done on the MSU samples and the timeline of events are found in Appendix B. As a final step in the chemical procedures, the MSU sample was split into two. The larger portion (90% of the original) was used for an activity measurement, discussed in Section 2.3. The smaller portion (10% of the original) was used for an AMS experiment, discussed in the following section.

2.2 Determining Isotopic Concentrations of the MSU Sample

Measuring the isotopic concentration of a sample using AMS is a complicated process. To measure a sample absolutely, one must account for all losses through the system, calibrate all Faraday cup readings, and know the detector efficiency. This is difficult to do and requires a high level of precision - specifically that the equipment must remain constant over a long period of time and all parameters must be monitored in case of any changes. To alleviate this, AMS concentration measurements are done relative to standard material when possible. By measuring a standard and an unknown sample back to back, systematic errors and losses are accounted for.

For ^{60}Fe, however, standard material concentrations of ^{60}Fe relative to ^{56}Fe had been based on the previous, shorter half-life. Therefore, the standards were unreliable (with the half-life of ^{60}Fe in question). A new method was proposed to measure relative to a different standard, ^{55}Fe. In this method, a similar amount of ^{55}Fe was added to each sample as compared to the expected amount of ^{60}Fe. ^{55}Fe has a well known half-life and standard material is readily available, making it a good candidate. Then, the concentration of ^{60}Fe/^{56}Fe and ^{55}Fe/^{56}Fe would be measured in the unknown sample and the ^{55}Fe/^{56}Fe would be measured in a known standard in the same conditions. This would allow a correction factor between the measured and true values of ^{55}Fe/^{56}Fe from the standard to be found and then applied to the measured ^{60}Fe/^{56}Fe. The true ratio of ^{60}Fe to ^{56}Fe can be found using the following equation, where the raw values refer to the experimental measured values and sample

refers to the unknown and the standard refers to the known sample.

$$(60/56)_{\text{sample, true}} = \underbrace{\frac{(60/56)_{\text{sample, raw}}}{(55/56)_{\text{sample, raw}}}}_{\text{a}} \times \underbrace{\frac{(55/56)_{\text{sample, raw}}}{(55/56)_{\text{standard, raw}}}}_{\text{b}} \times \underbrace{(55/56)_{\text{standard, true}}}_{\text{c}} \tag{2.1}$$

$$\text{a} = \text{Relative amounts of } {}^{60}\text{Fe}/{}^{56}\text{Fe and } {}^{55}\text{Fe}/{}^{56}\text{Fe in sample}$$

$$\text{b} = \text{Relative amounts of } {}^{55}\text{Fe}/{}^{56}\text{Fe in sample and standard}$$

$$\text{c} = \text{True amount of } {}^{55}\text{Fe}/{}^{56}\text{Fe in standard.}$$

The main hurdle to jump over with an ^{60}Fe AMS measurement is to separate ^{60}Fe from its stable isobar, ^{60}Ni, which passes through the accelerator system with the same behavior. Without separating the two isobars, we would see an inflated (and false) amount of ^{60}Fe at our particle identification detectors. Work started in 2010 on a method to measure the ^{60}Fe/^{56}Fe concentration at the University of Notre Dame's Nuclear Science Laboratory (NSL). Good separation had been observed between ^{58}Fe and ^{58}Ni (see Chapter 4 for more information). These two isobars show very similar properties as ^{60}Fe and ^{60}Ni and are used as good proxies for the mass 60 isobar pair. Background concentrations of ^{60}Fe/^{56}Fe were on the order of 10^{-12}, below the expected ^{60}Fe/^{56}Fe concentration of the MSU sample. However, determining the ^{55}Fe/^{56}Fe concentration at the NSL proved impossible. Contamination from ^{55}MnH was prevalent enough to overwhelm the expected ^{55}Fe signal. ^{55}Fe decays to ^{55}Mn, which is stable, and ^{55}MnH is easily produced in the ion source. Despite the small mass difference and the molecular dissociation in the carbon stripper foil in the tandem accelerator, the isotopic selectivity is not good enough and allows ^{55}Mn to make it through the beam line elements to the detectors. This overwhelms the true signal from ^{55}Fe.

The solution was to measure the $^{60}Fe/^{56}Fe$ concentration at the NSL and the $^{55}Fe/^{56}Fe$ concentration at the Vienna Environmental Research Accelerator (VERA) Laboratory in Austria. Figure 2.5 is a schematic of the laboratory setup at VERA. MSU sample material was packed into aluminum cathodes for use in Source 2, a Multi-Cathode Source of Negative Ions via Cesium Sputtering (MC-SNICS) ion source. With the use of an electrostatic analyzer and a 90° bending magnet after the ion source, all of the contaminants are filtered out before the beam reaches the accelerator (3 MV tandem accelerator). The 3+ charge state of the beam and a terminal voltage of 2.75 MV were used. A small ionization chamber was placed at the end of the "PIXE-ART" beam line after the switching magnet for particle identification. The MSU samples from the Table 2.1, #1 (^{60}Fe Sample) and #2 (AMS Sample), were measured along with a ^{55}Fe standard "A0." The scaling factor from the A0 standard was 1.13 ± 0.10. The expected and final scaled concentrations for the samples and the standard can be found in Table 2.2. The final scaled values for the ^{55}Fe concentration were close to the expected values.

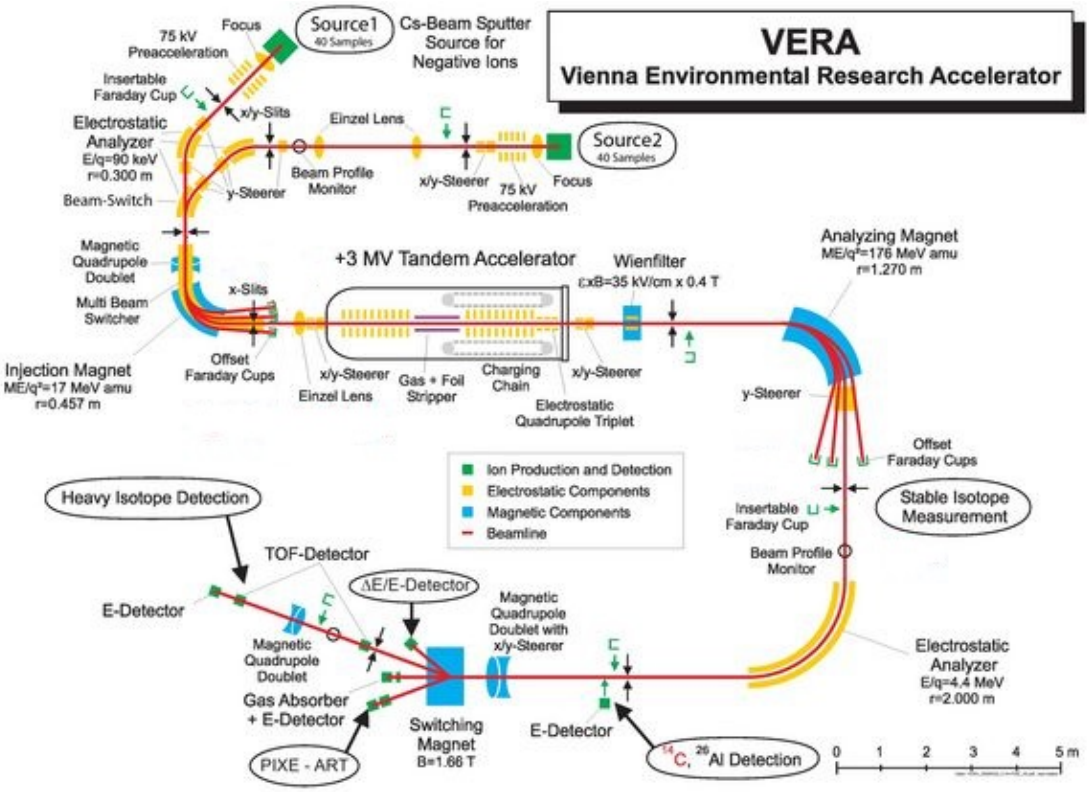

Figure 2.5. Schematic of the facilities at the Vienna Environmental Research Accelerator Laboratory. Source 2 was used for the ^{55}Fe measurement and a small ionization chamber was placed on the PIXE-ART beam line for particle identification.

TABLE 2.2

EXPECTED AND MEASURED ^{55}FE/^{56}FE CONCENTRATIONS FOR THE STANDARD, A0, AND TWO UNKNOWN SAMPLES

Material	Expected ^{55}Fe/^{56}Fe	Measured ^{55}Fe/^{56}Fe [a]
A0	3.26×10^{-10}	x
#1-^{60}Fe Sample	7.69×10^{-12}	$(6.57 \pm 0.04) \times 10^{-12}$
#2-AMS Sample	3.85×10^{-12}	$(3.11 \pm 0.03) \times 10^{-12}$

[a]The measured values of the ^{60}Fe sample and the AMS sample have been corrected with the scale factor found from the A0 standard.

2.3 Activity Measurement

Despite the success of the ^{55}Fe/^{56}Fe experiment at VERA and the expected success of the ^{60}Fe/^{56}Fe measurement at the NSL, the activity measurement proved more difficult than anticipated. The measurement was done with a coaxial High Purity germanium (HPGe) detector that has a maximum efficiency in the range needed for the decays of the excited states of ^{60}Ni (1173 and 1332 keV, see Chapter 5, Figure 5.1 for the full decay information). The detector was surrounded by two layers of lead bricks to eliminate as much of the room background as possible without adding unnecessary background from the bricks themselves, either through contaminants or interactions with other γ rays. The inner cavity was lined with copper sheets to decrease the energy of any γ ray that was able to pass through the lead. This, however, was not enough.

Two separate HPGe coaxial detectors were tested, a 50% relative efficiency and

a 130% relative efficiency. Relative efficiency refers to a quoted level of efficiency relative to a standard 3 inch by 3 inch NaI(Tl) scintillation crystal. Hence it is possible to have a germanium detector with a quoted relative efficiency of more than 100%. This quoted efficiency is not used when calculating the true number of photons emitted from the source but is only an industry convention.

Background measurements were taken with both detectors. Looking at a region around the excited states in ^{60}Ni, the 50% detector had a background of 80 counts per day (1173 keV) and 52 counts per day (1332 keV). Similarly with the 130% detector, the background rates were 116 counts per day (1173 keV) and 97 counts per day (1332 keV). The ^{60}Fe activity of the sample on the date of January 17, 2012 (when the background measurements were being considered) should have been approximately 525 decays per day from the ^{60}Co γ ray lines. Considering the detector efficiencies, found to be approximately 1% for the 50% HPGe and 3% for the 130% HPGe, only 5 counts per day and 15 counts per day, respectively, would be recorded with each detector. For both of the detectors, the background rates are far too high to distinguish the sample's decay from the room background. Similar tests were done with NaI detectors, in hopes that increased detector efficiency would solve the issues (see Table 2.3). However, the background rate still overpowered the sample's activity. An example using the 50% relative efficiency HPGe detector is shown in the following figures, 2.6 and 2.7.

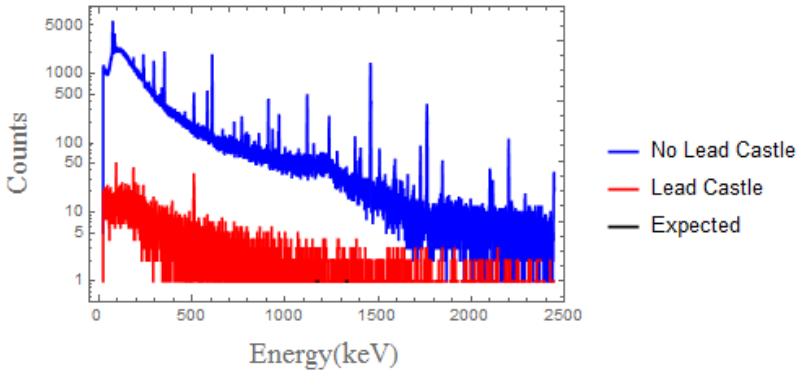

Figure 2.6. Four hour backgrounds with the 50% HPGe detector with (red) and without (blue) two layers of lead bricks to reduce the room background radiation. The expected count rate for the MSU sample is shown in black at energies of 1173 keV and 1332 keV. This count rate from the MSU sample, assuming a detection efficiency of 1%, would be less than one count per four hours.

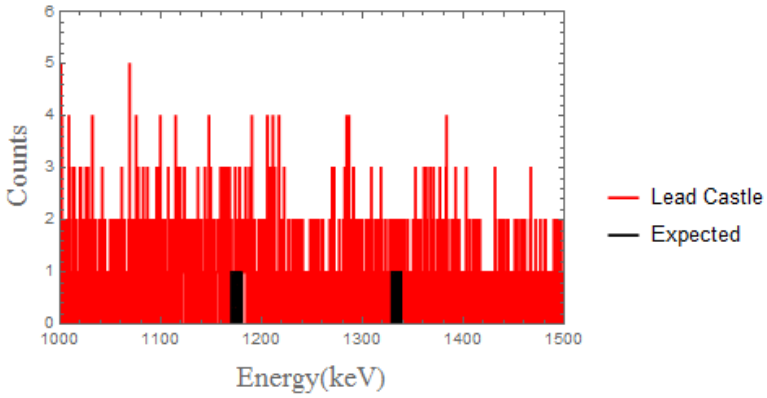

Figure 2.7. Zoomed in version of the Figure 2.6 on the region of interest. The background over a four hour time period is shown in red and the expected counts from the sample are in black. The expected count rate from the MSU sample is below the background rate for this detector and lead castle setup.

Efforts to either move the equipment to another laboratory, or find a laboratory capable of performing the measurement entirely were unsuccessful. In recent years, the NSL has become involved in supporting a new accelerator laboratory in the Homestake mine in South Dakota, which is 2400 meters underground. This may be a location, or something similar, where the activity measurement could be continued.

Work then began using a different sample, one from the Paul Scherrer Institute, that is expected to contain approximately two orders of magnitude more ^{60}Fe atoms. The production of this sample is described in the following chapter.

TABLE 2.3

TEST OF THE BACKGROUND RADIATION WITH TWO NAI(TL) DETECTORS

Detector	Mode [a]	Shielding [b]	Peak Efficiency [c]	Background Counts/day in Region	Cts/day, Eff [d]
50% HPGe	Singles	Lead	1%	52 (1332 keV)	5
130% HPGe	Singles	Lead	3%	97 (1332 keV)	15
NaI(Tl)	Total Sum	None	25%	1194720	131
NaI(Tl)	Total Sum	Lead	16%	146736	84
NaI(Tl)	Coincidence	None	10%	8976	52
NaI(Tl)	Coincidence	Lead	7%	1104	36
NaI(Tl)	Singles	Concrete	–	12690	–
NaI(Tl)	Singles	Lead	–	2592	–

[a]Total Sum=total in sum peak (2507 keV), Coincidence=1332 and 1173 keV lines at the same time, Singles=single detector.

[b]Lead Castle shield, Concrete Castle shield, or no shielding at all.

[c]Ratio of counts in full energy peak divided by number of gamma rays emitted by source.

[d]Last column is the count rate we should see of our sample based on the detector efficiency (column 3).

CHAPTER 3

PRODUCTION OF THE PSI ^{60}Fe SAMPLE

In our second attempt, a sample produced at the Paul Scherrer Institute (PSI) was used. A research and development program was started at PSI called ERAWAST (Exotic Radionuclide from Accelerator Waste for Science and Technology). This initiative was started to produce rare, exotic, or otherwise difficult to produce isotopes by bombarding matter with high energy protons. For this sample, protons from the PSI cyclotron at energies of 590 MeV and beam currents up to 2.4 mA were bombarded into a beam stop for 12 years starting in 1980. The beam stop, made of copper, was used to safely absorb charged particles from the accelerator when the beam was not in use elsewhere. Because the beam had an energy high enough, reactions with the beam and the copper produced other radioactive isotopes. The inner 2 cm of the copper beam stop had the highest activity of isotopes such as ^{26}Al, ^{44}Ti, ^{53}Mn, ^{59}Ni, and ^{60}Fe. Several grams of the copper beam stop were dissolved in nitric acid and then underwent several chemistry steps to remove contaminants, especially ^{60}Co. Two samples were produced, each containing $\sim 10^{16}$ atoms of ^{60}Fe and $<$0.25 Bq of ^{60}Co.

One of the samples was used in a $^{60}\mathrm{Fe}(\mathrm{n},\gamma)^{61}\mathrm{Fe}$ reaction experiment [45]. Approximately one third of this sample was then recovered and purified from the grown-in ^{60}Co. The sample at this point contained $\sim 3.5\times10^{15}$ ^{60}Fe atoms in 1.00027 grams of Fe_2O_3. The sample was split into two. The larger amount (0.65005 grams) was used for a grow-in ^{60}Co decay measurement for Wallner, et al. [47]. The smaller amount (0.30120 grams) was made into a dilution series for Accelerator Mass Spectrometry

measurements. Expected concentrations and relative amounts of the dilution series samples are shown in Table 3.1 that is reproduced from [47]. This sample, as briefly described at the end of Chapter 1, was originally going to be measured by our collaborators at the Vienna Environmental Research Accelerator (VERA) laboratory. However, due to the stable isobar contaminant ^{60}Ni, the concentration of ^{60}Fe/^{56}Fe could not be measured at VERA. Our group was then approached to measure the ^{60}Fe concentration and we received a small amount of the dilution series samples in the form of powder.

The scope of our involvement changed again, as mentioned previously, when Wallner moved to the Australian National University and it was deemed that the MSU sample activity could not be measured. Our plan then became to measure the ^{60}Fe concentration and the activity of one of the samples in the dilution series. Instead of measuring the same γ ray lines from the decay of the ^{60}Co ground states as our collaborators had, we planned to measure the decay of the isomeric state in ^{60}Co. For this final plan, we also received the remaining Fe-1 sample which was in liquid form (dissolved in hydrochloric acid, total mass of (13.0016 $\pm$ 0.0001) grams) which would serve as our activity sample. To remove any geometry effects for the activity measurement with the liquid Fe-1 source, it was evaporated into a point source under the direction of John Greene at Argonne National Laboratory. For the evaporation, the 13 mL Fe-1 sample was transferred to a 20 mL glass beaker and placed on a hot plate under a heat lamp, see Figure 3.1a. The acid was evaporated until the total volume was <1 mL. The 1 mL solution was then transferred to a 1 mL conical glass vial. This vial was placed in a hot water bath on the hot plate and under the heat lamp, see Figure 3.1b. The evaporation continued until <0.1 mL was left. From there, the solution was pipetted and deposited on a thin mylar plastic piece (0.002 inches thick, 1.25 inches by 1.25 inches square), see Figure 3.1c. The drop was allowed to completely dry and then a piece of tape was placed over the drop to prevent

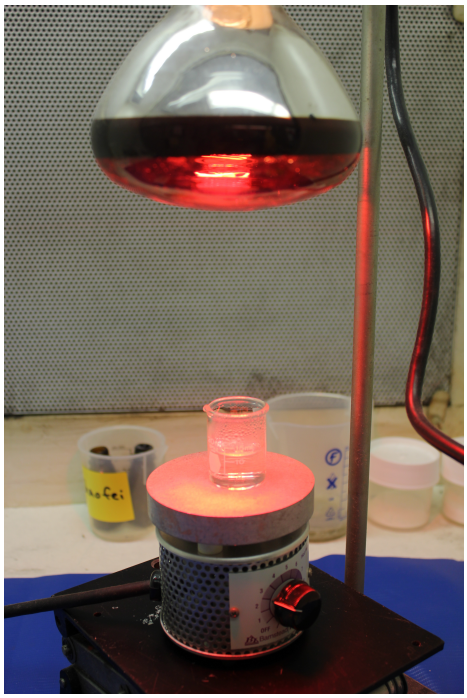

(a) Evaporating the HCl acid to make the remaining Fe-1 sample into a point source for an activity measurement. The sample was transferred to a glass beaker and placed on a hot plate and under a heat lamp.

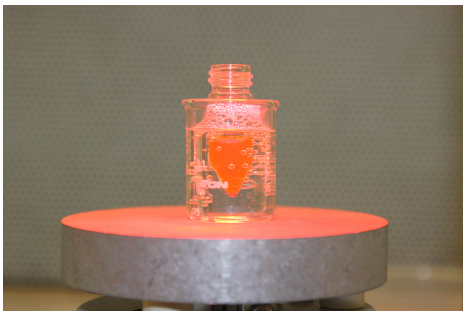

(b) At 1 mL left, the Fe-1 sample was transferred to a glass vial with a conical base and place in a hot water bath.

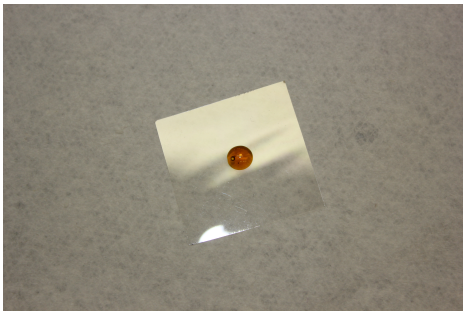

(c) The remaining Fe-1 was pipetted onto a 0.002 inch thick piece of mylar and allowed to dry.

Figure 3.1. Evaporation process for the liquid Fe-1 Sample to make it into a point source for the activity measurement.

losses. This tape is expected to not affect the count rate from the γ rays.

A similar point source was made using a calibrated ^{241}Am source mixed with Fe_2O_3. The original source, purchased from Eckert and Ziegler, was $AmCl_3$ in 1 M hydrochloric (HCl) acid for a total weight of 1.01422 g in a 1 mL vial. The activity on the reference data of March 1, 2014 was 3763 Bq with an uncertainty of 3%. Prior to evaporating the HCl acid, 6.5 mg of Fe_2O_3 was added to the Am source. This amount matches the amount of Fe that is present in the Fe-1 activity sample, that is 13% of the original Fe-1 sample which contained 50 mg. This ^{241}Am source, now in

the same geometry, thickness, and density as the Fe-1 activity sample, was used to determine the detector efficiency as ^{241}Am has a γ ray line at 59.54 keV (35.9 $\pm$ 0.4 % intensity, [5]). More discussion on this will be in Chapter 5

TABLE 3.1

DILUTION SERIES FOR ^{55}FE BETA ACTIVITY (LSC) AND THE ^{55}FE/^{56}FE ATOM-RATIO MEASUREMENTS (AMS)

Sample Name [a]	Fe carrier [b] (mg)	N_{56} (^{56}Fe at) ($\times 10^{20}$)	Dilution factor for ^{55,60}Fe	N_{60}/N_{56} relative to Fe-1	N_{55}/N_{56} relative to Fe-1	^{55}Fe/^{56}Fe (AMS measured; VERA [c])	^{55}Fe/^{56}Fe (AMS) relative to Fe-1	^{55}Fe activity [d] (Bq/g)
Fe-1	50.0	4.95	1	1	1	$(4.64 \pm 0.09) \times 10^{-7}$	1	22185 ± 755
Fe-2	55.0	5.44	10	0.091	0.091	$(4.37 \pm 0.06) \times 10^{-8}$	0.094 ± 0.002	2230 ± 79
Fe-3	55.5	5.49	100	0.0090	0.0090	$(4.30 \pm 0.14) \times 10^{-9}$	0.0093 ± 0.0004	217 ± 7
Fe-4	55.55	5.50	1000	0.00090	0.00090	$(4.35 \pm 0.18) \times 10^{-10}$	0.00094 ± 0.00004	22 ± 1

[a]Table reproduced from [47].

[b]Fe standard solution with 1 mgFe/mL.

[c]Not normalized to standard.

[d]LSC measurements from 100 μL aliquots of the 100-mL samples relative to a ^{55}Fe reference material valid for 01/01/2010 ([46]).

CHAPTER 4

ACCELERATOR MASS SPECTROMETRY FOR ^{60}Fe

In the following chapter, the technique of Accelerator Mass Spectrometry will be discussed in detail by highlighting the facilities and techniques used at the University of Notre Dame for this dissertation. Multiple experiments for beam development were performed and two sets of data are given in this chapter. Both sets of data were done under very similar conditions. Throughout the first part of this chapter, the settings and the reasons for choosing those settings are given for various pieces of equipment from the first of these data sets, completed in November 2015. The second of the final results was done in May 2016 and those settings are given in the last section of this chapter. The chapter concludes with the measurement method and results for the PSI samples that were measured from these two experiments.

4.1 Beginnings of Accelerator Mass Spectrometry

Accelerator Mass Spectrometry (AMS) is an ultra-sensitive technique, building on the principles of conventional mass spectrometry, to measure very low isotopic concentrations by mass separation. The differences in the two experimental techniques are illustrated in Figure 4.1. The first AMS experiment unwittingly occurred in 1939 and was not recognized as such. It accidentally discovered ^{3}He in nature by using a cyclotron as a mass spectrograph. At a cyclotron magnetic field between values corresponding to 8 MeV protons and 32 MeV alphas, a smaller beam was seen and given the equipment parameters could only have been ^{3}He, discovered for the first time. A description of the experiment is given in [4]. The experiment, however, was

not recognized as a new method until nearly 40 years later when the technique would be renewed to look for quarks with unit charge [33]. In the same year, that group of scientists also came up with the idea to use this technique for radiocarbon dating [32]. It didn't take long for the AMS technique to bleed into other areas of physics and science in general, becoming the workhorse of fields such as environmental studies. A nonexclusive list includes extraterrestrial applications, environmental sciences, geoscience, archeology, physics, materials, and life sciences. Many books, including [44], and many review articles, including [27], contain more in-depth discussions of these various applications.

AMS measures concentrations of isotopes by relying on the ability to filter out any unwanted particles or contaminants based on magnetic or electric rigidity. For example, with ^{60}Fe, unwanted contaminants from neighboring iron isotopes or the stable isobar, ^{60}Ni, must be filtered out. Without filtering, the AMS technique would measure both contaminants and ^{60}Fe as ^{60}Fe and this would inflate the true amount in the sample.

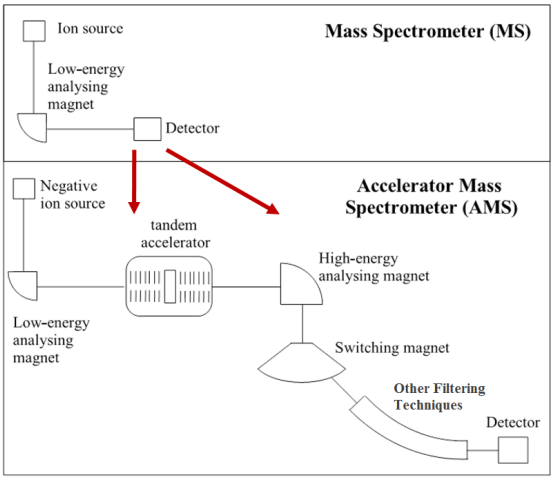

Figure 4.1. Differences in mass spectrometry and accelerator mass spectrometry. The major difference comes from the use of a particle accelerator which boosts the particles of interest to higher energies than attained in mass spectrometry. This allows experimenters to use other filtering and detection techniques not available at lower energies in order to make particle identification in terms of mass and proton number. Illustration edited from [1].

4.2 AMS at University of Notre Dame

The techniques and equipment used as filters within AMS are as numerous as the fields of research and the isotopes studied. Below, the facilities and the techniques used at the University of Notre Dame are illustrated as an example. A technical layout of the facilities is shown in Figure 4.2. The following sections will highlight the major components of the beamline necessary for the AMS technique.

4.2.1 Source of Negative Ions via Cesium Sputtering (SNICS) Ion Source

A Multi-Cathode Source of Negative Ions via Cesium Sputtering (MC-SNICS) ion source is used to produce beams for the FN Van de Graaff Accelerator at the

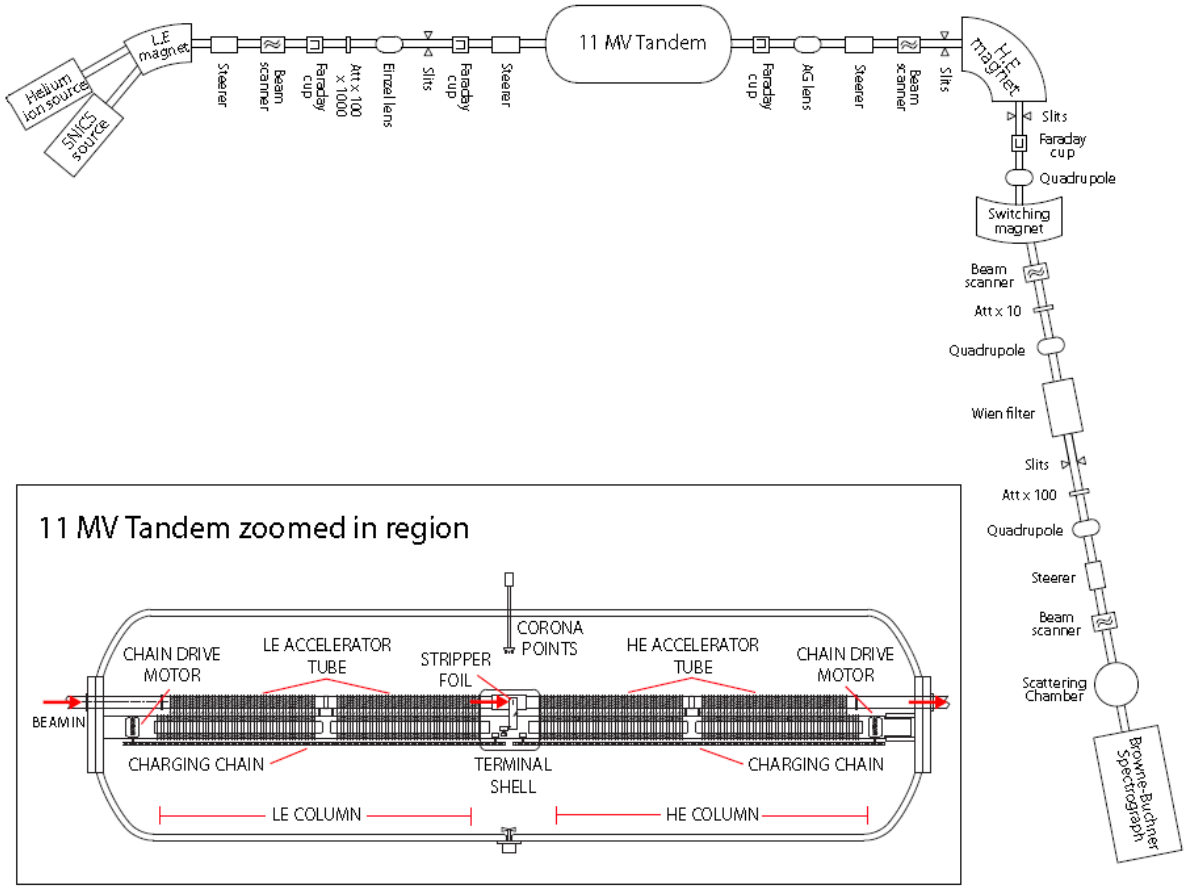

Figure 4.2: A schematic of the layout at the Nuclear Science Laboratory on the campus of the University of Notre Dame. Only components important to Accelerator Mass Spectrometry experiements are shown. Inset: A detailed internal view of the accelerator, courtesy Bradley Mulder.

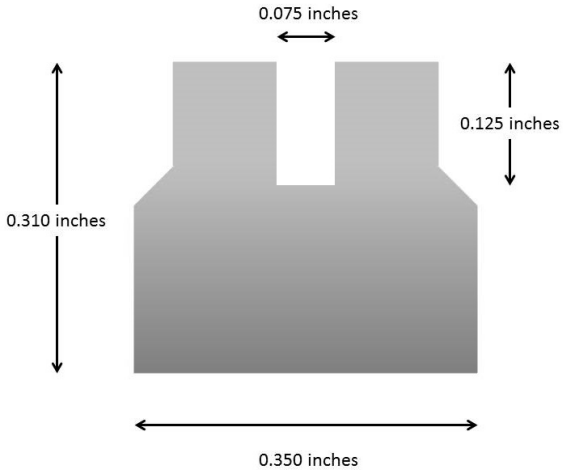

Figure 4.3. Drawing of an aluminum cathode used in the SNICS ion source. The desired material is pressed tightly into the cavity shown which has a depth of 0.125 inches and a diameter of 0.075 inches.

Nuclear Science Laboratory (NSL). Sample material, in the form of powder, is packed tightly into the cavity of small aluminum cathodes, or cylinders that fit specifically into the ion source. A drawing of a cathode, including dimensions, is shown in Figure 4.3. The cathodes have a small cavity where the material is pressed into place. 20 cathodes can be held in one wheel, which is mounted at the back of the ion source. Not needing to break vacuum at the ion source for each new sample provides a significant time advantage when doing multiple samples as is typically done in AMS experiments. This time advantage is also helpful when comparing multiple samples as it only takes minutes to change between samples as opposed to hours when needing to break vacuum for each sample change.

For this experiment, the cathode material, in the form of Fe_2O_3 powder, came from the dilution series made from PSI sample material, discussed in Chapter 3. There were four samples of various $^{60}Fe/^{56}Fe$ concentrations made as part of the dilution series.

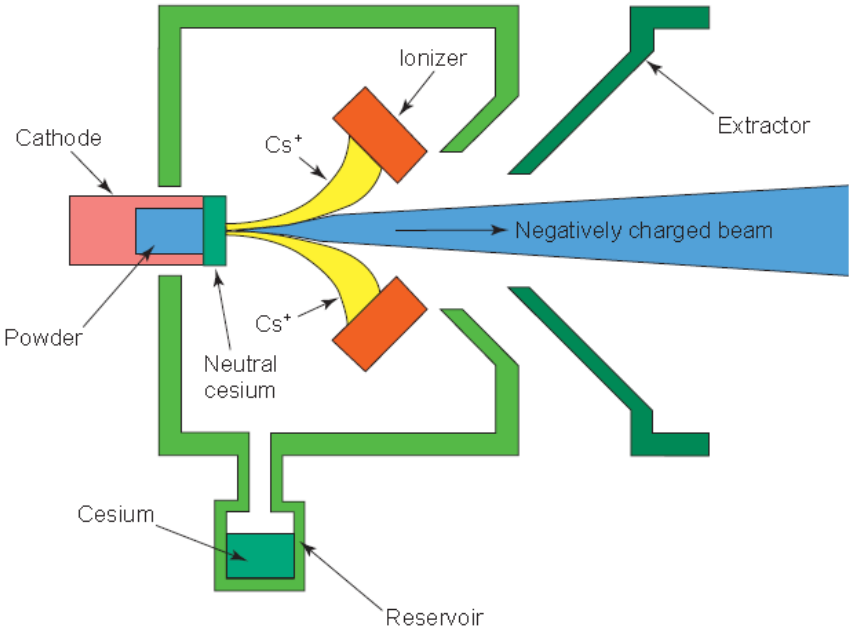

Figure 4.4. Schematic of the Source of Negative Ions via Cesium Sputtering (SNICS) ion source, courtesy of National Electrostatics Corporation.

Figure 4.4 is an illustration of the working principles behind the ion source. A reservoir of cesium metal is heated at the bottom of the ion source. Cesium vapor fills the area between the cathode and the ionizer. The cathode is held at negative potential and cooled while the ionizer is heated. A layer of cesium accumulates on the cathode and the ionizer. When fresh cesium hits the cesium-coated ionizer and boils off as positively charged ions, the cesium will accelerate toward the cathode. The cesium then hits the cathode material and causes it to be sputtered. The material gains an electron going out through the layer of cesium. The material is then accelerated away by the extractor and forms a beam. This initial acceleration is small, on the order of < 100 keV.

Typical settings for the MC-SNICS source at the NSL for ^{56}Fe, ^{58}Fe, and mass 60

(^{60}Fe, ^{60}Ni) are found in Table 4.1. These were the settings used during an experiment in November 2015, however the values for some settings may change slightly with each new tune of the accelerator system. Tuning the full system, ion source to final detector, is done with a "pilot" beam. In this case the pilot, or test, beam is ^{56}Fe, which is the most abundant iron isotope. The tune using the pilot beam will be the same tune used for the isotope of interest. The pilot beam is also used to measure the beam transmission, or the percentage of the beam put out by the ion source that is transported through the full system. The current of the pilot beam, ^{56}Fe, also factors into the sample's measured concentration, which is proportional to the ratio of the number of ^{60}Fe counts in the detector and the ^{56}Fe current from the ion source, correcting for beam transmission.

TABLE 4.1

SETTINGS FOR SNICS DURING THE NOVEMBER 2015 EXPERIMENT

	SNICS Component [a]	Digital Readout
Ion Source	Ionizer Current	26.10 A, 187 W
	Cathode Voltage	3.14 kV
	Extractor Voltage	14.99 kV
	Focus Voltage	2.44 kV
	^{56}Fe Bias Voltage	57.93 kV
	^{58}Fe Bias Voltage	55.16 kV
	mass 60 Bias Voltage	54.09 kV
	LE Magnet Current	54.11 A

[a]Ionizer current, Cathode voltage, Extractor voltage, Focus voltage, and the Magnet current will remain the same for each mass. By changing the Bias voltage, different masses will be bent through the SNICS Magnet. The Cathode voltage plus the Extractor voltage plus the Bias voltage is the energy of the beam as it exits the ion source. The Ionizer current relates to the amount of cesium that is sputtered and the focus voltage relates to the beam tune.

4.2.2 Low Energy (LE) Magnet

The magnet immediately following the SNICS ion source, referred to in Table 4.1, is used to select the beam injected into the accelerator. Particles with the correct ME/q^2 are bent so as to be transported to the accelerator. The mass of the particle or molecule is denoted by M, E represents the energy of the particle or molecule, and q is the charge state, which in this case is -1.

4.2.3 FN Van de Graaff Tandem Accelerator

The negatively charged particles that are selected by the low energy magnet are injected into the FN Tandem Accelerator, see the schematic in Figure 4.2. The accelerator is contained within a 40-foot-long, 12-foot-diameter tank. The tank is used to isolate the accelerator which only touches the tank at the ends. The tank contains 200 pounds per square inch of gas to act as a dielectric against discharges, or sparks, from the high voltage terminal to the inner tank walls. The gas is a mixture of dry N_2 and CO_2. Charge is brought up from the two ends of the tank via pelletron chains, which are alternating pieces of insulating plastic and charge-carrying metal cylinders. The charge is then picked off and placed on a metal shell, called the terminal shell, at the center of the tank. The beam particles move through an evacuated tube, called the column tube, that stretches from one end of the tank to the other. For the beam to experience a smooth gradient in the electric field between ground (the ends of the tank) and the terminal shell, nearly 800 resistors with 300 MΩ of resistance each connect the column from the end of the tank to the center. Compression from a very large spring holds all of the components together inside the tank.

With all of this, once the beam particles enter the tank, the negatively charged particles will be smoothly accelerated toward the terminal shell. At the center of the shell, the beam passes through a 3 $\mu g/cm^2$ carbon foil. By doing so, electrons are stripped off of the ions and molecules, and molecules will break up. Passing through the carbon foil will give a distribution of charge states, centered around the most probable state which is based on the particle's mass, energy, and proton number. The particle, now positively charged, will be accelerated away from the terminal shell and out through the high energy end of the accelerator. A second carbon foil stripper, with the same thickness as the first carbon foil, can be placed halfway between the terminal shell and the high energy end of the accelerator, shown in Figure

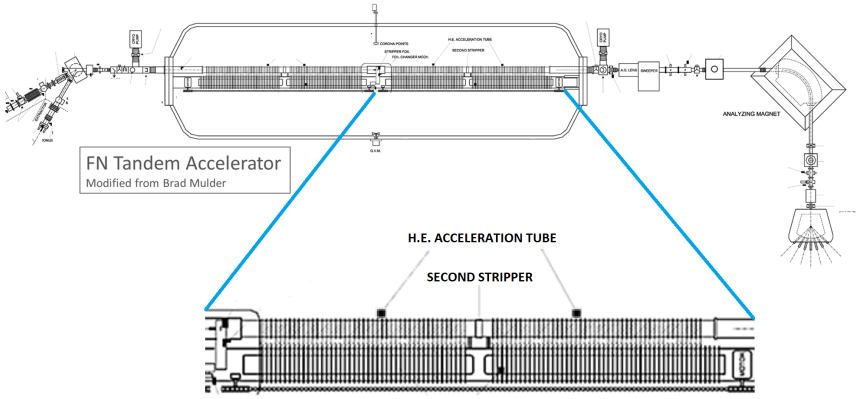

Figure 4.5. Technical schematic of the FN accelerator at the NSL. Inset is a zoomed in portion focused in on the midplane, halfway between the terminal and the high energy base where the second stripper compartment is located.

4.5. The energy of the beam with one carbon stripper is given by

$$E = TV \cdot (\frac{M}{M_{inj}} + q) + E_{pre} \cdot (\frac{M}{M_{inj}}), \tag{4.1}$$

where

$$\begin{aligned} TV &= \text{Terminal Voltage,} \\ M &= \text{Mass after dissociation of molecule, if any,} \\ M_{inj} &= \text{Mass injected to accelerator,} \\ E_{pre} &= \text{Energy given to the beam by the ion source,} \\ &= \text{Cathode Voltage + Extractor Voltage + Bias Voltage, and} \\ q &= \text{selected charge state after stripper.} \end{aligned}$$

Similarly, with two carbon strippers, the energy of the beam is

$$E = TV \cdot (\frac{M}{M_{inj}} + \frac{q_1}{2} + \frac{q_2}{2}) + E_{pre} \cdot (\frac{M}{M_{inj}}), \tag{4.2}$$

where q_1 is the charge state of the beam after the first stripper in the terminal shell and q_2 is the charge state of the beam after the second stripper. Based on this equation, to increase the beam energy, one needs to either increase the terminal voltage for the accelerator or chose a higher charge state. Both of these have their limits with either not being able to increase the terminal voltage further or sacrificing the amount of beam current. This is illustrated in Figure 4.6. As the terminal voltage is increased, the peak in the charge state distribution also increases slightly. By using the second carbon foil and stripping the beam particles twice, the charge state distribution can be shifted to higher charge states, but for the cost of less beam current, as reflected in the probability for the 2nd Stripper data set in Figure 4.6.

With this higher beam energy, filtering techniques and particle identification further down the beamline benefit by having greater separation between the isotope of interest and the contaminants. Multiple single carbon foil charge state and terminal voltage combinations were tested, see Table 4.2. Some combinations gave beam energies that were too low to make the most of the particle identification further down the beamline which is discussed in more detail in later sections. Other combinations had good beam energies but were only achieved by working near the highest possible terminal voltage, where the accelerator is not stable for long periods of time. This instability is detrimental for measuring samples back to back, as any accelerator sparks will change the overall efficiency of the system and will require a lengthy retune. Finally, mass and charge state combinations that give an integer ratio tend to also have a higher background rate. This comes from mass, energy, and charge state combinations from other isotopes that have the same or similar analyzing magnet setting. These types of isotopic contamination can come from trace amounts of other elements in the cathode material that are not specifically prevalent but can be

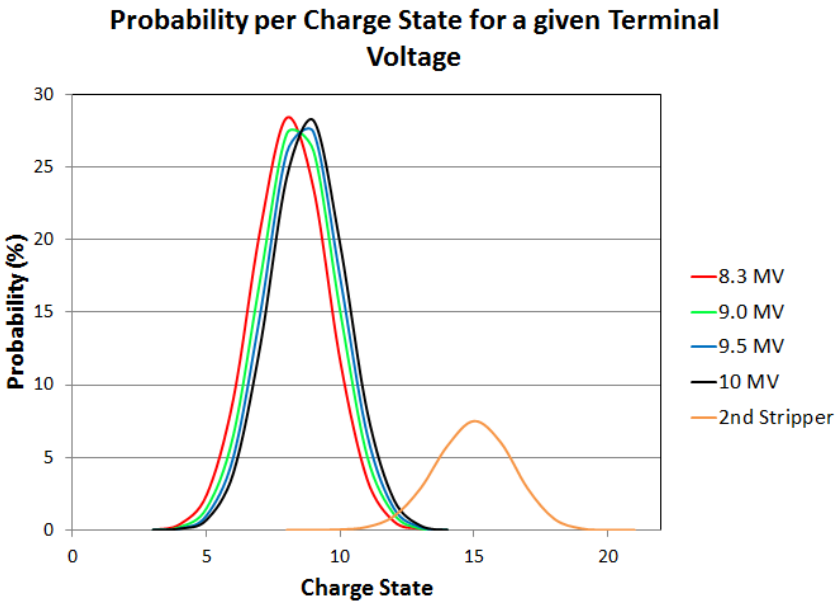

Figure 4.6. Percent Abundance for each charge states at a given accelerator terminal voltage for ^{56}FeO which breaks up in the first carbon stripper foil. As the terminal voltage increases the peak of the distribution of charge states also increases. The 2nd Stripper data set is the probability of available charge states when the 9+ charge state from the first stripper is selected for a terminal voltage of 8.3 MV. By using the second carbon foil, higher charge states are available but the overall percentage of the beam in those charge states is lower, therefore sacrificing total beam current.

detected with the AMS technique. Ultimately for this thesis, two carbon foils were used in the final experiments. The final probabilities for a terminal voltage of 8.3 MV are given in Figure 4.7. The single stripper data is shown in blue and follows the right axis. The second stripper data is shown for possible and prevalent charge states from the first stripper. As shown in the figure, high beam energies can be more easily reached by stripping the beam particles twice but at a much lower probability. For this thesis work, the 9+ charge state was selected from the first stripper (shown in black) and 16+ from the second stripper (one charge state higher than the peak in the distribution), giving a beam energy of 112.86 MeV and a probability of approximately 6%. Further details of how this is selected are in Section 4.2.4.

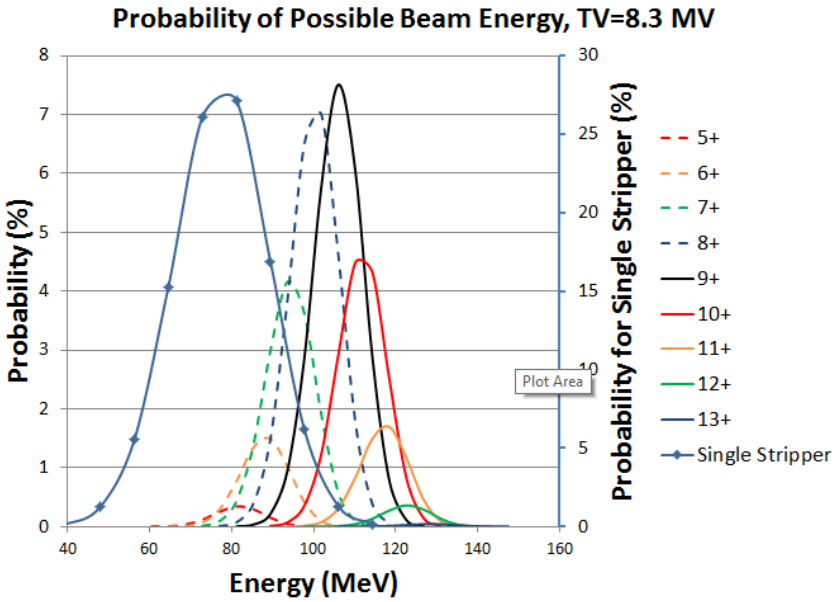

Figure 4.7. Final probability of possible beam energies from the second carbon stripper foil in the Tandem accelerator for ^{56}FeO which breaks up in the first carbon stripper foil. Each set of data is the distribution of energy for a given charge state from the first carbon foil. For example the solid black line is the final probability for a beam with a 9+ charge state from the first carbon foil. For comparison, single stripper data is shown in blue and uses the right y-axis.

TABLE 4.2

MULTIPLE TERMINAL VOLTAGE AND CHARGE STATE COMBINATIONS WERE TESTED GIVING A VARIETY OF ENERGIES FOR MASS 60

Terminal Voltage (MV)	Charge State, q	Energy (MeV)	Result
8.720	9+	87.2	Too low energy
8.760	10+	96.4	Mass/q=integer
9.702	9+	97.0	Accelerator not stable
9.575	11+	114.9	Accelerator not stable

4.2.4 Analyzing Magnet

The 90° analyzing magnet after the accelerator selects the particles that have a magnetic rigidity equal to the magnetic field of the magnet. The equation is as follows:

$$\mathrm{B}\rho = \frac{\sqrt{2\mathrm{ME}}}{q} \tag{4.3}$$

where B is the magnetic field, ρ is the radius of the particle's trajectory, M is the mass of the particle, E is the energy of the particle, and q is the final charge state of the particle. This effectively allows us to pick the charge state or charge state combination of the beam and therefore the energy of the beam.

4.2.5 Wien Filter and the Second Carbon Stripper Foil

Following the analyzing magnet is a Wien Filter located on the AMS beamline. The underlying process of a Wien Filter is shown in Figure 4.8. It consists of an

electric and a magnet field, perpendicular to each other and perpendicular to the beam direction. A particle that passes through this region will feel a force, $\vec{F} = q \cdot (\vec{E} + (\vec{v} \times \vec{B}))$ where q is the particle's charge, v is the particle's velocity, E is the Wien Filter's electric field, and B is the Wien Filter's magnetic field. A particle will be deflected unless its velocity is $v_o = E/B$ and the forces from the electric and magnetic fields exactly cancel each other. The Wien Filter can then deflect particles with velocities not equal to E/B out of the beam. Slits further down the beam pipe will stop the deflected particles from going further. This acts as a filter for isotopes with incorrect velocities which may manifest themselves as different masses, charge states, or some combination that manages to pass through the analyzing magnet.

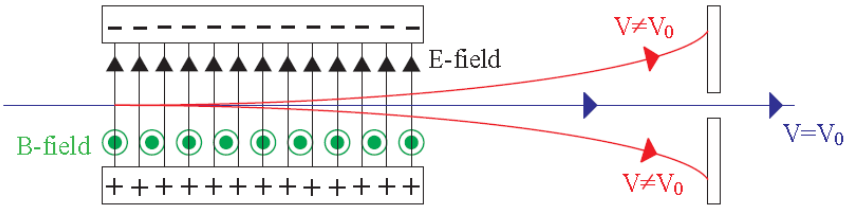

Figure 4.8. Schematic of the principles of a Wien Filter. An electric and magnet field are perpendicular to each other and to the direction of the particle's velocity. Particles that pass through this region will feel a force. If the particle's velocity is equal to the electric field divided by the magnetic field, the particle will pass through undeflected. Otherwise, the particle will be pushed up or down out of the beam, where it can be blocked by slits further downstream. Image taken from [38].

This filtering is especially necessary when the second carbon stripper foil in the FN accelerator is used as multiple charge state combinations may pass through the analyzing magnet for a particular setting. Work began on the possibility of using an existing second stripper in December 2014 as it gave us the option of accessing higher beam energies without needing to go to higher terminal voltages where the accelerator is only stable on the order of hours. As mentioned previously, instability in the accelerator in the form of discharges from the terminal to the tank walls for example, requires a new tune meaning data before and after a spark can not be correlated. Therefore, working at lower terminal voltages is preferred even if it means less overall beam current. Another downside to using the second stripper is that there are now multiple charge state combinations that will bend around the analyzing magnet at a particular setting and will reach the detectors, as illustrated in Figure 4.9. The Wien Filter can eliminate this problem and filter out the unwanted charge state combinations which will have different velocities than our chosen charge state combination, as shown in Figure 4.10. Wien Filter settings for a 9+ to 16+, doubly stripped beam with an energy of 112.86 MeV and a terminal voltage of 8.5 MV are listed in Table 4.3.

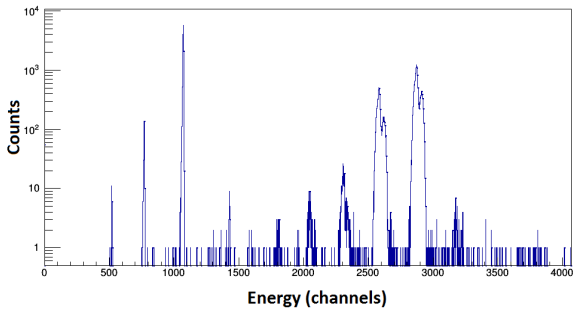

Figure 4.9. An example spectra from the silicon detector in the scattering chamber on the AMS beamline using a second stripped beam. The y-axis is counts per bin and the x-axis is energy deposited in the silicon detector in channels. The Wien filter is off. Each peak is a different charge state combination that pass through the analyzing magnet. The peak centered around channel number 3000 is our peak of interest at an energy of 112.86 MeV.

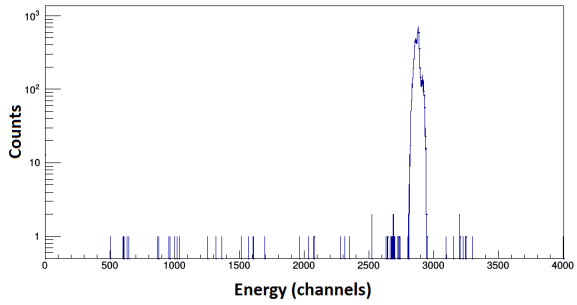

Figure 4.10. An example spectra from the silicon detector in the scattering chamber on the AMS beamline using a second stripped beam with the Wien filter turned on. The y-axis is counts per bin and the x-axis is energy deposited in the silicon detector in channels. The Wien filter will only allow one combination of charge states to pass through. The other combinations are bent away and filtered out of the beam.

TABLE 4.3

WIEN FILTER SETTINGS FOR THE ELECTRIC PLATES AND THE MAGNETIC FIELD FOR EACH OF THE THREE MASSES OF IRON ISOTOPES

Mass, A	Electric Plates		Magnetic Field [a]
	Input Value [b]	Physical Value [c]	
56	8.45	-47.6 kV	0.1096 T
		+48.8 kV	
58	8.30	-46.8 kV	0.1096 T
		+48.0 kV	
60	8.16	-46.1 kV	0.1096 T
		+47.3 kV	

[a]The magnetic field is an approximately reading from off of the true beam path. Therefore the magnetic field that the beam particles feel is, in truth, different than this value.

[b]Input values for the electric plates refer to the value sent by the LabView front panel control.

[c]The physical values are the true voltage placed on the plates, both positive and negative.

4.2.6 Gas Filled Magnet (GFM) Mode

After the isotopic selections from the SNICS magnet, Analyzing magnet, and the Wien Filter, isobars still contaminate the beam. These isobaric contaminants can be distinguished by using the Gas-Filled Magnet (GFM) technique which makes use of a 90° dipole magnet located at the end of the beamline. The specifications of this magnet are given in Table 4.4. Located then at the exit of the magnet are two

detectors for particle identification which are discussed in detail in the next section.

TABLE 4.4

SPECTROGRAPH MAGNET SPECIFICATIONS

Orbital Radius	1000 mm
Deflection	90°
Max Field	1.2 Tesla
Pole Gap	50.8 mm
Gas-filled Operating Parameters	
Gas	N_2
Pressure	1-10 Torr
Entrance Window	350 μg/cm^2 mylar
Detection	Parallel Grid Avalanche Counter Backed by Ionization Chamber

As shown in the left panel of Figure 4.11, the ion of interest and isobaric contaminant will take the same path through a magnetic field, in vacuum. If a thin window of mylar is placed in the beam's path, the beam will split into various charge states due to the charge exchange interactions with the thin window. However, the isobaric contaminant will still take a similar path to the ion of interest (center panel). Filling the magnetic field region with gas, such as nitrogen, typically on the order of 1 to 2 Torr, will cause the particles to coalesce around a mean charge state that is primarily

dependent on the number of protons. Therefore, the isobaric contaminants will take a different path through the magnet than the ion of interest (right panel). The mean charge state can be calculated through the following equation, [41]:

$$\bar{q} = Z\left(1 - 1.08\exp\left(-80.1 \cdot Z^{-0.506} \cdot \left(\frac{v}{c}\right)^{0.906}\right)\right), \tag{4.4}$$

where Z is the number of protons of a particle and v is the velocity of the particle (which is the same for each isobar). For iron and nickel at an energy of 112.86 MeV, the mean charge state for iron is 18.096 and for nickel, the mean charge state is 19.081.

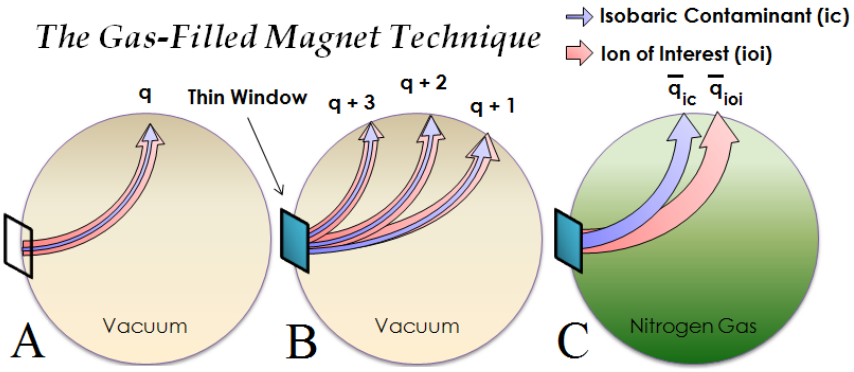

Figure 4.11. Illustration of the Gas-Filled Magnet Technique used to filter out isobaric contaminants. When two isobars pass through the magnetic field of the spectrograph magnet, both will follow a similar path as they have the same charge state, mass, and energy (A). When the isobars pass through a thin mylar plastic window, they undergo charge exchange and split into several different charge states. However, they still follow similar path through the magnetic field (B). Further, when the magnetic field region is filled with a low pressure gas (N_2) as well, then the two isobars undergo more charge exchange with the gas and coalesce around a mean charge state (C). The resulting mean charge state for each isobar is related to the number of protons and therefore each isobar would take a different path through the magnet. Figure courtesy Matthew Bowers.

4.2.7 Particle Identification

Identification of the particles that pass through all of the filters occurs after the spectrograph magnet. Two detectors are located at the exit of the magnet. The first, a Parallel Grid Avalanche Counter, is used to measure the position of the particle as it exits the magnetic field. The second, an Ionization Chamber, measures the energy loss of the particle.

Both detectors make use of the fact that heavy, positively charged particles interact with an absorbing medium through the Coulomb force between their positive

charge and the orbital electrons of the medium. Energy is transferred to the orbital electron from the incoming particle. This interaction can either excite the orbital electron or completely remove it from its atom. The incoming particle loses energy and slows down as a result. This leaves a trail of excited electrons or ion pairs in the absorbing material as the charged particle passes through. By suppressing the recombination of the ion pairs, they can be used for detection. The total number of pairs made along the particle's track is important for the detection signal. In the following sections, the technical details of the Parallel Grid Avalanche Counter and the Ionization Chamber are described.

4.2.7.1 Parallel Grid Avalanche Counter (PGAC)

The charged particle, after bending through the Spectrograph magnet, will first encounter the Parallel Grid Avalanche Counter (PGAC) detector. An electric field is set up in the volume by a voltage difference applied between an anode and two cathode grids. The placements of these grids are shown in the upper panel of Figure 4.12. In between these grids are two additional wire grids: one for detecting the x-position and one for detecting the y-position (not implemented) of an incoming particle. The x-position is effectively the difference in trajectories of the isobars as they pass through the GFM, as illustrated in Figure 4.11. The y-position is perpendicular to both the x-direction and the beam direction. The position grids are made of 20 micrometer gold-plated tungsten wire with a spacing of 1.25 millimeters. Continuously flowing isobutane gas, C_4H_{10}, maintained at a typical pressure of 3 Torr, is used as the absorbing medium. As the particle passes through the gas, ion pairs are created. Ions are accelerated toward the cathode and electrons are accelerated toward the anode due to the electric field that is set up by the applied voltages across the detector. The electrons will collide with other gas particles, releasing more electrons and causing an avalanche effect. This will induce a signal in one of the wires in the

grid.

The x-position grid and the anode grid are separated electrically into two halves, left and right. Figure 4.13 shows the left side of the x-position grid and the anode and how the signal is generated. A signal in the left side of the anode starts the timing of an event. The signal in the X position grid will split into two: one travels to the left and the other to the right. Each signal goes through a series of delay chips. These delayed signals will be the stop for the event timing. The difference in the timing of the two stop signals can be related to the position where the signal originated. The delay chips help to increase the differences in the timing. The right side of the detectors works the same. The PGAC can then be referred to as four "pieces": LL (left left) is leftmost of the left side of the detector, LR (left right) is rightmost of the left side, RL (right left) is leftmost of the right side, and RR (right right) is rightmost of the right side. All four pieces are physically a part of the same grid. The electrical separation is in the middle, between LR and RL.

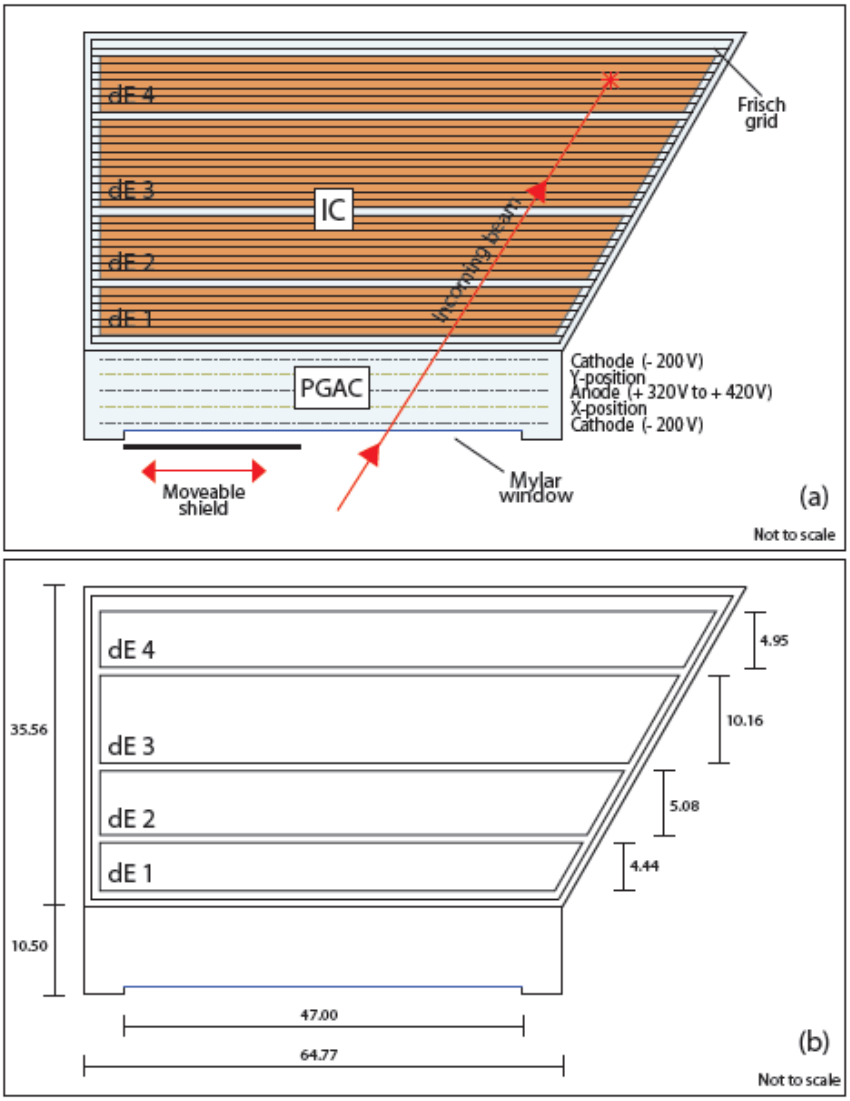

Figure 4.12. Schematic of the Parallel Grid Avalanche Counter and Ionization Chamber used for Accelerator Mass Spectrometry measurements. a) Approximate positions for grids, anodes, cathodes, and mylar windows for both detectors. b) Dimensions for both detectors in centimeters. Note: The IC and PGAC are separated by an extra 0.635 cm by an addition aluminum piece that isolates the two with a mylar foil [38].

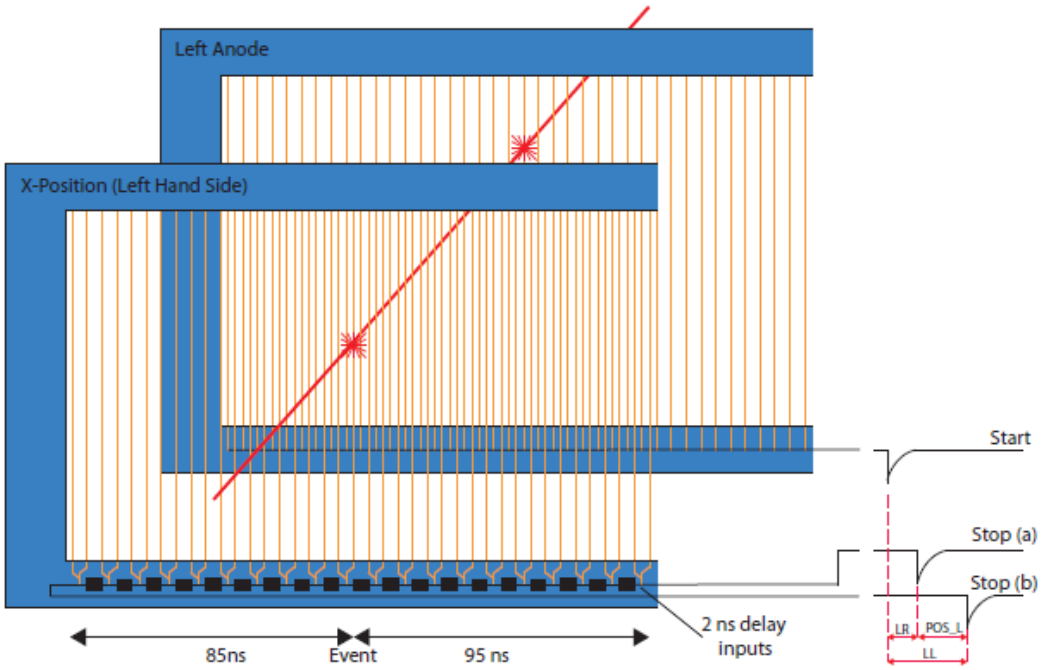

Figure 4.13. How the PGAC generates a position signal [38]. The anode is used as the start signal and the delayed signals from the position grid are used as the stop signal. The signal generated in the position grid is sent in two separate directions, to the right and to the left as shown. The difference in the time for each of these two signals results in the position of the event. As shown here, the event generates a signal that goes to the right, with a delay of 95 nanoseconds and a second signal going to the left, with a delay of 85 nanoseconds plus an additional 180 nanoseconds to return to the right. The difference then relates to the physical position of the event.

4.2.7.2 Ionization Chamber (IC)

The medium for the IC is also isobutane and with the use of a wire support grid between the IC and the PGAC, the IC can hold pressures up to 50 Torr. The interaction process between the gas and the incoming charged particle will cause the particle to lose energy and, if conditions are right, the particle will come to a complete stop within the gas. The energy loss per path length for a certain particle in a given

material is called the linear stopping power, S = -dE/dx. Another way to express the rate of energy loss is the Bethe-Bloch formula, Equation 4.5,

$$-\frac{dE}{dx} = \left(4\pi e^4 z^2/m_o v^2\right) \times NB \tag{4.5}$$

where B is $Z \times \left[\ln\frac{2m_o v^2}{I} - \ln\left(1-\frac{v^2}{c^2}\right) - \frac{v^2}{c^2}\right]$, v is the velocity of the primary particle, ze is the charge of the primary particle, N is the number density of the absorber, Z is the atomic number of absorber, m_o is the rest mass of the electron, and I is the average ionization and excitation potential of the absorber.

The Bragg curve describes the rate of energy loss as a function of the distance traveled in the material. This can be obtained by plotting Equation 4.5 as a function of the depth inside the material. For most of the path through the absorber, the energy loss is proportional to 1/E. Near the end of the track, the energy loss rate spikes and then the Bragg curve falls off drastically as the particle losses all of its energy as illustrated in Figure 4.18.

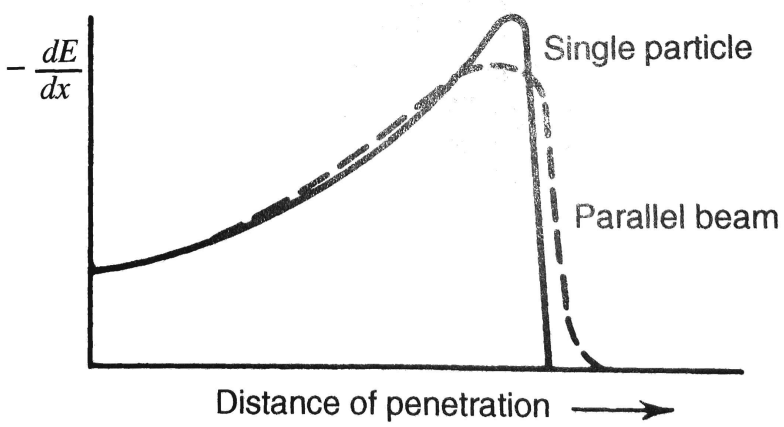

Figure 4.14. Example of a typical Bragg Curve, where dE/dx, the rate of the energy loss, is plotted as a function of distance into an absorbing medium [24]. The plot shows the behavior of a single particle and a beam of particles of the same initial energy. The difference in the two is due to energy straggling, which comes from the statistically random energy loss due to interactions between the beam particles and the absorbing medium.

The anode for the IC is split into four sections in order to look at different points along the Bragg curve for the incoming particles. A perpendicular electric field is set up across the detector with a potential difference between the cathode and anodes. The voltages used are set differently depending on the energy of the specific ion being measured. A wire grid, called a Frisch grid, is placed near the anode, such that all beam particles pass between the cathode and the Frisch grid, as generically illustrated in Figure 4.15. No signal is generated by the electrons as they drift toward the Frisch grid, which is at ground. Once they pass through the Frisch grid, the anode-grid voltage begins to drop and a signal voltage develops across the resistor. This setup eliminates the position-sensitive aspect of the electrons generated. Without the grid, electrons produced close to the anode would cause a smaller signal than

those produced farther away because of the path length for the electron. The signal is now proportional to the total number of ion pairs formed and is independent of the position. This system allows us to measure the total energy lost by the particle in each section of the detector. We use this information and the Bragg curve formula to help determine the identity of each isotope passing through the detector.

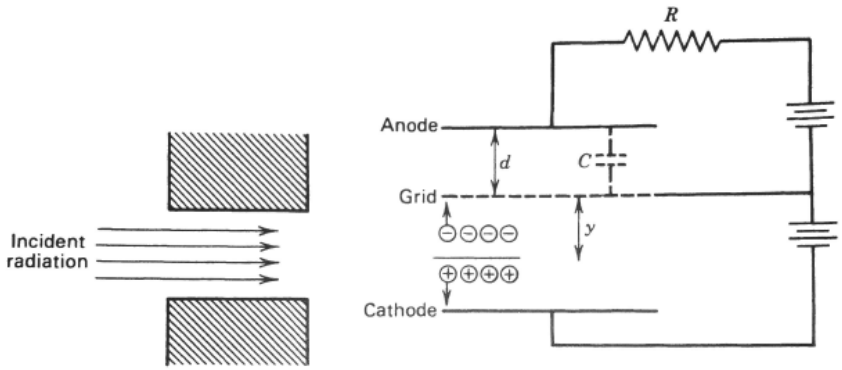

Figure 4.15. Placement of Anode, Cathode, and Frisch Grid for an Ionization Chamber. This configuration ensures that all incoming particles pass between the Frisch Grid and the Cathode. All of the electrons will cross the Frisch grid, held at ground, and travel the same voltage drop from the Frisch grid to the anode where the signal is generated. This makes the signal independent of the original position of the event. [24]

4.2.8 GFM and Detector Settings

In the following two sections, spatial and energetic separation is described, including how the settings for the GFM technique and the detectors were chosen for this dissertation.

4.2.8.1 Optimizing for Spatial Separation

By using the GFM technique described in Section 4.2.5, we can spatially separate ^{60}Ni from ^{60}Fe in the beam. Figure 4.16 illustrates this concept using ^{58}Ni and ^{58}Fe as a proof of principle.

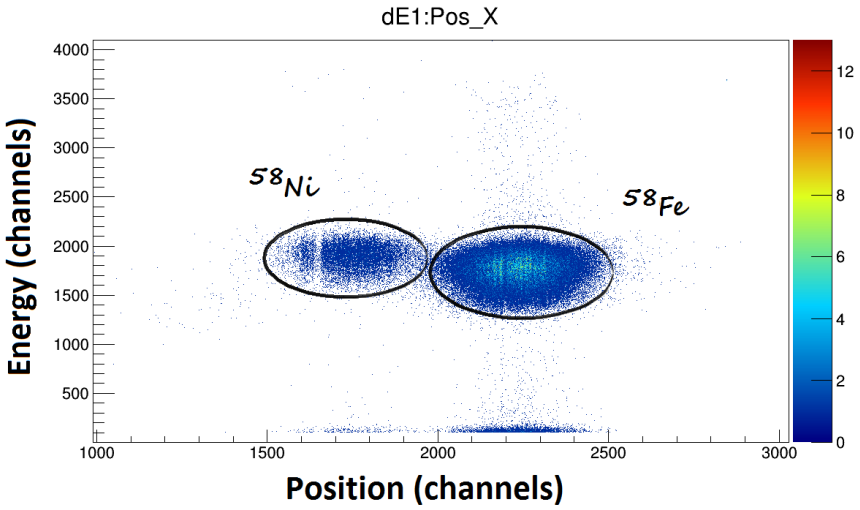

Figure 4.16. Energy loss in the first anode, dE1, (y-axis) versus position (x-axis), both in channels, for ^{58}Ni and ^{58}Fe. By using the GFM technique, nickel and iron will take slightly different paths through the spectrograph magnet and will register different positions on the PGAC detector. The gap in the ^{58}Ni beam comes from the gap between the two halves of the PGAC detector.

Settings for GFM mode are typically 1-2 Torr of nitrogen gas in the spectrograph magnet, separated from the upstream beamline by a 350 μg/cm^2 mylar window just before the entrance into the magnet. The gas pressure is set based on a combination of the separation in the centroids of nickel and iron and the full width at half maximum

of the two peaks in the PGAC detector. As illustrated in Figure 4.17, there is an optimum pressure where the width of the position spectra is at a minimum, balancing out the narrowing of the peak due to collisions with the gas particles, causing an averaging of the trajectories and the broadening due to scattering and energy loss straggling. Furthermore, higher pressure in GFM mode causes the beam particles to lose more energy before entering the two detectors due to collisions with the gas in the magnet. This energy loss is also a factor in how much gas to use for GFM mode. Too much energy loss may not allow us to use further energy separation techniques efficiently. A final consideration for gas pressures in GFM mode is to keep the pressure at or below the gas pressure in the PGAC. A higher gas pressure in the magnet would cause the mylar window separating the detector and the spectrograph magnet to bow into the wires inside the PGAC detector, creating electrical and data collection issues.

For this work, nitrogen gas at a pressure of 1.5 Torr for GFM mode, resulted in the best physical separation between the nickel and iron centroids without sacrificing too much beam energy.

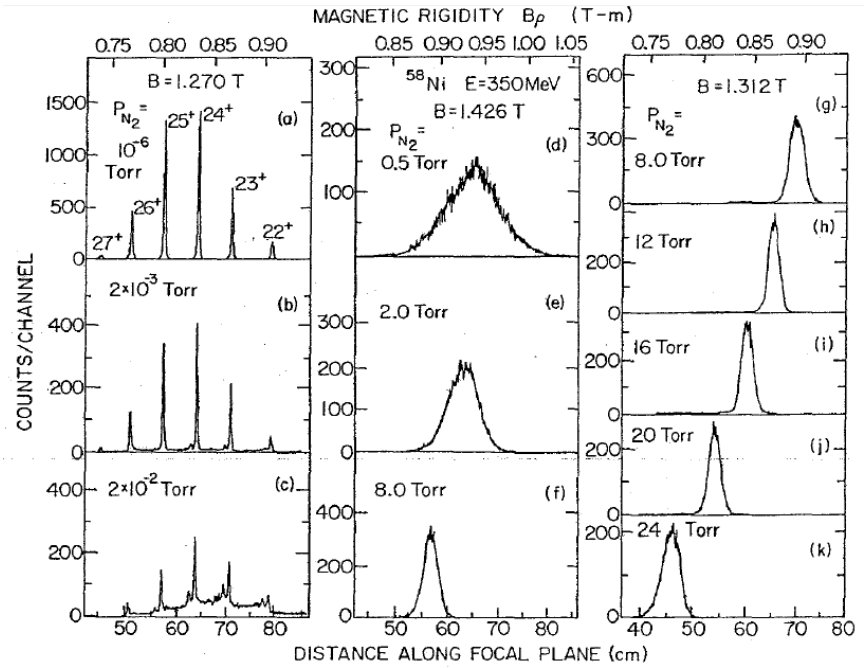

Figure 4.17. Focal-plane position spectra for ^{58}Ni ions with an incident energy of 350 MeV measured with an Enge split-pole magnetic spectrograph at Argonne National Laboratory filled with nitrogen at different pressures as specified. Image taken from [36]. Following the individual plots from (a) in the upper left corner to (k) in the lower right corner, the pressure in the spectrograph magnet is increased. Once the pressure is high enough (d), the individual charge states will coalesce around a mean charge state. Increasing the gas pressure further will narrow the peak as the charge is more focused around the mean charge state. The peak will begin to broaden again as shown in (k). This results from the competition between narrowing due to the higher number of collisions with the gas particles, causing a better statistical averaging of the trajectories and the broadening due to small angle scattering and energy loss straggling.

4.2.8.2 Optimizing for Energetic Separation

The final step is to separate nickel and iron energetically. After the beam passes through the PGAC, it enters the IC detector for Bragg curve spectroscopy. As shown in Figure 4.12, the IC is split into four anodes allowing us to look at four sections

of the incoming particle's Bragg curve as it passes through the detector. Figure 4.18 shows the simulated Bragg curves of iron and nickel from a 112 MeV beam. In this simulation, the beam reaches the detectors after passing through several mylar windows and 1 Torr of nitrogen gas in GFM mode. With the resulting energy loss, the simulated beam has an energy of about 60 MeV when it enters the IC.

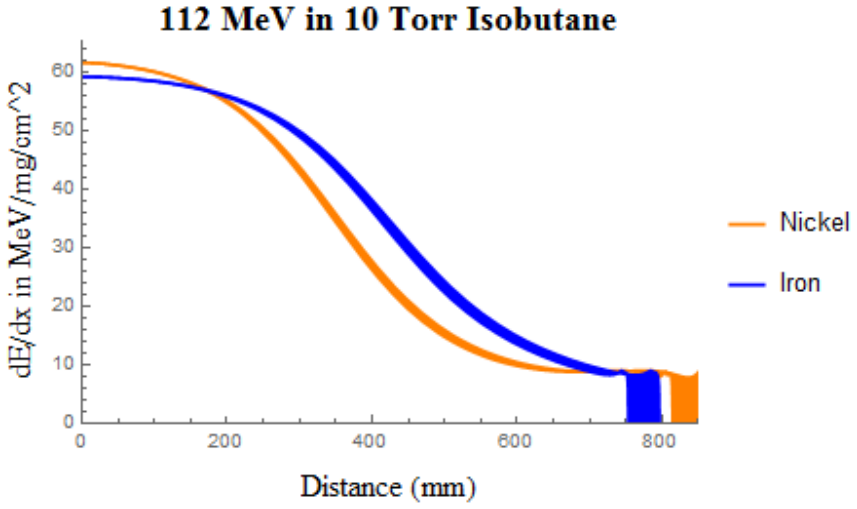

Figure 4.18. Simulated Bragg curves from the program SRIM for nickel and iron in the IC with an incoming energy near 60 MeV. Energy loss is on the y-axis in units of MeV/mg/cm^2 and distance through the gas in millimeters is on the x-axis. Nickel is shown in orange and iron is shown in blue. The thickness of the lines indicate the errors in the simulation. Toward the lower ranges of energy, the simulation from SRIM is not as accurate and errors are large. From this, we can expect nickel to have a higher rate of energy loss in the first part of the IC and iron to have a higher rate later in the IC. This leads to the concept of crossover, or the point where nickel and iron are losing at the same rate.

As illustrated, nickel has a higher rate of energy loss than iron initially. After about 200 mm of 10 Torr isobutane, iron will have a higher energy loss rate in this simulation. This occurrence, referred to as crossover, allows us to use the fact that nickel and iron swap roles as the highest rate of energy loss. By tweaking the gas pressure in the IC, the first anode will contain the part of the Bragg curve where nickel is losing energy at a faster rate. In the second anode, nickel and iron will have the same rate of energy loss. Finally, in the third anode, iron will lose energy at a higher rate than nickel. This is illustrated in the following Figure 4.19. The crossover technique is a feature of the analysis and helps to separate background from real signal. By using this crossover technique, gates, or cuts, on the data can be made on the regions of interest in anode 1 (dE1) and anode 3 (dE3), removing most of the background contamination from ^{60}Ni.

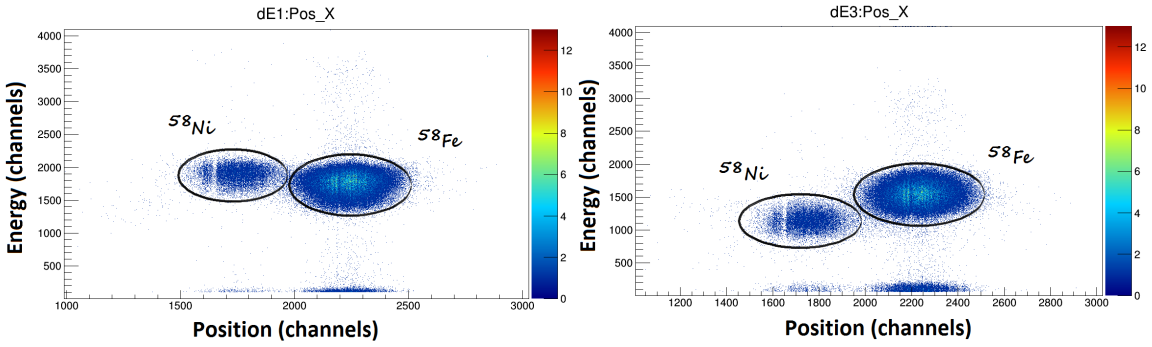

Figure 4.19. Example spectra showing the crossover technique. For both spectra, the y-axis is energy loss in channels and the x-axis is position in channels. The left spectra is the energy loss in anode 1 (dE1) and the right spectra is the energy loss in anode 3 (dE3). In dE1, nickel is losing energy faster than iron and in dE3, iron is losing faster than nickel. Note, that the gains for the preamplifiers are different between dE1 and dE3, so the energy loss is not to scale. This example is for mass 58 but this is a good approximation of the behavior observed at mass 60.

Another technique that can be used is to change the gas pressure in the IC until the greatest separation is found in one of the anodes, dE3 for example (which is the largest anode by area). From Figure 4.18, the greatest separation will happen by forcing as much of the Bragg curve after the crossover point into one anode. This can be achieved by increasing the gas pressure in the IC.

For this work, the crossover technique was used and resulted in a background concentration on the order of 10^{-12} ^{60}Fe/^{56}Fe. This is sufficient for our measurement which has a sample with an estimated lowest concentration of 10^{-9} ^{60}Fe/^{56}Fe. Example spectra of a background measurement from the November 2015 experiment are shown in Figure 4.20, and the unknown sample Fe-1 in Figure 4.21. The November 2015 settings for both detectors can be found in Table 4.5. The electronics setup for collecting the data can be found in Appendix A.

As the isobar contaminant ^{60}Ni is more prevalent than the ion of interest ^{60}Fe, the number of beam particles, both nickel and iron, will be too high and can overload the detectors. Since nickel and iron take slightly different paths through the spectrograph magnet, an aluminum sheet, or shield, can be placed immediately before the PGAC, as illustrated in Figure 4.12. This shield can be moved into position remotely to block some of the contaminant beam. Keeping the count rate in the detectors at a reasonable level will prevent overload. This manifests itself in the spectra below as a sharp cutoff, which will depend on the shield's position.

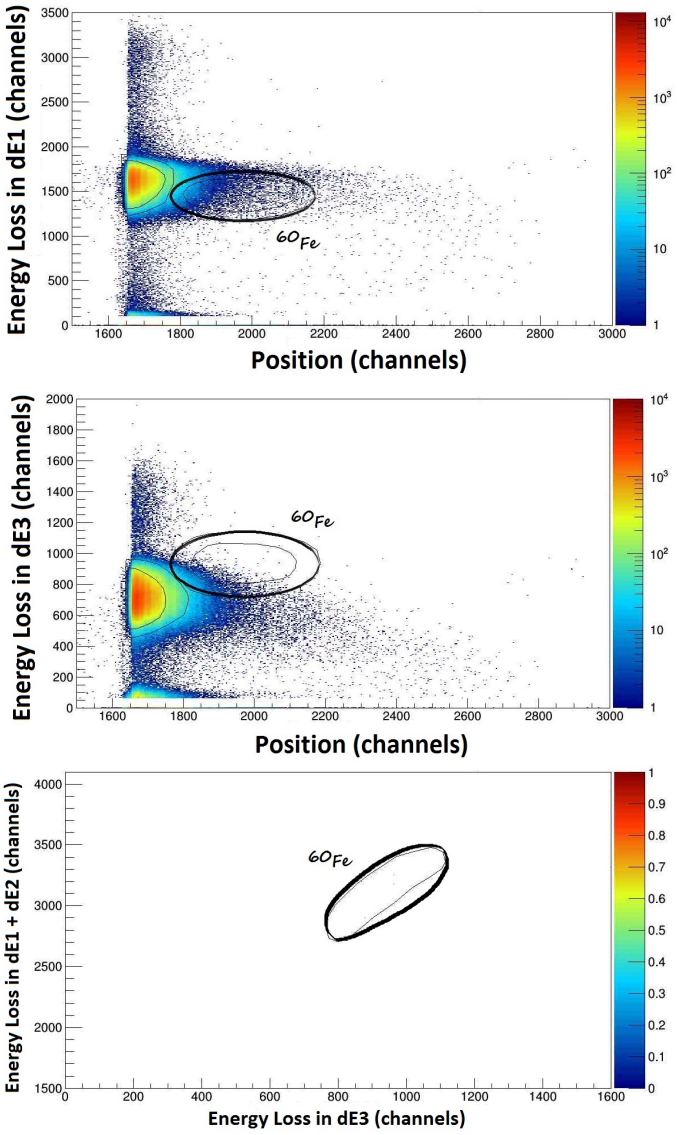

Figure 4.20. Example background spectra from a blank sample (material that contains no ^{60}Fe). Top: Spectrum for dE1 (y) versus position (x) of blank material. Part of the ^{60}Ni peak is blocked by an aluminum plate, located before the PGAC. The location for ^{60}Fe is highlighted. Middle: Spectrum for dE3 (y) versus position (x) for the same material. The location of ^{60}Fe is highlighted. Bottom: Spectrum of the energy loss in dE1 plus dE2 (y) versus the energy loss in dE3 (x). The cuts from dE1 and dE3 have been applied and only four counts pass these cuts for this sample. The background concentration is measured as approximately 2×10^{-12}. The regions of interest for each spectrum were determined from the Fe-1 sample as illustrated in Figure 4.21.

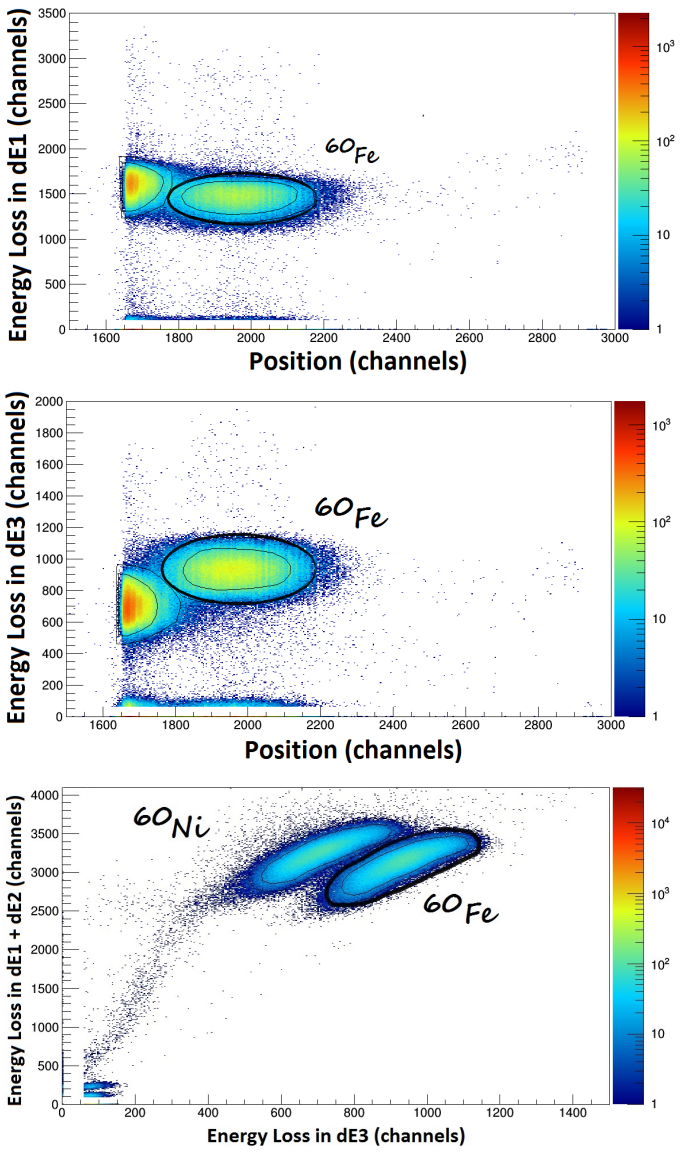

Figure 4.21. Example spectra for the Fe-1 sample, which contains the highest ^{60}Fe/^{56}Fe concentration of all of our samples. Top:Spectrum for dE1 (y) versus position (x) of the Fe-1 sample. Part of the ^{60}Ni peak is blocked by an aluminum plate, located before the PGAC. The location of the ^{60}Fe is highlighted. Middle: Spectrum for dE3 (y) versus position (x) for the same material. The location of ^{60}Fe is again highlighted. Bottom: Spectrum of the energy loss in dE1 plus dE2 (y) versus the energy loss in dE3 (x). The locations of the ^{60}Ni and the ^{60}Fe peaks are highlighted. The cuts used for the analysis are based off of runs on the Fe-1 sample due to the prevalence of the ^{60}Fe peaks.

TABLE 4.5

GFM AND DETECTOR NOVEMBER 2015 SETTINGS INCLUDING GAS PRESSURES AND DETECTOR VOLTAGES

	Gas Pressure	Anode Voltage	Cathode Voltage
GFM Mode	1.5 Torr	-	-
PGAC	3.0 Torr	+265 Volts	-390 Volts
IC	9.0 Torr	+400 Volts	-300 Volts

4.3 Measurement Method and Results for the November 2015 Experiment

With the settings finalized and the background concentration at a reasonable level during the November 2015 experiment, measurements on the samples could be done. To account for any unquantifiable losses of beam particles through the accelerator and the beamline, our unknown material (Fe-1) was measured relative to a standard material (Fe-4). The Fe-4 material was measured accurately by Wallner, et al. [47] using the $^{60}Fe/^{55}Fe$ technique discussed in Chapter 2, and can be used as a standard. The concentration of Fe-4 was reported as $(2.095 \pm 0.089) \times 10^{-9}$ $^{60}Fe/^{56}Fe$. A background measurement on blank material was done first, followed by a measurement of the standard material, Fe-4. Lastly, the unknown material (Fe-1) was measured. For each, (background, Fe-4, and Fe-1) six five-minute runs were performed totaling 30 minutes on each. This was repeated twice. The ^{56}Fe current at the ion source was measured before and after each run. The transmission of the beam was also measured at the start of each sample and again at the end. The transmission refers to the percentage of the beam that is transported through the full system and

is a ratio of the current at the Faraday cup in the Scattering Chamber on the AMS beamline and the current at the SNICS Faraday cup after the LE magnet, accounting for the charge states at each cup. To ensure that the beam current and transport are stable over time, measurements are taken of the transmission before and after each sample. Both of these, beam current and transmission, factor into the concentration calculation as

$$\text{Concentration} = \frac{\text{Counts of } ^{60}\text{Fe}}{\text{time}} \times \frac{100}{\text{Transmission } \%} \times \frac{1}{\text{Beam Current}} \tag{4.6}$$

Counts of ^{60}Fe is the number of counts in the region of interest, transmission is in percentage, and the beam current is in ^{56}Fe particles per second.

Each set of six runs for a sample or background was treated as one continuous run, summing the counts from each individual run. The transmission measured before and after the sample was averaged. An average was also taken between the first and last ion source ^{56}Fe current reading. The resulting raw concentrations are shown in Table 4.6, with futher details in Appendix C.

The background concentration, as shown in Figure 4.20, is two orders of magnitude lower than the standard Fe-4. Therefore, the background subtraction on the Fe-4 concentration had a minimal effect. No subtraction was performed on the Fe-1 sample as it is five orders of magnitude higher in concentration than the blank material, as shown in Figure 4.21. After the background subtraction was done on Fe-4, the scale factor was determined (nominal value of Fe-4 divided by the measured value of Fe-4, as shown in Equation 4.7 where "raw" is the measured value and "true" is the nominal value of Fe-4) and found to be 2.808 for the first round and 2.273 for the second round. These scale factors were applied to the corresponding Fe-1 raw concentration, as shown by Equation 4.8 where "raw" is the measured value and the "true" is the nominal value, for each round.

$$\text{Scale Factor} = (\text{Fe-4}_{\text{true}})/(\text{Fe-4}_{\text{raw}} - \text{Background}_{\text{raw}}) \quad (4.7)$$

$$\text{Fe-1}_{\text{true}} = \text{Fe-1}_{\text{raw}} \times \text{Scale Factor} \quad (4.8)$$

A weighted average of the two Fe-1 values measured is $(2.066 \pm 0.242) \times 10^{-6}$ ^{60}Fe/^{56}Fe. The error mostly comes from the statistical error on the Fe-4 counts in the region of interest at approximately 15%. Current readings for the ion source had an assigned error of 1% and for the Scattering Chamber Faraday cup, 5%. Improvements to the error would come from increasing the number of counts in the region of interest by either increasing the output of the ion source or measuring the sample for a longer time period. Knowing from the chemistry steps in Chapter 3 that 4.95×10^{20} ^{56}Fe atoms were added to Fe-1, the number of ^{60}Fe atoms in the full Fe-1 sample is 1.023×10^{15} (the measured and scaled ^{60}Fe/^{56}Fe concentration multiplied by the added ^{56}Fe).

TABLE 4.6

RAW DATA FROM THE EXPERIMENT IN NOVEMBER 2015

Sample [a]	Time (seconds)	Initial ^{56}Fe (nA)	Final ^{56}Fe (nA)	Average ^{56}Fe (pps)[b]	Average Transmission (%)	Total Counts	Raw Concentration (^{60}Fe/^{56}Fe)
Background	1668.138	60.080	54.161	3.5700×10^{11}	0.534	8	2.517×10^{-12}
Fe-4	1636.242	1.473	1.219	8.4114×10^{9}	0.408	42	7.487×10^{-10}
Fe-1	1753.529	3.746	3.768	2.3480×10^{10}	0.544	176977	7.901×10^{-7}
Background	1651.215	67.012	63.396	4.0752×10^{11}	0.535	8	2.221×10^{-12}
Fe-4	1686.808	1.259	1.017	7.1113×10^{9}	0.424	47	9.238×10^{-10}
Fe-1	1757.152	3.049	3.214	1.9570×10^{10}	0.515	153563	8.667×10^{-7}

[a]Each row represents the summation of six five minute runs. The raw concentration is calculated using Equation 4.6 and is unscaled. More detailed information for each run can be found in Appendix C.

[b]particles per second

4.3.1 Second Attempt during the May 2016 Experiment

With a 15% error for the concentration as shown above, a second attempt was made in similar conditions in May 2016, several months after the first attempt. The same energy and charge state combination were chosen at the analyzing magnet, specifically 112.86 MeV and 9+ to 16+. However with each tuning of the accelerator system, some settings are slightly different. This is most notable in the bias voltage on the SNICS ion source platform and the accelerator terminal voltage. The settings used are shown in the tables below. Table 4.7 shows the settings for the SNICS ion source, Table 4.8 shows the settings for the Wien Filter (electric plates and magnetic field), and Table 4.9 shows the settings for the detectors (gas pressures and voltages). Most differences between these settings and the settings from the November 2015 experiment are related to the new tune of the pilot beam, ^{56}Fe. One major, supposed difference is in the magnetic field of the Wien Filter. The magnetic field value, however is measured using a Hall Probe that is off-axis from the beam itself. The probe had also been moved to a slightly different location between the two measurements. Therefore the magnetic field is not an accurate representation of the true field that the beam particles experience. Maximizing the count rate on the detector (for a mass-60 beam) or the current on a Faraday cup (for the pilot beam, ^{56}Fe) with the electric plate settings can correct for small differences in the true magnetic field.

The goal was to collect more counts in the region of interest for the standard material, Fe-4. The error on the standard during the November 2015 experiment was a major source of error for the calculated half-life value. More counts in the region of interest decreases the error overall significantly. This can be achieved by either collecting data at the same count rate for a longer period of time or by producing more from the ion source, causing a greater count rate at the detectors. Maintenance and general cleaning of the ion source had occurred several weeks prior to this second

attempt, allowing us to produce almost an order of magnitude more ^{56}Fe current at the SNICS Faraday cup. With the significant increase of production and a slightly higher transmission through the system, the count rates at the detectors were greater by an order of magnitude. To prevent overloading the detectors, the aluminum shield was brought in farther to block more of the ^{60}Ni isobar, without blocking any of the ^{60}Fe beam. Even with this, the detectors' dead time was more significant than in previous experiments. In the end, the high count rate allowed us to collect data for a shorter amount of time. Raw data including ^{56}Fe currents, transmission, time, and counts in the region of interest are shown in Appendix C in Table C.2.

Another source of error was the ^{56}Fe current reading at the Scattering Chamber Faraday cup. By integrating this current reading for more than 10 seconds, such as is done with the SNICS Faraday cup reading, we can decrease the assigned error from 5% to 1%. Overall the total error on the AMS measurement between November 2015 and May 2016 changed from around 12% to about 5%.

TABLE 4.7

SETTINGS FOR SNICS DURING THE MAY 2016 EXPERIMENT

	SNICS Component [a]	Digital Readout
Ion Source	Ionizer Current	19.07 A, 105 W
	Cathode Voltage	3.15 kV
	Extractor Voltage	15.20 kV
	Focus Voltage	3.75 kV
	^{56}Fe Bias Voltage	57.07 kV
	^{58}Fe Bias Voltage	55.19 kV
	mass 60 Bias Voltage	53.22 kV
	LE Magnet Current	53.22 A

[a]Ionizer current, Cathode voltage, Extractor voltage, Focus voltage, and the Magnet current will remain the same for each mass. By changing the Bias voltage, different masses will be bent through the SNICS Magnet. The Cathode voltage plus the Extractor voltage plus the Bias voltage is the energy of the beam as it exits the ion source. The Ionizer current relates to the amount of cesium that is sputtered and the focus voltage relates to the beam tune.

TABLE 4.8

WIEN FILTER SETTINGS DURING THE MAY 2016 EXPERIMENT FOR THE ELECTRIC PLATES AND THE MAGNETIC FIELD FOR EACH OF THE THREE MASSES OF IRON ISOTOPES

Mass, A	Electric Plates		Magnetic Field [a]
	Input Value [b]	Physical Value [c]	
56	8.48	-47.8 kV	0.11325 T
		+49.0 kV	
58	8.33	-47.0 kV	0.11325 T
		+48.2 kV	
60	8.23	-46.5 kV	0.11325 T
		+47.7 kV	

[a]The magnetic field is an approximately reading from off of the true beam path. Therefore the magnetic field that the beam particles feel is, in truth, different than this value. For this second attempt, the Hall Probe used to measure the magnetic field was in a slightly different location on the magnet compared to the first experiment in November 2016. This explains the difference in the magnetic fields between the two.

[b]Input values for the electric plates refer to the value sent by the LabView front panel control.

[c]The physical values are the true voltage placed on the plates, both positive and negative.

TABLE 4.9

GFM AND DETECTOR FINAL SETTINGS DURING THE MAY 2016 EXPERIMENT INCLUDING GAS PRESSURES AND DETECTOR VOLTAGES

	Gas Pressure	Anode Voltage	Cathode Voltage
GFM Mode	1.5 Torr	-	-
PGAC	3.0 Torr	+250 Volts	-385 Volts
IC	9.0 Torr	+400 Volts	-300 Volts

The following plots are examples of the data taken. Figure **??** shows spectra on a mass-58 beam, including ^{58}Ni and ^{58}Fe. This, again shows the crossover between nickel and iron, where nickel is losing energy at a faster rate in anode 1 and iron is losing energy faster in anode 3. As before, mass 58 is a good approximation of the behavior that exists at mass 60. The next figure, Figure 4.23 shows the standard material, Fe-4 and the last figure, Figure 4.24 shows the unknown material, Fe-1. The top two spectra in each figure are the energy loss in anode 1 (left) and anode 3 (right) versus position. The bottom spectrum for each figure is the energy loss combination of anode 1 and 2 versus anode 3. As before, an aluminum shield is partially blocking the nickel peak, which prevents detector overload. For the Fe-4 sample, the ^{60}Fe peak is difficult to identify in the individual anode spectrum but is easily seen in the energy loss versus energy loss spectra of Figure 4.23. The cuts used on the data are from the Fe-1 sample as the peaks are more prevalent in both the energy loss versus energy loss spectrum and the individual anode spectra.

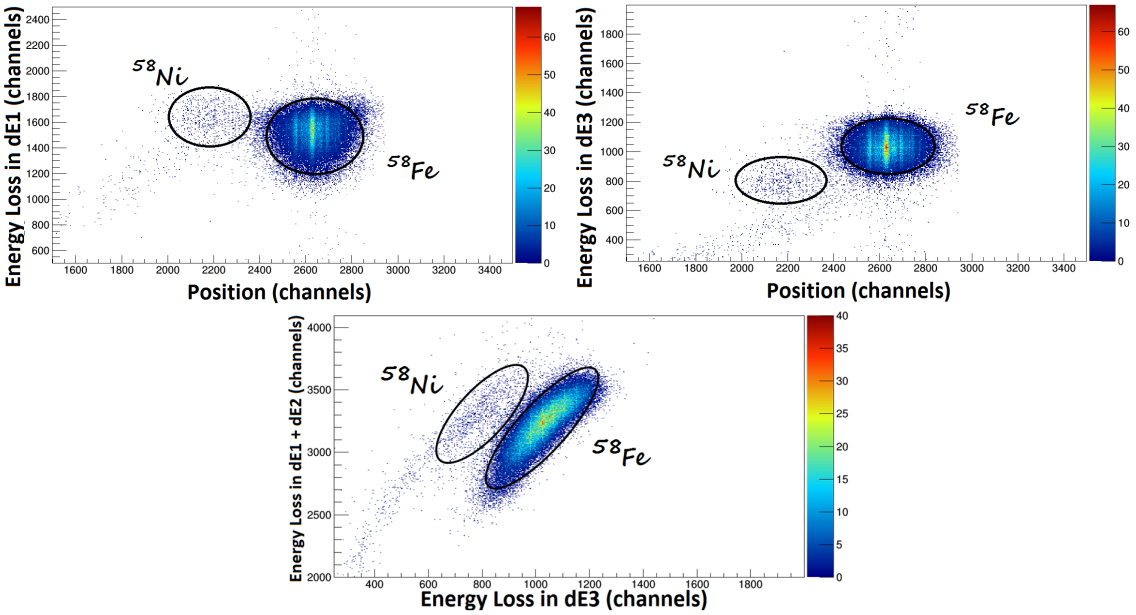

Figure 4.22. Example spectra showing the crossover technique. For the top two spectra, the y-axis is energy loss in channels and the x-axis is position in channels. The left spectra is the energy loss in anode 1 (dE1) and the right spectra is the energy loss in anode 3 (dE3). In dE1, nickel is losing energy faster than iron and in dE3, iron is losing faster than nickel. Note, that the gains for the preamplifiers are different between dE1 and dE3, so the energy loss is not to scale. The bottom spectrum is the energy loss in anode 1 and anode 2 (dE1 + dE2) versus the energy loss in anode 3 (dE3).

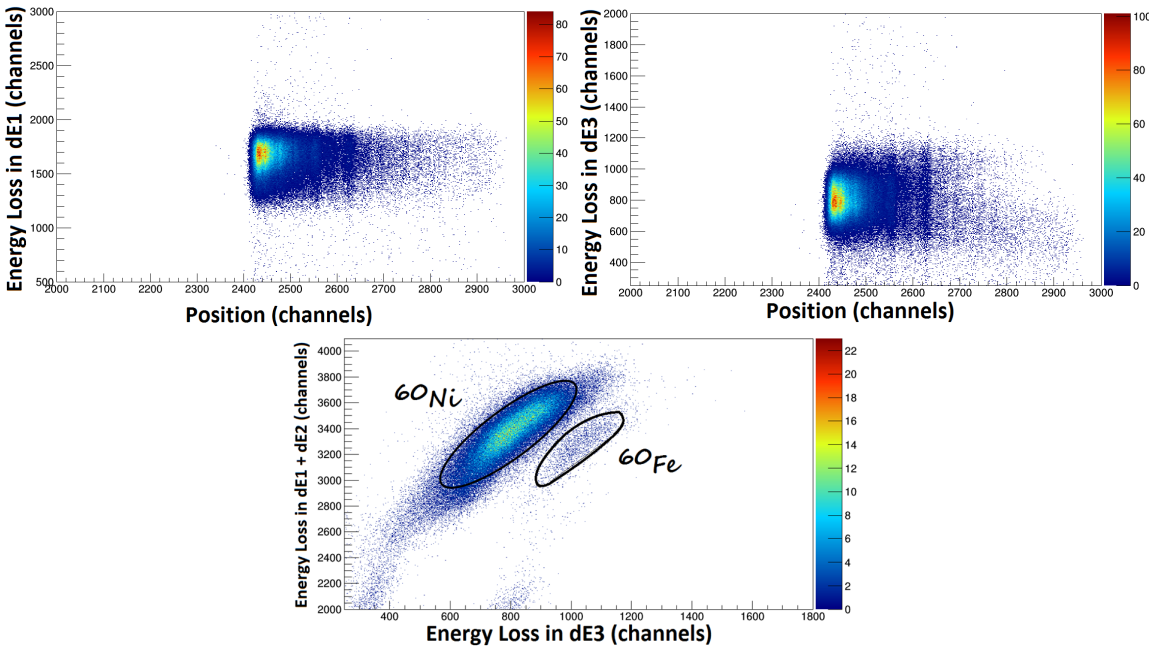

Figure 4.23. Example spectra for the Fe-4 sample. For the top two spectra, the y-axis is energy loss in channels and the x-axis is position in channels. The left spectra is the energy loss in anode 1 (dE1) and the right spectra is the energy loss in anode 3 (dE3). Bottom: Spectrum of the energy loss in dE1 plus dE2 (y) versus the energy loss in dE3 (x). The locations of the ^{60}Ni and the ^{60}Fe peaks are highlighted. The cuts used for the analysis are based off of runs on the Fe-1 sample due to the prevalence of the ^{60}Fe peaks.

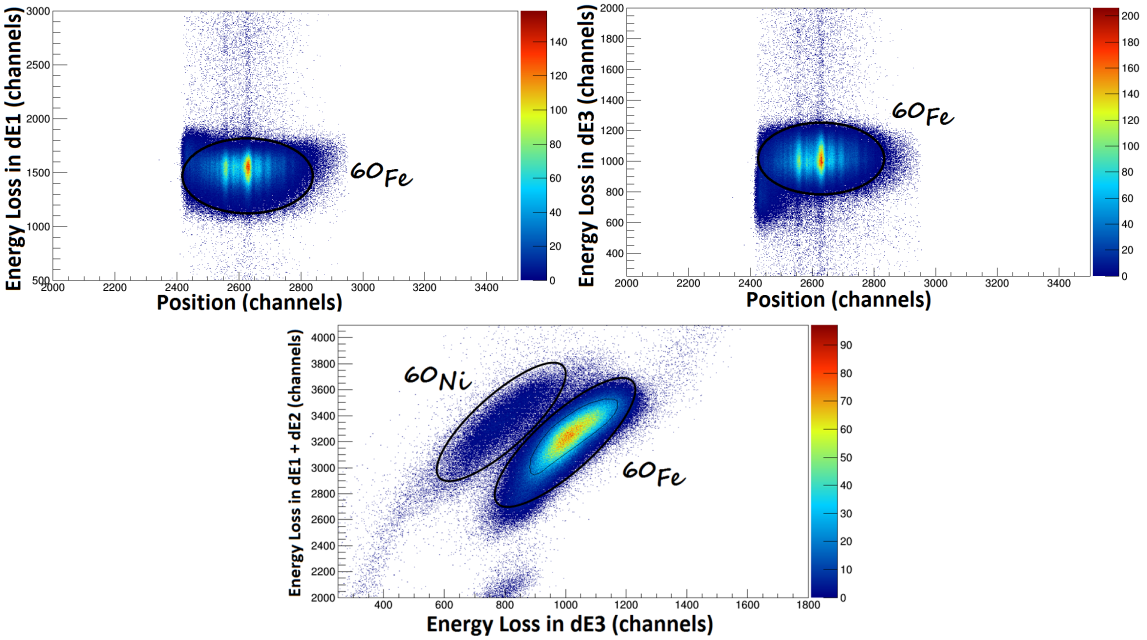

Figure 4.24. Example spectra for the Fe-1 sample, which contains the highest ^{60}Fe/^{56}Fe concentration of all of our samples. For the top two spectra, the y-axis is energy loss in channels and the x-axis is position in channels. The left spectra is the energy loss in anode 1 (dE1) and the right spectra is the energy loss in anode 3 (dE3). The location of ^{60}Fe is highlighted. Bottom: Spectrum of the energy loss in dE1 plus dE2 (y) versus the energy loss in dE3 (x). The locations of the ^{60}Ni and the ^{60}Fe peaks are highlighted. The cuts used for the analysis are based off of runs on the Fe-1 sample due to the prevalence of the ^{60}Fe peaks.

Raw data from the May 2016 experiment is given in Table 4.10 with further details given in Appendix C. The first round of Fe-4 and Fe-1 gives a scale factor of 16.652 ± 0.879, the second round gives a scale factor of 3.253 ± 0.153, and the final round gives a scale factor of 3.104 ± 0.162. The difference between the first round and the last two rounds comes from a change in the tune of the pilot beam. A small change in one of the focusing elements before the accelerator on the mass-60 beam resulted in a larger count rate at the detectors. This change was done for both the standard and the unknown material.

Only one round was completed on the blank material due to the significantly lower raw concentration of the blank material. With that same thought process, background subtraction is not needed on the standard or the unknown samples as the blank concentration is 3-4 orders of magnitude lower than the standard. Therefore, the average, scaled concentration for the unknown, Fe-1 sample is $(2.299 \pm 0.119) \times 10^{-6}$. With this result, the number of ^{60}Fe atoms in full Fe-1 sample is $(1.138 \pm 0.006) \times 10^{15}$. This second attempt is more reliable given the reduction in the percent error of the concentration measurement from 11.7% for the November 2015 experiment to 5.2% for the May 2016 experiment. The data from the May 2016 experiment will be used to calculate the half-life of ^{60}Fe along with the activity, which is described in detail in the following chapter.

TABLE 4.10

RAW DATA FROM THE EXPERIMENT IN MAY 2016

Sample [a]	Time (seconds)	Initial ^{56}Fe (nA)	Final ^{56}Fe (nA)	Average ^{56}Fe (pps)[b]	Average Transmission (%)	Total Counts	Raw Concentration (^{60}Fe/^{56}Fe)
Fe-4	2569.356	81.128	75.973	4.816×10^{11}	0.740	1156	1.262×10^{-10}
Fe-1	467.851	93.190	107.394	6.312×10^{11}	0.730	344633	1.599×10^{-7}
Background	1677.807	200.792	211.605	1.257×10^{12}	0.675	1	7.025×10^{-14}
Fe-4	1417.269	76.136	78.571	4.723×10^{11}	0.748	3226	6.443×10^{-10}
Fe-1	64.886	62.948	62.104	3.922×10^{11}	0.751	137621	7.205×10^{-7}
Fe-4	1456.651	25.907	24.786	1.610×10^{11}	0.778	1232	6.754×10^{-10}
Fe-1	425.498	56.552	58.504	3.592×10^{11}	0.801	746016	6.094×10^{-7}

[a]Each row represents the summation of six five minute runs. The raw concentration is calculated using Equation 4.6 and is unscaled. More detailed information for each run can be found in Appendix C.

[b]particles per second

CHAPTER 5

GAMMA RAY ACTIVITY MEASUREMENT

5.1 Decay Scheme for ^{60}Fe

As can be inferred from the decay scheme of ^{60}Fe in Figure 5.1 [10], there are two methods to measure the activity of a sample containing ^{60}Fe. The first method is by measuring the isomeric decay of the 2+ excited state in ^{60}Co. The second method is to measure the cascading gamma rays in the excited states of ^{60}Ni. The disadvantages of using the second method stems from the slow activity build-up of the excited states of ^{60}Ni due to the more-than-five-year half-life of the ground state ^{60}Co and the necessity of zero initial ^{60}Co in the sample. This, however, is not the case for the isomeric decay in ^{60}Co. All previous measurements of the half-life, not including the initial measurement in 1957, have measured the excited states in ^{60}Ni. This will be the first measurement of the isomeric state in ^{60}Co that is also coupled with the AMS technique as described in the previous chapter.

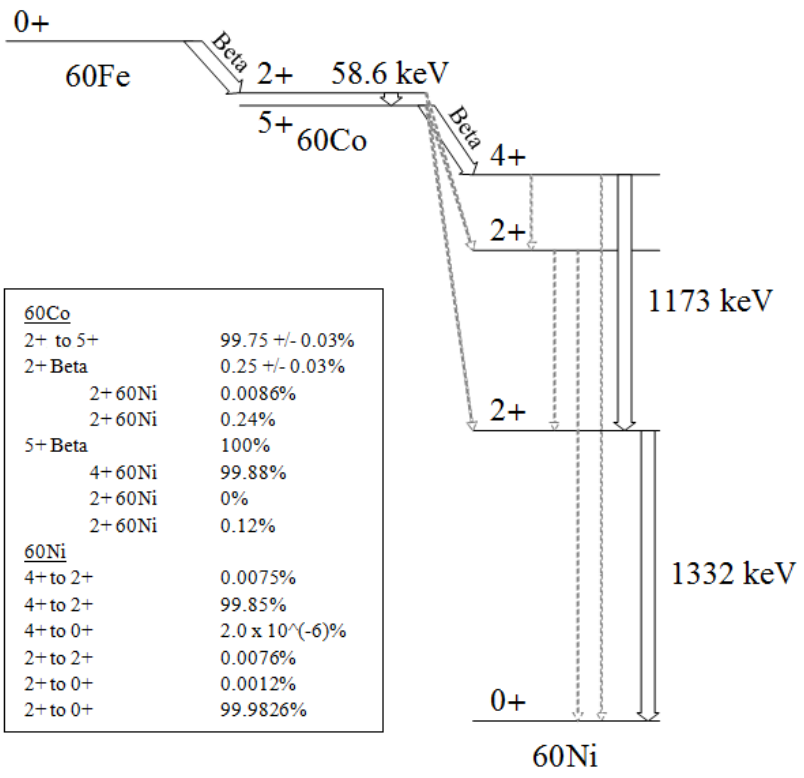

Figure 5.1. Decay Scheme of ^{60}Fe. Thick open lines indicate the most probable decays, both β decays and gamma ray decays. Dotted lines indicate other possible decays that occur with a branching ratio of less than 0.25% [10].

The 2+ state of ^{60}Co decays with a half life of 10.467 minutes [10] by internal conversion to the ground state of ^{60}Co (99.75 $\pm$ 0.03 %) or by β- decay to one of the excited states in ^{60}Ni (0.25 $\pm$ 0.03 %). Internal conversion decay by definition occurs one of two ways: either the excited nucleus will emit a γ ray or will transfer its excess energy to an inner shell atomic electron, thereby ejecting that electron from the atom. A higher shell atomic electron will transition down to fill the now empty

space, emitting a characteristic x-ray at the same time. Combining the probability of ejecting an electron, λ_e, and the probability of emitting a gamma ray, λ_γ gives the total decay probability, λ_{total}. The ratio between the two values is defined as the internal conversion coefficient, α, shown in Equation 5.1. In Equation 5.2, the total coefficient has been expressed as the sum of the partial coefficients for each atomic shell. For example, the probability that the electron that fills the vacancy is from the K shell is written as λ_K.

$$\alpha_{total} = (\lambda_e) / (\lambda_\gamma) \tag{5.1}$$

$$\alpha_{total} = (\lambda_K) / (\lambda_\gamma) + (\lambda_L) / (\lambda_\gamma) + (\lambda_M) / (\lambda_\gamma) + ... = \alpha_K + \alpha_L + \alpha_M + ... \tag{5.2}$$

The total decay probability can then be rewritten in terms of the internal conversion coefficients:

$$\lambda_{total} = \lambda_\gamma + \lambda_e = \lambda_\gamma \cdot (1 + \lambda_e/\lambda_\gamma)$$

$$\lambda_{total} = \lambda_\gamma \cdot (1 + \alpha_{total}) \tag{5.3}$$

$$\lambda_{total} = \lambda_\gamma \cdot (1 + \alpha_K + \alpha_L + \alpha_M + ...) \tag{5.4}$$

The value of α_K is 39.0 $\pm$ 1.9, experimental determined by [34], and the ratios of α_K/α_L and α_L/α_M are 5.78 $\pm$ 0.15 and 7.53 $\pm$ 0.18, as determined by [37]. This leads to an α_{total} of:

$$\begin{aligned}
\alpha_{\text{total}} &= \alpha_{\text{K}} + \alpha_{\text{L}} + \alpha_{\text{M}} \\
\alpha_{\text{total}} &= \alpha_{\text{K}} \cdot (1 + (\alpha_{\text{L}}/\alpha_{\text{K}}) + (\alpha_{\text{M}}/\alpha_{\text{L}})(\alpha_{\text{L}}/\alpha_{\text{K}}))
\end{aligned}$$

Therefore, α_{total} is 46.64 ± 1.91. Looking at Equation 5.3, we can find the percentage of decays that occur via a γ ray emission by dividing by λ_γ and inverting:

$$\begin{aligned}
\lambda_{\text{total}}/\lambda_\gamma &= 1 + \alpha_{\text{total}} \\
\lambda_\gamma/\lambda_{\text{total}} &= \frac{1}{47.64} = 2.10 \pm 0.08\%
\end{aligned}$$

This experimental result, as a check, is within error of the theoretical calculations of $(2.07 \pm 0.03)\%$ [10], which is the accepted value for this decay.

5.2 Experimental Setup

For measuring the activity of our ^{60}Fe sample, High Purity Germanium (HPGe) detectors are used. These types of detectors are used to measured γ rays and X-rays. Before discussing the detector itself, the following section briefly reviews how γ rays interact with material.

5.2.1 Gamma Ray Interactions

Nuclear reactions and some particle decay processes can leave the nucleus in an excited state. This excess energy can be released through the emission of γ rays. The energy range for γ rays is on the order of 0.1 - 10 MeV. These photons are similar to x rays and can overlap in energy ranges. γ rays come from nuclear transitions whereas

x-rays come from atomic transitions, or the energy released when atomic electrons change atomic levels.

Photons interact with material in the following four processes: Photoelectric Absorption, Compton Scattering, Pair Production, and Coherent Scattering. In Photoelectric Absorption, the γ ray interacts with the material and is absorbed. A photoelectron is ejected from a bound shell, typically the innermost K shell. The photoelectron will have an energy of the original γ ray minus the binding energy of the electron. For γ ray rays of less than 100 keV, the photoelectron carries off most of the original energy. The interaction also leaves behind a vacancy which is filled by a higher shell electron. An x-ray of the energy difference of the two shells is emitted in the process. This x ray is usually reabsorbed but it can migrate in the material and escape altogether. The photoelectric absorption process dominates for low energy x and γ rays and is enhanced with increasing proton number of the absorbing material.

A second process of interaction is Compton Scattering, where an incident γ ray will interact with an atomic electron and be deflected. Calculated in the rest frame of the electron, the γ ray has the energy of $h\nu$, where h is Planck's constant and ν is the wave frequency. Some of this energy is transferred to the electron and it recoils as well. The new energy of the photon is

$$h\nu' = \frac{h\nu}{1 + \frac{h\nu}{\mathrm{m_o c^2}} \cdot (1 - \cos(\theta))} \tag{5.5}$$

where θ is the angle of deflection for the γ ray and $\mathrm{m_o c^2}$ is the rest energy of the electron.

The third type of interaction, called Pair Production, is only for γ rays with energies above twice the rest mass of an electron ($\approx$1.02 MeV). In this process, the γ ray within the Coulomb field of a nucleus converts into an electron-positron pair. All

excess energy above 1.02 MeV goes into the kinetic energy of the e-/e+ pair. Both the e- and the e+ will eventually be absorbed back into the material, annihilating, and giving off a γ ray of 511 keV each. The probability of this process also depends on the material's proton number.

The last interaction for γ rays is Coherent (or Rayleigh) Scattering. Here the γ ray interacts with the electrons of the absorber but it doesn't excite or ionize the atom. The γ ray does not lose any energy.

In Figure 5.2, the dominating process for a given absorber proton number is shown as a function of the photon energy in MeV. In general, the photoelectric effect is dominant at lower energies and pair production at higher energies. The solid black lines show were the neighboring processes are equivalent.

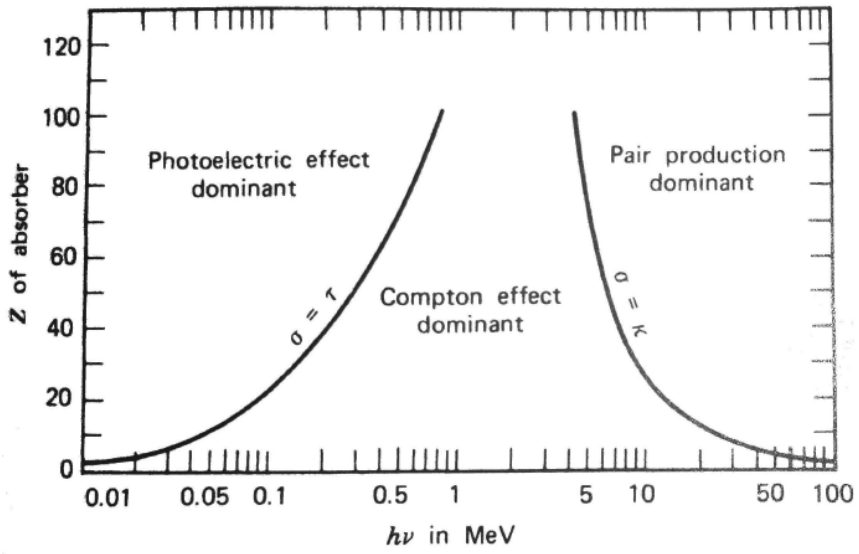

Figure 5.2. Relative Importance of the three major γ ray interactions, minus Coherent Scattering [24]. Solid lines indicate where the neighboring interactions are equivalent.

Each of the processes described above will remove a γ ray by absorption or scattering away except for Coherent Scattering. This attenuation of γ rays has a probability per path length of

$$\begin{aligned} \mu = & \quad \tau(\text{Photoelectric}) + \sigma(\text{Compton}) + \kappa(\text{Pair}) \\ = & \qquad \text{Linear Attenuation Coefficient} \end{aligned}$$

where τ, σ, and κ are the parameterization probabilities that a γ ray interacts and is removed via the Photoelectric Effect, Compton Scattering, and Pair Production respectively. Each of these probabilities will depend on the material the photon is passing through and the energy of the photon. The linear attenuation coefficient divided by the density of the absorber is called the mass attenuation coefficient.

In trying to measure the activity of our ^{60}Fe sample, we want to find the total rate at which the γ rays are emitted from the sample. Any material between the sample and the detector, such as the sample holder and the detector housing, can absorb these emitted γ rays. Absorption through materials and the solid angle between the sample and the detector crystal are factors in the overall detection efficiency. Two main types of detector efficiency are absolute full-energy peak efficiency and intrinsic efficiency. Absolute efficiency is defined as the ratio of counts in the full energy peak divided by the number of γ rays emitted from the source. Intrinsic efficiency is the ratio of the number of counts in the peak divided by the number of γ rays incident on the detector. Efficiencies quoted through the following are absolute unless otherwise noted.

5.2.2 High Purity Germanium Detectors

Semiconductor materials have been used as γ ray detectors as they provide several key advantages over scintillation detectors. These advantages are a compact size, relatively fast timing characteristics (charge carrier mobility is several times that of scintillation detectors), and an effective thickness that can be changed. However, semiconductor detectors are limited to a small size and are highly susceptible to radiation damage.

One type of semiconductor commonly used for γ ray detection is High Purity Germanium (HPGe). Semiconductor detectors are based on the properties that can be found at the junction of n-(donor) and p-(acceptor) type material. For n-type, the material is doped with an impurity such that the number of conduction electrons is much greater and the number of holes is much smaller than found in a pure sample. The opposite is true for p-types, where the impurity causes the number of holes to be much greater and the number of conduction electrons to be much smaller than in a pure material. The junction between the types of material is typically achieved by starting with a crystal of one type and changing the doping conditions from one side to the other side. For example, one can start with a p-type material and expose one side of it to an n-type vapor that will diffuse to a certain depth in the p-type material. Around this junction between p- and n-type material, conduction band electrons from the n-type will move across the junction to fill holes in the p-type material. Conversely, holes from the p-type material will move across to combine with electrons in the n-type material. This leads to a build up of negative charge on the p-side and positive charge on the n-side of the junction, with a steady state charge distribution across the junction itself. This region of charge imbalance is referred to as the depletion zone. This concept is shown in Figure 5.3.

With a higher level of purity (or low levels of doped impurities) added to the germanium crystal, the depletion region will be larger and the conductivity of the

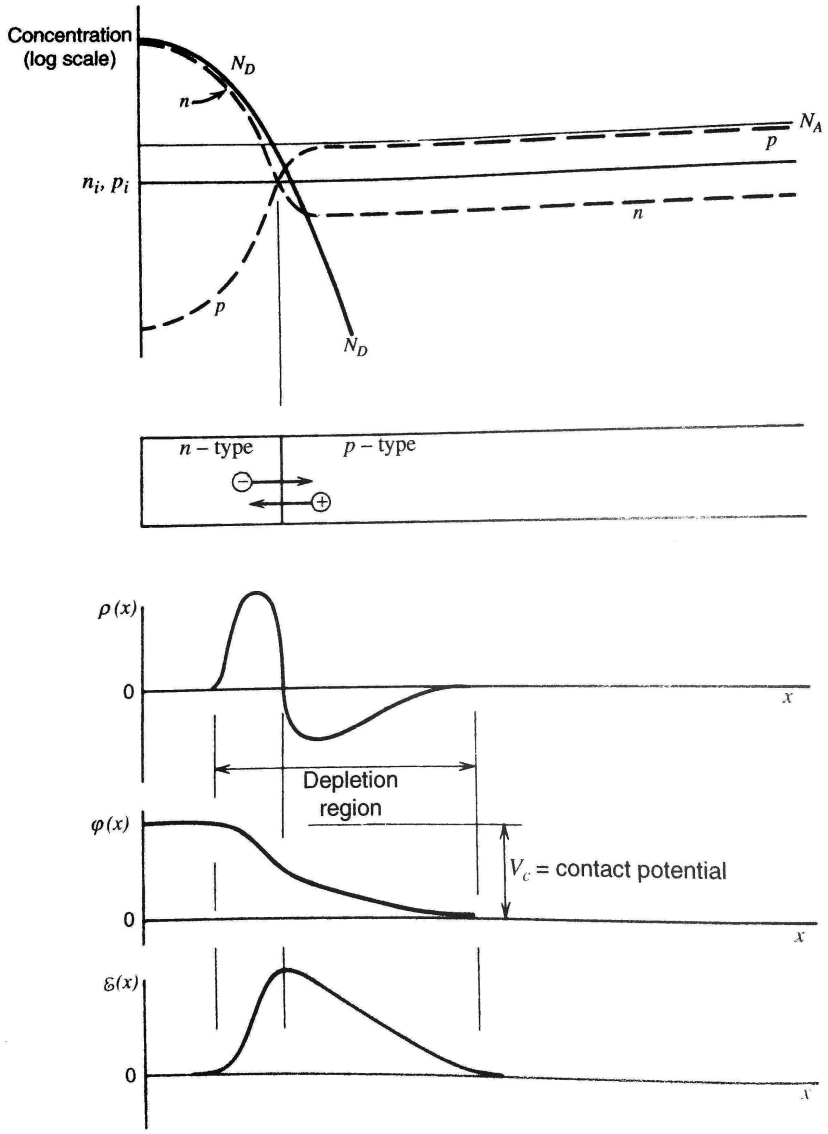

Figure 5.3. The effects of a junction between n-(donor) and p-(acceptor) types of semiconductor material. Top: the concentrations of the both types in a p-type semiconductor that has been exposed to a vapor of an n-type material. N_D is the resulting donor profile and N_A is the resulting acceptor profile. The variation of equilibrium charge carrier concentration is labeled as n and p for conduction electron and hole concentration respectively. n_i and p_i are for an intrinsic material, or one where the holes and conduction electrons are equal. Bottom: profiles for the space charge ρ(x), electric potential φ(x), and the electric field ε(x). The effects of the charge diffusion across the junction lead to these profiles [24].

material will be higher. The depletion region is where the γ ray will create charges by interactions with the material. Further biasing this region with applied voltages will increase the thickness of the depletion region, giving a larger section for the γ rays to interact in. HPGe detectors are operated as fully-depleted (the depletion region extends throughout the entire crystal) by applying a reverse bias voltage to the crystal. Further increasing the voltage applied creates a uniform electric field throughout the crystal. A small electric field is enough to affect the drift velocities of the created charge carriers, minimizing the collection time and reducing the negative effects of carrier recombination and trapping.

These detectors come in a variety of geometrical configurations, two of which are planar and coaxial. The planar configuration has the electrical connections on either side of a thin, flat crystal. The end cap of the detector is made with a thin beryllium foil, or "window," which allows low energy photons to pass through. This configuration provides a depletion region of only 1- 2 cm, making it the ideal configuration for low energy (3 keV to 300 keV) photons due to the mean free path of the γ ray. For energies up to several MeV, depletions regions of 5 cm are needed. To achieve this depth, the coaxial configuration is used. One electrical contact is on the outer surface of a cylinder. The other is on the inner surface where the core of the cylinder has been removed.

For the decay of the excited states in ^{60}Ni the coaxial configuration is used. These types of HPGe detectors are readily available in most laboratories. However, for the isomeric decay of ^{60}Co, the planar configuration is needed as the low energy γ ray produced would be stopped in the coaxial detector housing. The settings and physical dimensions for the two planar HPGe detectors used for the measurement are shown in Table 5.1. These detectors were borrowed from Argonne National Laboratory for use in this specific experiment.

TABLE 5.1

SPECIFICATIONS FOR BOTH HPGE PLANAR DETECTORS

	Detector 1	Detector 2
Model #	GLP-50XXX/15-S	GLP-50XXX/15-S
CFG	GG-GLP-S	GG-GLP-S
Serial	37-H185	38-H192
Bias Voltage	-1500V	-2000V
Active Crystal Diameter	51.0 mm	51.0 mm
Active Crystal Depth	14.3 mm	14.3 mm
Crystal Back Contact	0.7 mm	0.7 mm
Beryllium (Be) Window Thickness	0.5 mm	0.5 mm
Crystal Position from inside of Be window	11 mm	12 mm

5.2.3 Low Background Counting Station

In order to measure the activity of our sample, one needs to eliminate as much of the background radiation as possible. This is typically done by surrounding the chosen detector(s) with lead bricks. The lead bricks, with their high proton number, are able to stop or attenuate background radiation from the room and from cosmic rays. This is illustrated in Chapter 2, Figure 2.6. A diagram of the the lead castle setup used is shown in Figure 5.4. Some bricks are not visible here, in order to show the inside of the castle. The dark blue bricks are the two base layers of the castle. The green bricks are the walls of the castle, two layers deep. Eight bricks, four per detector, have a half circle cut made in their sides to closely surround the

detector stem. The dark- and light-gray bricks are the top two layers, supported by an aluminum sheet (not shown). The light-gray bricks in particular are connected together and can be lifted up using a custom winch system. This allows for easy access to the inside of the castle and eliminates any line-of-sight issues from above. Two layers of bricks are used on all sides to help eliminate line of sight issues and also because any extra layers would only add to the background due to a buildup of tertiary cosmic-ray particles [29] or from the intrinsic background from the added bricks themselves. Therefore, the only line-of-sight issues are from the bricks around the detector stems.

5.2.3.1 Selection of Lead Brick

Considerable effort was expended in order to select bricks from the NSL with the lowest intrinsic activity and the squarest edges. In the following paragraphs, several intrinsic background lines for lead bricks are discussed briefly. The activity of the background radiation was a factor in deciding which bricks were used for the final castle as shown in Figure 5.4.

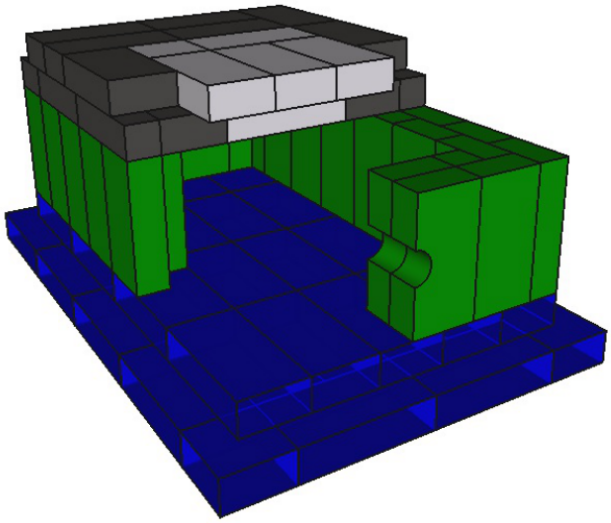

Figure 5.4. Lead Castle Construction with Interior View. The dark blue bricks are the bottom two layers. The green bricks are the side layers. The bricks surround the detector stems had half circles cut out in order to surround the detector stems fully. The dark- and light-gray bricks are the top two layers, supported in place by an aluminum sheet (not shown). The light-gray bricks are connected together for easy access to the inside.

Natural impurities found in lead ore include the products from decay chains of ^{238}U and ^{232}Th. In particular, impurities such as the radioactive ^{210}Pb from the ^{238}U decay chain can not be removed from the lead by further chemical processing. The decays from either of the ^{238}U or the ^{232}Th chains should be considered when choosing lead bricks to use for low background counting stations [35]. One such decay that was looked at for each brick was the decay of ^{226}Ra at 186.211 keV from the ^{238}U decay chain.

Another possible background contaminant is ^{137}Cs, which was produced during the testing of nuclear bombs. It has a half-life of 30.08 years [11], so as a result of bomb testing in the atmosphere, this radioactive isotope is found in water and dirt.

Though not on levels to be harmful to the human population, ^{137}Cs can be seen by, and can affect, low background counting stations. Lead bricks that were selected for the final castle were cleaned with water and soap and then air dried to remove any surface dust which may contain ^{137}Cs. The bricks were then wrapped in brown paper, in order to keep the bricks clean from further contamination. Should contamination occur, the paper can be replaced which is easier and safer than cleaning the bricks again.

We also looked at the count rate in the region of interest between 48 keV and 68 keV for each brick. There is one specific background line in this region at 63.29 keV from the decay of ^{234}Th in the ^{238}U decay chain. This peak is well separated from our peak of interest.

Bricks with contamination levels well above the average for the bricks tested were not considered for the castle. Bricks with the lowest activity were used as the inner layers.

5.2.3.2 Efficiency Measurements

The efficiency for each detector must be known well as it is used to determine the total count rate emitted by a sample. The isotope ^{241}Am was used to determine the detectors' efficiency as it decays by α emission to an excited state in ^{237}Np which then contains a prominent γ ray emission line at 59.54 keV [5]. Since this line is within 1.5 times the full width half maximum of our planar detectors to our gamma ray of interest at 58.6 keV, it makes for an appropriate detector efficiency calibration. A 100 nCi ^{241}Am + Hydrochloric (HCl) acid liquid source was obtained from the isotope products company, Eckert and Ziegler. 6.5 mg of stable Fe_2O_3 was added in solution to match the amount of stable iron in the Fe-1 sample. The HCl acid was then evaporated out of the solution as done with the Fe-1 sample. The remaining 0.05 mL was then pipetted onto a thin piece of Mylar (0.002 inches thick, 1.25 inches by 1.25

inches square) and allowed to fully dry. This process followed the same procedure as the Fe-1 sample evaporation and details of that are discussed above in Chapter 3. This point source of ^{241}Am was used to determine the efficiency of the planar detectors and eliminate any geometry effects between the efficiency source and the sample.

5.3 Background Considerations

Despite the careful construction of the lead castle to surround the detectors, the detectors still register background. Part of the background comes from the room and the castle itself, but some background is sample-induced. As beta decay is the main decay mechanism for ^{60}Fe and the ground state of ^{60}Co, there are numerous fast electrons being emitted from the sample. These beta particles will have energies from 0 keV up to the end-point energy, which is 178 keV for ^{60}Fe, and 317.88 keV and 1492 keV for the ground state of ^{60}Co [10]. Some beta particles will have enough energy to reach the detector crystal itself, but more likely the beta particles will interact with the source, the detector, and the shielding materials of the castle. These interactions create bremsstrahlung photons that will increase the background continuum in the spectra as shown in Figure 5.5. The best way to eliminate some of this is to add a beta absorber between the source and detectors [18]. We used a 0.25 cm thick piece of transparent plastic, or acrylic glass, on either side of the source. The effect of the acrylic glass is shown in Figure 5.6 and is very pronounced for low energy γ rays. The acrylic glass will have a minimum effect on the amount of γ rays from either the sample or the ^{241}Am efficiency source that reach the detector but will serve to eliminate some of the background in our region of interest, see Figure 5.7.

The mass attenuation coefficient for a gamma ray of 60 keV is 0.1924 cm^2/g [20] and the density of acrylic glass, or polymethyl methacrylate, 1.18 g/cm^3. Plugging these values and a acrylic glass thickness of 0.25 cm into the following equation for the

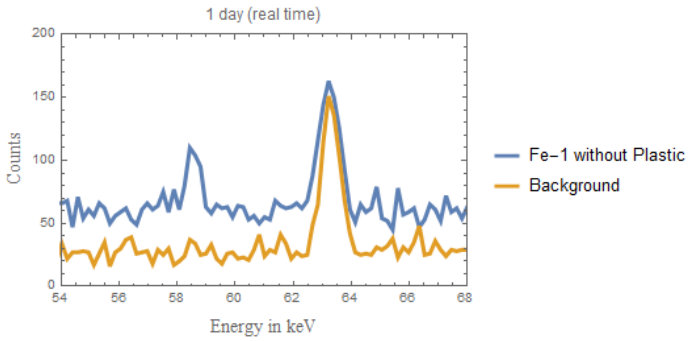

Figure 5.5. 1 day runs on the Fe-1 ^{60}Fe sample and the background. Counts per bin are on the y-axis and energy in keV is on the x-axis. For the sample data, the background continuum is shifted slightly upward. The background subtraction technique described later in this section, accounts for this shift.

attenuation of gamma rays through material, shows that almost 95% of the gamma rays will be transmitted through the acrylic glass. The extra 5% that is attenuated either from the efficiency source or the sample is accounted for with the efficiency sample, provided that the acrylic glass is used for both.

$$\begin{aligned} I &= I_o \exp^{-\mu/\rho \cdot \rho l} \\ I/I_o &= 0.9448 \rightarrow 94.48\% \end{aligned}$$

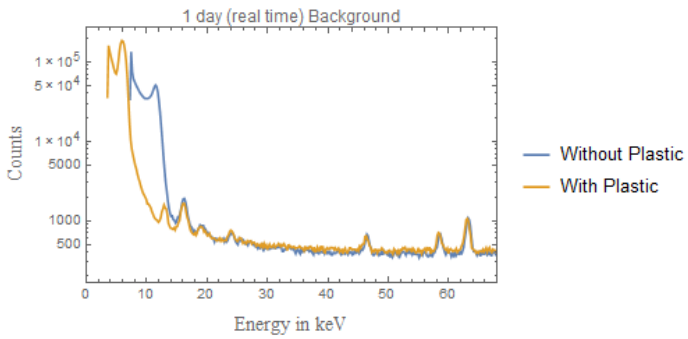

Figure 5.6. Full spectra of Fe-1 sample, with and without plastic for a beta absorber. Measurements were taken for one day each. Counts per bin are on the y-axis and the energy in keV is on the x-axis. Note the reduction specifically in the lower energy gamma rays and X rays (below 20 keV).

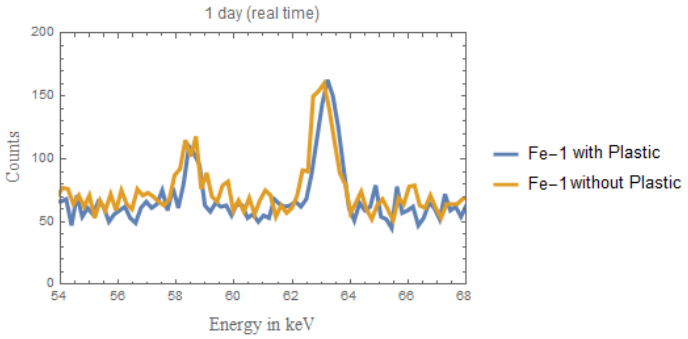

Figure 5.7. Zoomed in on the region of interest for the Fe-1 sample, with and without the plastic beta absorber. Counts per bin are on the y-axis and energy in keV is on the x-axis. The measurement of each was taken over one day. The difference between the two spectra is subtle however the spectra without the plastic (orange) has slightly higher counts per bin on either side of the peak of interest at 58 keV than the spectra with the plastic (blue).

Any technique used to subtract out the background from the real peak must account both for the room background and this shift due to the beta particle emission. The technique is illustrated in Figure 5.8 and was used for both the sample and the ^{241}Am efficiency source. For this method, measurements on the sample also serves as the background subtraction. Averages of counts per bin are taken on either side of the peak of interest. Any counts below a straight line between these averages on the left and right side are subtracted from the peak's total. As a check, we can apply this technique to the background line at 63 keV. This peak, as a reminder, is from the ^{238}U decay chain and is found in lead bricks themselves. As such, this peak should remain effectively constant with and without the sample. This was checked for a 24 hour run and the activity of this uranium peak was found to be, with background subtraction, $(7.80 \pm 0.47) \times 10^{-3}$ Bq and $(8.29 \pm 0.33) \times 10^{-3}$ Bq for the background run and the sample run, respectively. These are consistent with each other.

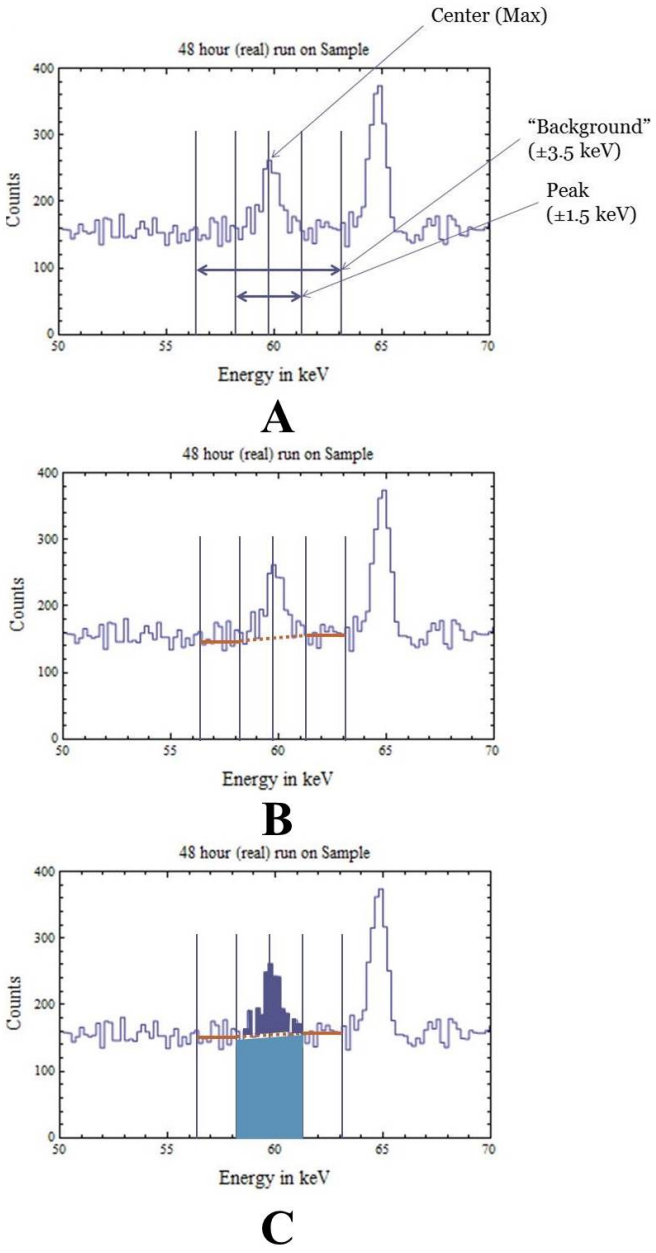

Figure 5.8. Continuum Subtraction Example on 48 hour measurement on the Fe-1 Sample shown as counts (y) as a function of energy in keV (x). Each panel contains the same data. The progression of the panels illustrates the subtraction technique. In A, the max of the peak is defined as the centroid. The full peak is ±1.5 keV from the max. The background continuum is defined from ± 1.5 keV to ± 3.0 keV from the max. In B, the average counts per channel on the left and the right is found (solid line) and a line is defined between the two averages (dashed line). In C, the area below the line connecting the two averages is subtracted out from the total area in the full peak. This, then, gives the corrected counts in the peak.

5.4 Measurement Method and Analysis

In the following sections, the measurement and analysis techniques are discussed and the final count rate for the Fe-1 sample is given.

5.4.1 Measurement Method

For each measurement of the sample, a cycle was followed. The efficiency of the detectors were measured for 3600 live seconds using the ^{241}Am point source. Then a background measurement was taken with no sample. This measurement was taken for 24 hours real time and used to ensure there were no major changes in the room background. Lastly, the Fe-1 sample was measured for a total of six days. This cycle was repeated for a total of ten times. For the samples, the corrected counts (background subtracted) are scaled for the internal conversion, the isomeric decay, and the detector efficiency percentages.

$$\begin{aligned} \text{Counts}_{\text{total}} &= \text{Counts}_{\text{corrected}} \left(\frac{100}{\text{Internal Conversion \%}} \right) \left(\frac{100}{\text{Isomeric Decay \%}} \right) \times \\ &\quad \times \left(\frac{100}{\text{Detector Efficiency \%}} \right) \\ &= \text{Counts}_{\text{corrected}} \left(\frac{100}{2.07\%} \right) \left(\frac{100}{99.75\%} \right) \left(\frac{100}{\text{Detector Eff. \%}} \right) \end{aligned}$$

5.4.2 Example Spectra and Results

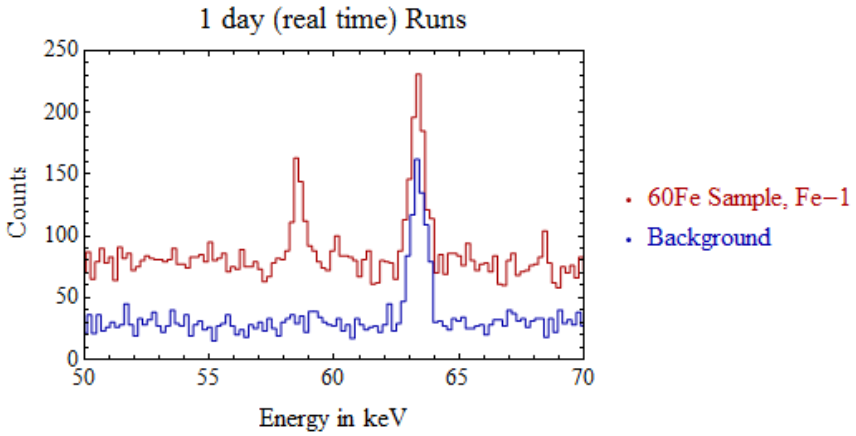

Figure 5.9. 24-hour runs on the Fe-1 sample (in red) and the background (in blue). Counts per bin are on the y-axis and energy in keV is on the x-axis. Note the background peak at 63 keV. This peak is from the decay of ^{234}Th in the ^{238}U decay chain. This peak is well separated from our peak of interest but can act as a good test of the background subtraction technique.

Figure 5.9 shows example spectra from the Fe-1 sample (24 hours real time) and a background (24 hours real time). The y-axis is counts per bin and the x-axis is energy of the γ ray in keV. The background measurement is shown in blue and the measurement on the Fe-1 sample is shown in red. A total of ten six-day measurements were completed on the Fe-1 sample for each detector. Accounting for any dead time, which was minimal, these measurements equate to more than 118 days and more than 34600 counts (background subtracted) seen by the detectors. Each six-day run was totaled up and corrected, as discussed above, for the detector efficiency and the branching ratios. Following the corrections to the measured counts, the corrected

counts and the measurement times were summed, respectively, and the count rate for the Fe-1 sample is 1.2732 Becquerel (Bq), or counts per second. Knowing that the detector system and the sources were stable over time, the main contributors to the error on the measurement are in the detector efficiency (3.0%), the internal conversion coefficient (1.45%), and the branching ratio of the isomeric decay (0.03%). This leads to a total error on the activity measurement of 3.33%. Contributions from the statistics, for both the ^{241}Am and the Fe-1 sources, are negligible. Finally, remembering that this part of Fe-1 sample is 13.0016 g of an original 100 g solution with an error of 0.0001 g (also negligible), then the count rate for the full Fe-1 sample is 9.7926 ± 0.3261 Bq.

CHAPTER 6

CONCLUSION

Because ^{60}Fe is so long lived, its decay can be considered essentially constant. Therefore the decay constant for ^{60}Fe, λ_1, is much less than the decay constant for ^{60}Co, λ_2. The activity, A_2 for ^{60m}Co can then be simplified from Equation 6.1 to Equation 6.2. The activity of ^{60m}Co approaches the limiting value of Equation 6.2 as it comes into secular equilibrium, or when the production rate equals the decay rate.

$$A_2(t) \equiv \lambda_2 N_2(t) = N_o \frac{\lambda_2 \lambda_1}{\lambda_2 - \lambda_1}(\exp^{-\lambda_1 t} - \exp^{-\lambda_2 t}) \quad (6.1)$$

$$A_2(t) \simeq N_o \lambda_1 (1 - \exp^{-\lambda_2 t})$$

$$\simeq N_o \lambda_1 \quad (6.2)$$

$$t_{1/2} = N_o \frac{\ln 2}{A_2} \quad (6.3)$$

where λ_1 is the decay constant for ^{60}Fe, λ_2 is the decay constant for ^{60}Co, N_o is the number of ^{60}Fe atoms in the sample, N_2 is the number of ^{60}Co atoms in the sample from the decay of ^{60}Fe, and A_2 is the activity in counts per second of the ^{60}Co isomeric decay.

Therefore, the final result of our activity measurement, A_2, is (9.7926$\pm$0.3261) Bq. For N_o, we must convert our ^{60}Fe/^{56}Fe concentration into ^{60}Fe atoms by multiplying the concentration by the amount of ^{56}Fe added to the Fe-1 sample at its creation. Therefore, following Equation 6.3, the half-life of ^{60}Fe is

$$
\begin{aligned}
t_{1/2} &= \frac{\ln 2}{A} N_o = \frac{\ln 2}{A} (\text{Concentration} \times \text{Added } {}^{56}\text{Fe}) \\
t_{1/2} &= \frac{\ln 2}{9.7926 \text{ Bq}} \times (2.299 \times 10^{-6}) \times (4.95 \times 10^{20}) \\
t_{1/2} &= 8.055 \times 10^{13} \text{ seconds} = 2.55 \times 10^{6} \text{ years}
\end{aligned}
$$

The error in this measurement includes previously stated errors on the weighed samples (added ^{56}Fe and the weight of the Fe-1 sample used for the activity measurement) and the listed errors for the activity (3.33% error) and AMS measurements (5.18% error). The overall resulting error is 0.15×10^6 years, or 5.88%. The percent errors are given in Table 6.1 with the main contributors to the activity and AMS errors.

Our work agrees within error of the two recent measurement (Rugel, et al. [40] and Wallner, et al. [47]) and does not agree with the previously accepted value from Kutschera, et al. [28]. This is illustrated in the following figure, Figure 6.1.

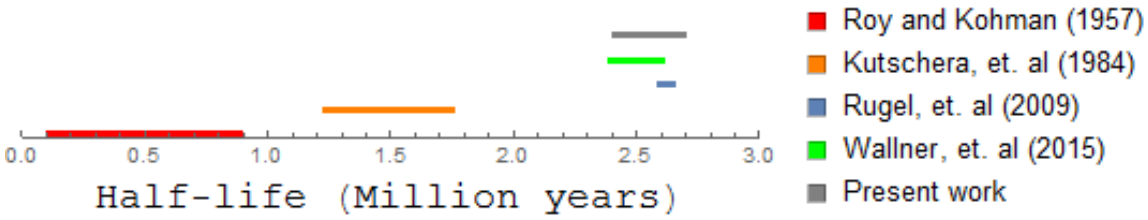

Figure 6.1. The previous four ^{60}Fe half-life measurements, including this work in grey. Our work overlaps with Rugel, et al. in blue with a half-life of (2.62 ± 0.04) million years and with Wallner, et al. in green with a half-live of (2.50 ± 0.12) million years. Our work also does not agree with the previously accepted value from Kutschera, et al. in orange of (1.49 ± 0.27) million years.

TABLE 6.1

QUANTITIES AND PERCENT ERRORS FOR THE ACTIVITY AND AMS MEASUREMENTS

	Quantity [a]	Amount	Percent Error (%) [b]
Activity Measurement	**Activity of Fe-1 sample** [c]	1.2732 Bq	3.33
	Branching Ratio	99.75 %	0.030
	Internal Conversion	2.07 %	1.45
	Detector Efficiency	x	3.00
	Fraction of the Original Fe-1 Sample	13.0016 mL/100 mL	7.69×10^{-4}
AMS Measurement	**AMS Isotope Ratio** [d]	2.299×10^{-6} ^{60}Fe/^{56}Fe	5.18
	Wallner, et al. Fe-4 Isotope Ratio	2.095×10^{-9} ^{60}Fe/^{56}Fe	4.25
	Faraday Cup Readings	x	1.0
	Stable Fe added to Fe-1 Sample	4.95×10^{20} ^{56}Fe atoms	0.20

[a]Bolded quantities are the final totals.

[b]Other contributors to the error, such as statistics, are negligible comparatively.

[c]Errors on the Branching Ratio, the Internal Conversion, and the Detector Efficiency are folded into Activity error.

[d]Errors on the reference material, the Faraday Cup readings, and the Stable Fe added are folded into the AMS error.

Because ^{60}Fe is only naturally produced in stellar environments, the observation of and the half-life for ^{60}Fe can have an impact on nuclear astrophysics related questions. For example, these include the timing of early Solar System events, the distance to or the amount of ^{60}Fe produced in a nearby supernova, and the brightness of ^{60}Fe

γ ray sources in our Galaxy. This work was the first time that the technique of accelerator mass spectrometry was paired with the isomeric decay of ^{60m}Co. With the development of a ^{60}Fe beam and a low level background counting station at the University of Notre Dame, we combined the results of the two experiments, thereby confirming a substantially longer half-life than previously accepted.

Pumbaa, with you, everything's gas. - Timon

APPENDIX A

ELECTRONICS

A.1 Signals from LL, LR, RL, and RR

Referring to Figure A.1, the position signals from the Parallel Grid Avalanche Counter (PGAC), referred to as LL, LR, RL, and RR pass through an Inverter before going to a Timing Filter Amplifier (TFA) where the signal is amplified and shaped. After the TFA, the signal goes to a Constant Fraction Discriminator (CFD) which creates a precisely timed logic pulse for the input signal. From here the signal goes through a Level Translator which has ECL logic outputs that go to a Time to Digital Converter (TDC). The TDC recognizes events and makes a digital representation of when it occurred, or the time interval between events. The gate of the TDC acts as the start signal and comes from an OR gate of the signals from the Left Anode, the Right Anode, and the Silicon Detector. The input signals are the stop signal for each channel.

A.2 Signals from the Left and Right Anodes

The signals from the Left Anode and the Right Anode go through an Inverter and a CFD, similar to the position signals from the PGAC. Following this the Left and Right Anodes along with the position signals to go another Level Translator. The ECL outputs from the level translator are sent to a latching scaler, which has independent counting channels so that the information can be read out to the computer without disrupting the data taking.

A.3 Gate and Delay Generator

Signals from the Left Anode and the Right Anode and the Silicon Detector go to an OR gate. One output of the OR gate is the real time for the level translator. As shown in Figure A.2, the other two outputs go to a Quad Four Fold Logic, which acts as a Fan-in/Fan-out with a veto. Three of the outputs from the Quad Four Fold Logic go to a Quad Gate and Delay Generator. One output is the TDC common start signal and one goes to the level translator as the the live time. In the Quad Gate and Delay Generator, the trigger from the second section starts a veto gate. This gate is stopped by the I/O Register from the computer, saying that it is done with the data. The gate will veto any other signals received at the Quad 4-Fold during that time. The Trigger from the third section of the Quad Gate and Delay Generator is delayed by 10 microseconds and then becomes the Trigger for the first section. The first section's Trigger starts a gate, telling the I/O Register to start taking data. This gate is stopped by the I/O, saying it is done. The Trigger from the fourth section starts a timed 10 microsecond gate which goes to the ADC which handles the energy signals from the Ionization Chamber (IC). This Trigger will already have had the vetoed signals taken out. At the ADC, this 10 microsecond gate is the same gate for the ADC.

A.4 Pile Up Rejection (PUR)

The Pile Up Rejection (PUR) signals from the Spectroscopy Amplifiers for the four sections of the IC are feed into an OR Gate as shown in Figure A.3. The OR Gate output is the start signal for a timed (48 microsecond) NIM Pulse/Gate. If this NIM pulse occurs at the same time as the gate for the energy signals, then it starts a latch Gate. The end of the latch gate, the Ship Out is reset from the I/O Register. This information is sent to another I/O Registers and the event is flagged as "PUR."

The event is not removed from the data, only flagged and can be taken out in the software later.

Figure A.1: Position Signals and Scalers schematic for the Accelerator Mass Spectrometry (AMS) electronics set up. Shown here are the position signals and the PGAC anode signals used for online scalers and timing. Figure courtesy William Bauder.

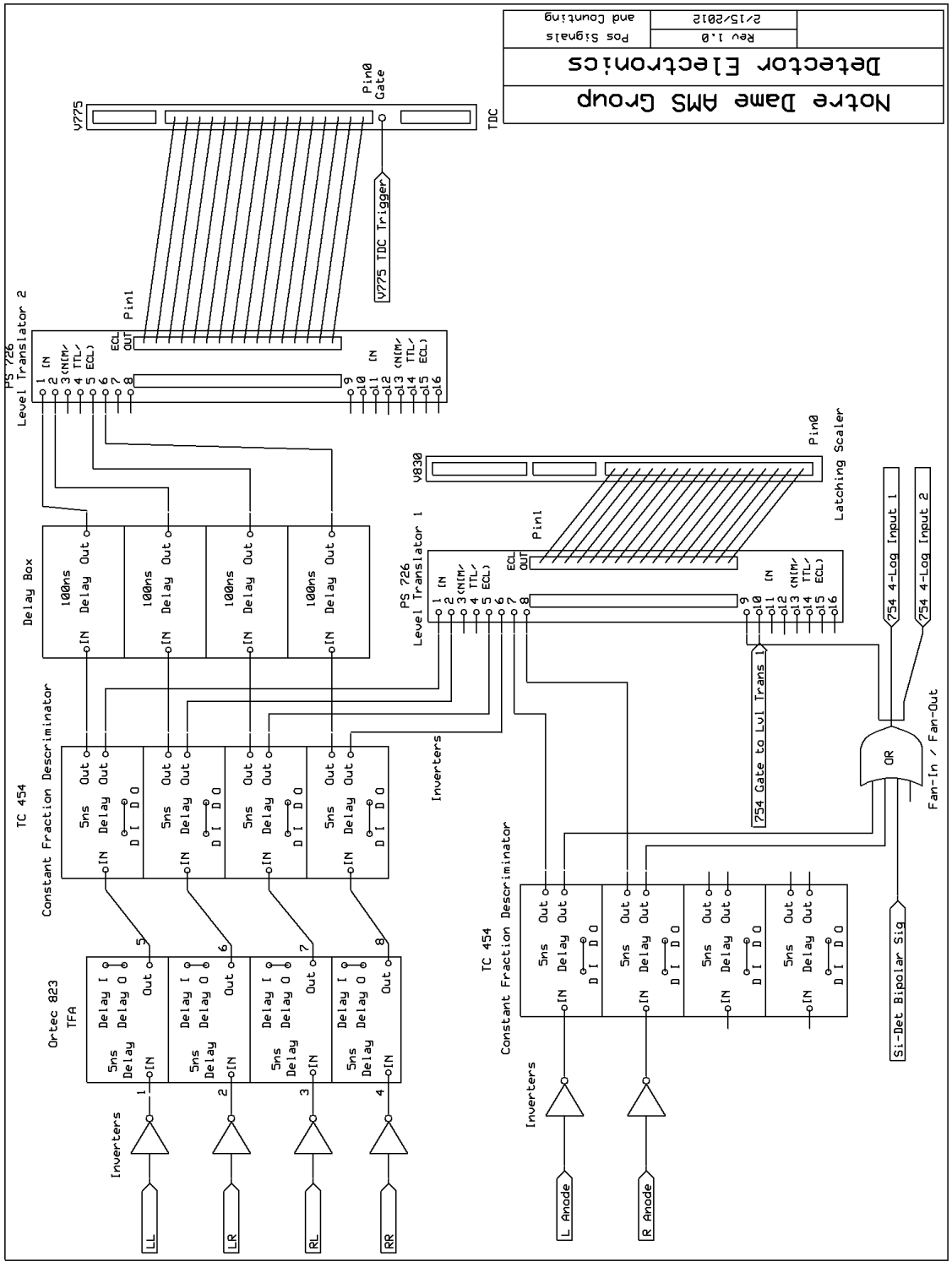
Notre Dame AMS Group
Detector Electronics
Rev 1.0
2/15/2012
Pos Signals and Counting
V775
TDC
Pin0
Gate
V775 TDC Trigger
Pin1
PS 726
Level Translator 2
ECL
OUT
1 IN
2
3 (NIM/
4 TTL/
5 ECL)
6
7
8
9
10
11 IN
12
13 (NIM/
14 TTL/
15 ECL)
16
Delay Box
100ns
Delay
Out
IN
V830
Latching Scaler
PS 726
Level Translator 1
754 4-Log Input 1
754 4-Log Input 2
754 Gate to Lvl Trans 1
OR
Fan-In / Fan-Out
TC 454
Constant Fraction Descriminator
5ns
Delay
D I D O
Inverters
Ortec 823
TFA
Delay I
Delay O
Out
5ns
Delay
IN
LL
LR
RL
RR
L Anode
R Anode
Si-Det Bipolar Sig

Figure A.2: Gating and Energy Signals for the AMS electronics set up. Shown here are the gates based on the position and Silicon detector signals. Also shown are the energy signals from the Ionization Chamber. Figure courtesy William Bauder.

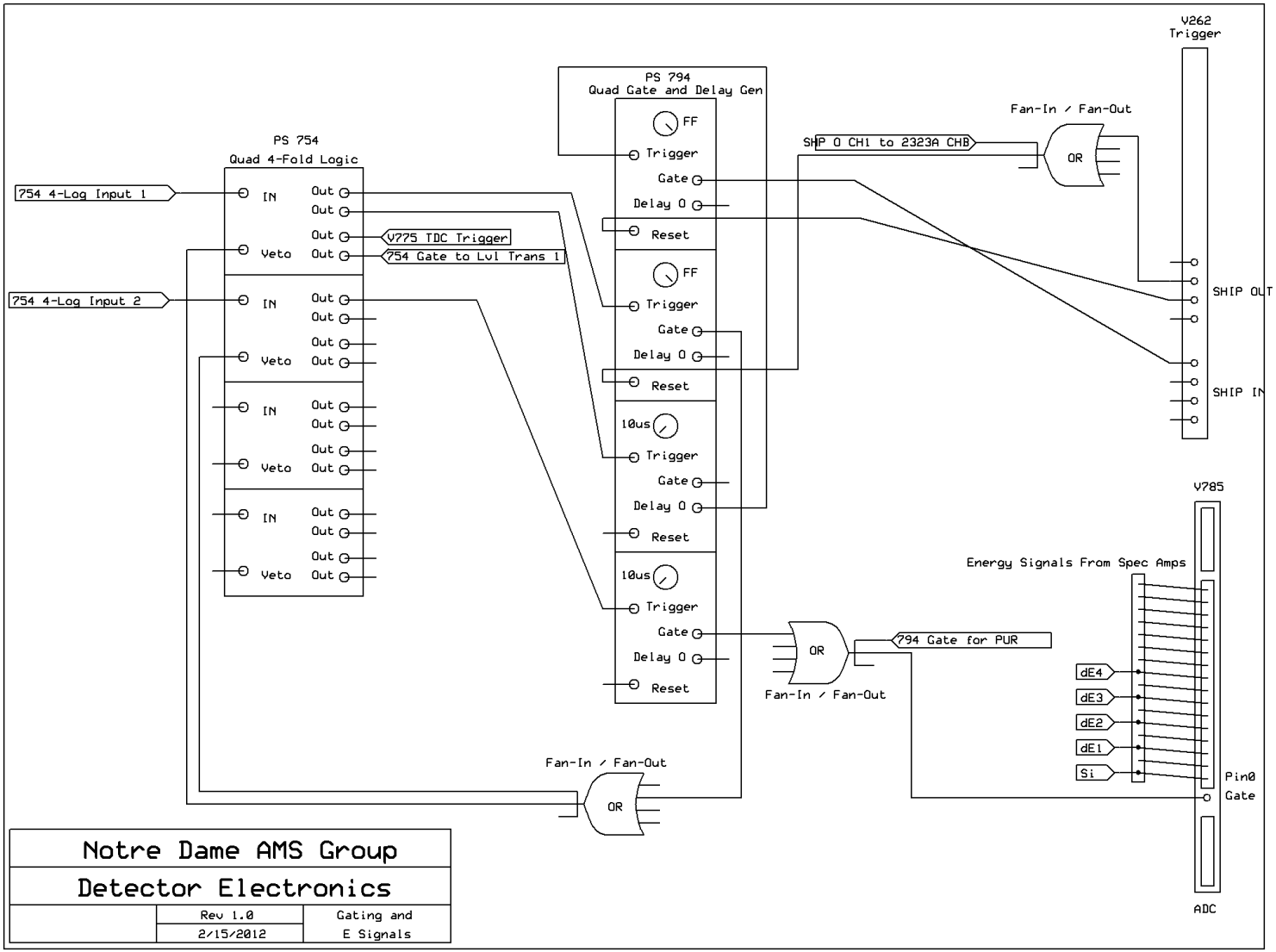
V262
Trigger
PS 794
Quad Gate and Delay Gen
Fan-In / Fan-Out
SHP 0 CH1 to 2323A CHB
OR
PS 754
Quad 4-Fold Logic
754 4-Log Input 1
754 4-Log Input 2
IN
Out
Veto
V775 TDC Trigger
754 Gate to Lvl Trans 1
FF
Trigger
Gate
Delay 0
Reset
10us
SHIP OUT
SHIP IN
V785
Energy Signals From Spec Amps
794 Gate for PUR
Fan-In / Fan-Out
dE4
dE3
dE2
dE1
Si
Pin0
Gate
ADC
Notre Dame AMS Group
Detector Electronics
Rev 1.0
2/15/2012
Gating and
E Signals

Figure A.3: Pile Up Rejection schematic for the AMS electronics set up. Figure courtesy William Bauder.

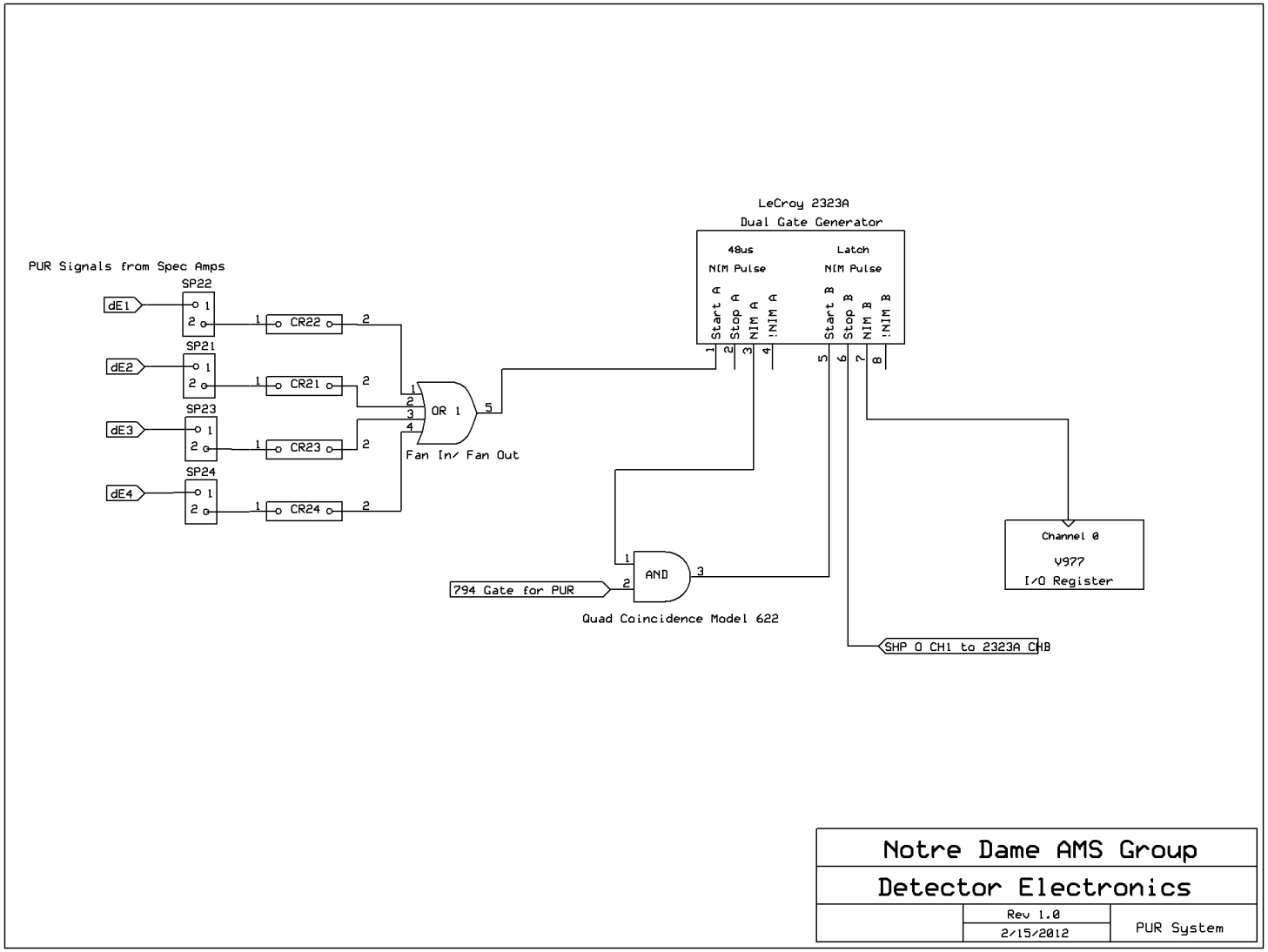
PUR Signals from Spec Amps
SP22
SP21
SP23
SP24
dE1
dE2
dE3
dE4
CR22
CR21
CR23
CR24
OR 1
Fan In/ Fan Out
LeCroy 2323A
Dual Gate Generator
48us
NIM Pulse
Latch
NIM Pulse
Start A
Stop A
NIM A
!NIM A
Start B
Stop B
NIM B
!NIM B
AND
794 Gate for PUR
Quad Coincidence Model 622
Channel 0
V977
I/O Register
SHP 0 CH1 to 2323A CHB
Notre Dame AMS Group
Detector Electronics
Rev 1.0
2/15/2012
PUR System

APPENDIX B

CHEMISTRY AND TIMELINE FOR MSU PRODUCED ^{60}Fe SAMPLE

The following pages include a timeline of events after the production of the MSU ^{60}Fe sample and the chemistry correspondence that was written.

Sample Timeline

Jan. 2-Feb. 1, 2009:	Implantation of ^{60}Fe in Al holder (1-3) (also short implantation in the same conditions).	
Feb. 1, 2009:	Implantation of ^{60}Co and ^{59}Fe in Al holder (3-3).	
Feb. 10, 2009:	Sample activity measurement at MSU prior to shipping.	
Feb. 11, 2009:	Begin of data analysis setup at ND.	
	Cobalt sample:	^{60}Co: 5.5×10^{10} MSU calib.
		^{59}Fe: 8.8×10^{9} MSU calib.
	^{60}Fe sample:	^{60}Fe: 3.01×10^{12} MSU calib.
Mar. 12, 2009:	First measurement of 60Co and 59Fe activities at ND. All samples measured at 1 cm, 8 cm, and 14 cm. Background and calibration measurements between each measurement.	
	Cobalt sample:	^{60}Co: 5.4×10^{10} (decay since impl. i.e. expected if 100% impl.), 5.1×10^{10} (from decay counting)
		^{59}Fe: 3.9×10^{9} (decay since impl. i.e. expected if 100% impl.), 3.3×10^{9} (from decay counting)

	This high ^{60}Co concentration in the sample (from nuclear reactions in the target foil) make a chemical separation absolutely necessary. The difference in measuring from decay to expected from implanted gives us a control over ions lost to nuclear reactions during implantation.
Apr. 2009:	Begin of 60Fe standards preparation at University of Jerusalem. Material from PSI beam stop. Initial dilution by Munich group.
Apr. 30, 2009:	Shipping of samples to ANL.
May 6, 2009:	Arrival at ANL and activity measurement at ANL counting station of all samples.
May 21, 2009:	Completion of sample extraction and first 60Co separation at ANL. Losses as determined by chemistry group (4.7%, 8.8%, 4.6%).
May 22-26, 2009:	Post chemistry activity measurement at ANL. Separation of ^{60}Fe sample in 10% and 90% samples. This was deemed necessary in order to independently determine the number of ^{60}Fe atoms in the samples using AMS on the 10% sample. Activity measurement will be made on the 90% sample.
June 1, 2009:	Return of samples to ND.
June-July 2009:	Repeat activity measurement of all samples at ND and full gamma detector efficiency measurement (this was deemed necessary due to discrepancies between chemistry-determined losses and activity-determined losses). Losses as determined by ^{59}Fe activity measurement (12%, 10%, 10%).
	Reduction of ^{60}Co was measured to be 96.8%. This factor of 30 in ^{60}Co reduction was deemed insufficient and a second round of ^{60}Co was planned.
July 31, 2009:	Meeting at ND with Andreas Stolz to compare data analysis results.
August 10, 2009:	Summary of all gamma ray measurements present by M. Bowers prior to resending samples to ANL for second ^{60}Co reduction.

September 10, 2009:	Shipment of samples back to ANL.
September 21, 2009:	Delivery of ^{60}Fe standards prepared by M. Paul at the University of Jerusalem.
October 2, 2009:	Meeting at ANL to discuss next ^{60}Co reduction steps as well as making of ^{60}Co, ^{59}Fe, and ^{55}Fe standards and point sources. In order to obtain an AMS measurement on the 10% sample of ^{60}Fe independent of the Munich standards, it was decided to spike the full ^{60}Fe sample with a known quantity of ^{59}Fe and ^{55}Fe prior to ^{60}Co separation. Also meeting with D. Graczk in Chemistry division to discuss further ^{60}Co separation.
November 3-8, 2009:	Start of the ^{60}Fe beam development at ND for AMS measurements.
December 16, 2009;	Shipment of samples and standards from physics division to chemistry division for second ^{60}Co separation. Wet recombination of 10% and 90% samples into single sample.
January 22, 2009:	Completion of chemistry.
January 25, 2009:	Shipment of samples back to physics division. Separation of ^{60}Fe samples in 10% and 90%.

Chemistry Procedures

Three samples were produced at MSU in January 2009:

^{60}Fe sample (1-3)	3.01×10^{12}	^{60}Fe atoms implanted.
^{60}Co sample (3-3)	5.5×10^{10}	^{60}Co atoms implanted.
	8.8×10^{9}	^{59}Fe atoms implanted.
Test (AMS) Sample (2-3)	5.65×10^{10}	^{60}Fe atoms implanted.

(1-3),(2-3), and (3-3) denominations were the numbering used in the chemistry.

First chemistry at ANL (extraction of iron atoms from Al foils followed by ^{60}Co reduction chemistry) was chemically identical for all samples.

During the chemistry, stable iron carrier was added to all samples:

^{60}Fe sample (1-3):	500 mg Fe to obtain an isotopic ratio of 5×10^{-10}
^{60}Co sample (3-3):	500 mg Fe.
Test sample (2-3):	1000 mb Fe to obtain an isotopic ratio of 5×10^{-12}

Losses during chemistry were estimated both by weight and independently by measurement of the 1099 keV ^{59}Fe gamma ray line before and after chemistry. This latter measurement shows larger losses. However, the change in geometry of the sample probably accounts for these. The ^{60}Fe sample was also separated into two samples, one 10% of the total weight and one 90% of the total weight.

	By weight	By activity
^{60}Fe sample (1-3):	4.66%	12.38%
^{60}Co sample (3-3):	4.39%	9.86%
Test sample (2-3):	8.76%	—

First round of chemistry (May 21, 2009):

Natural iron was added by dispensing mass aliquots of an iron solution prepared form ACS Reagent Grade ferric chloride hexahydrate to beakers in which the aluminum foils would be dissolved. Two aliquots were dispensed for use in standardizing the iron solution using a gravimetric method based on precipitating the iron with ammonium hydroxide, collecting the ferric hydroxide precipitate by filtering and igniting the precipitate to Fe_2O_3 for weighing. The Duplicate standardizations agreed to within about 0.1% relative.

Each Al foil was added to a beaker containing the natural iron spike aliquot and then was dissolved in the beaker. Iron was separated from aluminum and cobalt by anion exchanged chromatography. The iron fraction was then precipitated with ammonia, collected on a filter and then ignited to Fe_2O_3 in a used silica beaker.

The mass of the recovered oxide was determined as the difference between the beakers mass after ignition and the empty beaker mass. Two of the samples (1-3 and 2-3) gave 100.14 and 100.09% recovery of the iron added. The other two gave slightly high recoveries (101.8 and 102.6%). There was no good explanation given by the chemists. Possible explanations included either static charge affecting the weighing of the beakers or some unanticipated impurity that followed the iron through the process.

Finally the oxide from the beaker was transferred to weighed glass vials. Complete transfer of the oxide is not possible. Relative to the amounts of iron added to each sample, the vials contained 91 to 96% of the starting material:

(1-3):	95.39%
(2-3):	91.24%
(3-3):	95.61%
Blank:	92.89%

Reduction of the ^{60}Co was determined by comparing the cobalt activity before and after the chemistry. Reduction was determined to by 96.8%. This factor of 30 in cobalt reduction was insufficient and a second round of cobalt reduction was done. For this chemistry, the 10% and 90% samples were recombined.

Second round of chemistry (January 25, 2009):

During this chemistry round, the samples were also spiked with ^{55}Fe and ^{59}Fe. The samples are as listed:

a) 60Fe sample (1-3): spiked with 10nCi ^{55}Fe and 20 nCi ^{59}Fe and treated by ion exchange to remove ^{60}Co.

b) Test sample (2-3): spiked with 10nCi ^{55}Fe and 20nCi ^{59}Fe and treated by ion exchange to remove ^{60}Co.

c) 60Co sample (3-3): treated by ion exchange to remove ^{60}Co.

d) 500 mg Fe sample spiked with 10nCi ^{60}Co and then taken through ion exchange to remove the cobalt.

e) 450 mg Fe sample spiked with 10nCi ^{60}Co, precipitated and ignited for use as a ^{60}Co counting standard.

f) 500 mg Fe sample spiked with 20nCi ^{59}Fe, precipitated, and ignited for use as a ^{59}Fe counting standard.

APPENDIX C

ACCELERATOR MASS SPECTROMETRY DATA

In this chapter, the raw data for the Accelerator Mass Spectrometry (AMS) experiment is given in Table C.1 for the November 2015 experiment and Table C.2 for the May 2016 experiment. Each row is an individual run. The Sample column is the name of the sample for the run including "Background" (done with a blank, Fe_2O_3 powder), "Fe-4" (PSI sample, standard material), and "Fe-1" (PSI sample, unknown material). The Time column is the live time for each run. The Initial ^{56}Fe and Final ^{56}Fe are the current reads in nanoAmperes at the Faraday cup located just after the low energy magnet. This two values are averaged and converted to particles per second in the Average ^{56}Fe column. The Transmission column shows the transmission for ^{56}Fe before and after the set of six runs. This transmission is measured as a percentage of the beam current from the ion source that reaches the Faraday cup at the Scattering Chamber before the spectrograph magnet, accounting for the change in charge state. The Total Counts column is the number of counts in the region of interest after the cuts have been made on the data. The Raw Concentration is calculated in the last column using an average of the two transmission measurements. This value of the concentration per run is a raw value and has not been scaled for any standard material. For the final analysis, the time and the counts were totaled together for each six runs on a sample. The average currents at the start and end of the set were used and the average transmission before and after each set was also used.

TABLE C.1

RAW ACCELERATOR MASS SPECTROMETRY DATA FROM NOVEMBER 2015

Sample	Time (second)	Initial ^{56}Fe (nA)	Final ^{56}Fe (nA)	Average ^{56}Fe (pps)	Trans. (%)	Total Counts	Raw Concentration ^{60}Fe/^{56}Fe
Background	277.758	60.080	57.980	3.6894×10^{11}	0.540	0	0.000
	277.902	57.980	56.711	3.5841×10^{11}		0	0.000
	278.307	56.711	55.899	3.5191×10^{11}		3	5.739×10^{-12}
	277.780	55.899	55.009	3.4659×10^{11}		2	3.892×10^{-12}
	278.214	55.009	54.729	3.4293×10^{11}		1	1.964×10^{-12}
	278.177	54.729	54.161	3.4028×10^{11}	0.527	2	3.959×10^{-12}
Fe-4	267.639	1.473	1.348	8.8143×10^{9}	0.411	5	5.200×10^{-10}
	270.486	1.458	1.310	8.6474×10^{9}		11	1.154×10^{-9}
	271.713	1.310	1.269	8.0582×10^{9}		9	1.008×10^{-9}
	274.751	1.269	1.260	7.9024×10^{9}		8	9.040×10^{-9}
	275.484	1.260	1.227	7.7708×10^{9}		5	5.730×10^{-9}
	276.169	1.227	1.219	7.6423×10^{9}	0.404	4	4.650×10^{-9}
Fe-1	291.540	3.746	3.828	2.3670×10^{10}	0.581	29740	7.922×10^{-7}
	291.463	3.828	3.841	2.3966×10^{10}		30122	7.926×10^{-7}
	292.830	3.841	3.811	2.3913×10^{10}		28977	7.607×10^{-7}
	292.294	3.811	3.831	2.3882×10^{10}		29618	7.799×10^{-7}
	292.486	3.831	3.826	2.3929×10^{10}		29846	7.839×10^{-7}
	292.917	3.826	3.768	2.3730×10^{10}	0.507	28674	7.582×10^{-7}
Background	274.824	67.012	65.858	4.1522×10^{11}	0.538	3	4.911×10^{-12}
	275.373	65.858	65.303	4.0988×10^{11}		1	1.655×10^{-12}
	275.477	65.303	64.840	4.0670×10^{11}		1	1.667×10^{-12}
	274.782	64.840	63.725	4.0176×10^{11}		0	0.000
	275.523	63.725	63.886	3.9878×10^{11}		1	1.700×10^{-12}
	275.236	63.886	63.396	3.9775×10^{11}	0.532	2	3.413×10^{-12}
Fe-4	279.432	1.259	1.150	7.5283×10^{9}	0.453	9	1.009×10^{-9}
	279.979	1.150	1.101	7.0337×10^{9}		8	9.578×10^{-10}
	281.537	1.101	1.072	6.7890×10^{9}		9	1.110×10^{-9}
	281.235	1.072	1.049	6.6278×10^{9}		7	8.855×10^{-10}
	282.022	1.049	1.027	6.4865×10^{9}		9	1.160×10^{-9}
	282.604	1.027	1.017	6.3851×10^{9}	0.395	5	6.533×10^{-10}
Fe-1	292.481	3.049	3.220	1.9590×10^{10}	0.538	24982	8.462×10^{-7}
	292.398	3.220	3.281	2.0316×10^{10}		25813	8.434×10^{-7}
	293.184	3.281	3.288	2.0528×10^{10}		25907	8.355×10^{-7}
	292.227	3.290	3.284	2.0543×10^{10}		26045	8.420×10^{-7}
	293.296	3.284	3.235	2.0370×10^{10}		25366	8.240×10^{-7}
	293.566	3.235	3.214	2.0151×10^{10}	0.492	25450	8.350×10^{-7}

TABLE C.2

RAW ACCELERATOR MASS SPECTROMETRY DATA FROM MAY 2016

Sample	Time (second)	Initial ^{56}Fe (nA)	Final ^{56}Fe (nA)	Average ^{56}Fe (pps)	Trans. (%)	Total Counts	Raw Concentration ^{60}Fe/^{56}Fe
Fe-4	285.990	81.127	74.864	4.868×10^{11}	0.696	107	1.105×10^{-10}
	282.784	75.748	76.832	4.762×10^{11}		110	1.174×10^{-10}
	296.034	76.832	76.353	4.781×10^{11}		111	1.128×10^{-10}
	281.408	76.353	78.368	4.828×10^{11}		126	1.333×10^{-10}
	276.331	78.368	79.016	4.912×10^{11}		140	1.483×10^{-10}
	296.688	79.016	78.436	4.914×10^{11}		152	1.499×10^{-10}
	277.915	78.436	76.413	4.832×10^{11}		131	1.402×10^{-10}
	296.495	76.413	75.213	4.732×10^{11}		140	1.434×10^{-10}
	275.711	75.213	75.972	4.718×10^{11}	0.784	139	1.362×10^{-10}
Fe-1	94.508	93.190	96.705	5.926×10^{11}	0.719	67232	1.671×10^{-7}
	94.217	96.705	100.761	6.162×10^{11}		68126	1.633×10^{-7}
	93.303	100.761	102.767	6.352×10^{11}		68429	1.607×10^{-7}
	93.418	102.767	105.112	6.487×10^{11}		69065	1.586×10^{-7}
	92.404	105.112	107.394	6.632×10^{11}	0.742	71781	1.58×10^{-7}
Fe-4	294.407	76.136	73.599	4.67×10^{11}	0.755	647	6.229×10^{-10}
	278.093	73.599	73.103	4.578×10^{11}		626	6.512×10^{-10}
	294.521	73.103	75.546	4.639×10^{11}		636	6.165×10^{-10}
	295.483	75.547	78.786	4.816×10^{11}		636	5.919×10^{-10}
	254.764	78.786	78.571	4.911×10^{11}	0.741	681	7.347×10^{-10}
Fe-1	16.359	62.9479	62.652	3.92×10^{11}	0.724	35330	7.613×10^{-7}
	15.846	62.652	63.2567	3.929×10^{11}		33836	7.508×10^{-7}
	16.362	63.256	62.8892	3.937×10^{11}		34361	7.37×10^{-7}
	16.319	62.882	62.1044	3.901×10^{11}	0.778	34094	6.888×10^{-7}
Fe-4	298.337	25.907	25.2349	1.596×10^{11}	0.793	257	6.807×10^{-10}
	298.139	25.235	25.6403	1.588×10^{11}		223	5.941×10^{-10}
	296.793	25.640	26.4658	1.626×10^{11}		271	7.081×10^{-10}
	298.172	26.466	26.3273	1.648×10^{11}		244	6.264×10^{-10}
	265.210	26.327	24.7857	1.595×10^{11}	0.762	237	7.35×10^{-10}
Fe-1	70.871	56.552	57.2524	3.552×10^{11}	0.815	125345	6.109×10^{-7}
	70.553	57.252	56.2684	3.543×10^{11}		129581	6.36×10^{-7}
	70.591	56.268	57.5478	3.552×10^{11}		126833	6.206×10^{-7}
	70.347	57.548	59.9422	3.667×10^{11}		127425	6.061×10^{-7}
	71.334	59.942	56.7295	3.641×10^{11}		119429	5.641×10^{-7}
	71.802	56.729	58.5039	3.596×10^{11}	0.787	117403	5.779×10^{-7}

APPENDIX D

ACTIVITY DATA

In this chapter, the raw data for the activity measurement described in Chapter 5 is given in Table D.1. The Source column gives the name of the sample measured. ^{241}Am refers to the efficiency calibration source. The ^{60}Fe, Fe-1 source refers to the point source made out of the remaining liquid Fe-1 sample discussed in details in Chapter 3. Two HPGe planar detectors were used for this measurement and they are label as "1" and "2" for this table. The background subtracted counts are in the Corrected Counts column. The total live time is given in seconds. The detector efficiency calculated for each detector is given in the Efficiency column and factors into the Activity of the ^{60}Fe, Fe-1 sample in the final column.

TABLE D.1

DATA FOR THE ^{241}AM EFFICIENCY AND THE FE-1 ^{60}FE SOURCES

Source	Detector	Corrected Counts	Time (sec)	Efficiency (%)	Activity (Bq)
^{241}Am	1	635977.18	3600	13.078	x
	2	608503.4	3600	12.513	x
^{60}Fe, Fe-1	1	1755.1	512471	x	1.268
	2	1623.83	513480	x	1.224
^{241}Am	1	1229954.2	7100	12.825	x
	2	1264066.1	7098	13.184	x
^{60}Fe, Fe-1	1	1682.82	512685	x	1.240
	2	1595.51	513410	x	1.142
^{241}Am	1	667060.18	3600	13.718	x
	2	612685.56	3600	12.600	x
^{60}Fe, Fe-1	1	1963.21	512864	x	1.351
	2	1724.61	513451	x	1.291
^{241}Am	1	641133.09	3600	13.185	x
	2	623244.04	3600	12.817	x
^{60}Fe, Fe-1	1	1749.73	513147	x	1.252
	2	1608.27	513005	x	1.185
^{241}Am	1	654958.27	3600	13.469	x
	2	625883.51	3600	12.872	x
^{60}Fe, Fe-1	1	1874.29	513093	x	1.313
	2	1599.52	513350	x	1.172
^{241}Am	1	680885.64	3600	14.003	x
	2	628743.35	3600	12.931	x
^{60}Fe, Fe-1	1	1873.1	512455	x	1.264
	2	1656.99	513240	x	1.209
^{241}Am	1	681887.15	3600	14.024	x
	2	621374	3600	12.779	x
^{60}Fe, Fe-1	1	2008.28	510469	x	1.359
	2	1812.82	513547	x	1.338
^{241}Am	1	680876.08	3600	14.003	x
	2	624441.85	3600	12.843	x
^{60}Fe, Fe-1	1	2048.55	511611	x	1.385
	2	1572.25	513242	x	1.155
^{241}Am	1	709689.24	3600	14.596	x
	2	596024.08	3600	12.258	x
^{60}Fe, Fe-1	1	1938.55	512547	x	1.255
	2	1800.48	513901	x	1.384
^{241}Am	1	483099.25	3600	9.936	x
	2	450777.97	3600	9.272	x
^{60}Fe, Fe-1	1	1370.19	512806	x	1.302
	2	1355	514823	x	1.375

BIBLIOGRAPHY

1. Accelerator Mass Spectrometry. http://www.physics.helsinki.fi/tutkimus/mat/ionisadelaboratorio/ams. Accessed on March 16, 2016.

2. Stellar Evolution. http://frigg.physastro.mnsu.edu/ eskridge/astr101/week8_3.html. Accessed on March 9, 2016.

3. Stars and Nebulae. http://skyserver.sdss.org/dr1/en/astro/stars/stars.asp. Accessed on April 27, 2015 from the Sloan Digital Sky Survey website.

4. L. W. Alvarez and R. Cornog. he^3 in helium. *Phys. Rev.*, 56:379–379, Aug 1939. doi: 10.1103/PhysRev.56.379.2. URL http://link.aps.org/doi/10.1103/PhysRev.56.379.2.

5. M. Basunia. Nuclear Data Sheets for A = 237. *Nuclear Data Sheets*, 107 (8):2323 – 2422, 2006. ISSN 0090-3752. doi: http://dx.doi.org/10.1016/j.nds.2006.07.001. URL http://www.sciencedirect.com/science/article/pii/S0090375206000585.

6. N. Benítez, J. Maíz-Apellániz, and M. Canelles. Evidence for Nearby Supernova Explosions. *Physical Review Letters*, 88(081101), 2002.

7. S. Bishop, P. Ludwig, R. Egli, T. Faestermann, G. Korschinek, and G. Rugel. Search for supernova 60Fe in the Earth's microfossil record. *American Institute of Physics Conference Proceedings*, 1484(63), 2012.

8. M. Bizzarro, D. Ulfbeck, A. Trinquier, K. Thrane, J. N. Connelly, and B. S. Meyer. Evidence for a Late Supernova Injection of ^{60}Fe into the Protoplanetary Disk. *Science*, 316(5828):1178–1181, 2007. doi: 10.1126/science.1141040. URL http://www.sciencemag.org/content/316/5828/1178.abstract.

9. L. Bouchet, E. Jourdain, and J.-P. Roques. Observation of the ^{26}Al Emission Distribution Throughout the Galaxy with INTEGRAL/SPI. *Proceedings of Science-34th International Cosmic Ray Conference*, ICRC2015(896), 2015.

10. E. Browne and J. Tuli. Nuclear Data Sheets for A = 60. *Nuclear Data Sheets*, 114(12):1849 – 2022, 2013. ISSN 0090-3752. doi: http://dx.doi.org/10.1016/j.nds.2013.11.002. URL http://www.sciencedirect.com/science/article/pii/S0090375213000823.

11. E. Browne and J. K. Tuli. Nuclear Data Sheets for A=137. *Nuclear Data Sheets*, 108:2173–2318, 2007.

12. E. M. Burbidge, G. R. Burbidge, W. A. Fowler, and F. Hoyle. Synthesis of the Elements in Stars. *Reviews of Modern Physics*, 29(4):547, 1957.

13. D. Darling. s-process. http://www.daviddarling.info/encyclopedia/S/s-process.html. Accessed on January 13, 2016.

14. J. Ellis, B. Fields, and D. N. Schramm. Geological Isotope Anomalies as Signatures of Nearby Supernovae. *The Astrophysical Journal*, 470:1227–1236, 1996.

15. B. D. Fields and J. Ellis. On deep-ocean Fe-60 as a fossil of a near-earth supernova. *New Astronomy*, 4, 1999.

16. L. Fimiani, D. L. Cook, T. Faestermann, J. M. G. Guzmán, K. Hain, G. F. Herzog, K. Knie, G. Korschinek, B. Ligon, P. Ludwig, J. Park, R. C. Reedy, and G. Rugel. Evidence for Deposition of Interstellar Material on the Lunar Surface. *45th Lunar and Planetary Science Conference Proceedings*, 1, 2014.

17. C. Fitousii, G. M. Raisbeck, K. Knie, G. Korschinek, T. Taestermann, S. Goriely, D. Lunney, M. Poutivtsev, G. Rugel, C. Waelbroeck, and A. Wallner. Search for Supernova-Produced 60Fe in a Marine Sediment. *Physical Review Letters*, 101 (121101), 2008.

18. R. Gehrke and J. Davidson. Acquisition of Quality γ-Ray Spectra with HPGe Spectrometers. *Applied Radiation and Isotopes*, 62(3):479 – 499, 2005. ISSN 0969-8043. doi: http://dx.doi.org/10.1016/j.apradiso.2004.07.005. URL `http://www.sciencedirect.com/science/article/pii/S0969804304004403`.

19. A. Group. A1900 schematic. `https://groups.nscl.msu.edu/a1900/overview/schematic.php`, 1 2009. Accessed on January 19, 2016.

20. J. Hubbell and S. Seltzer. Tables of X-Ray Mass Attenuation Coefficients and Mass Energy-Absorption Coefficients (version 1.4). *Online: http://physics.nist.gov/xaamdi [2014, November 13]*, 2004. URL `http://physics.nist.gov/xaamdi[2014,November13]`.

21. C. Iliadis. *Nuclear Physics of Stars*. Wiley-VCH Verlag GmbH and Co., 2007.

22. J. José and C. Iliadis. Nuclear asrophysics: the unfinished quest for the origin of the elements. *Reports on Progess in Physics*, 74, August 2011. doi: 10.1088/0034-4885/74/9/096901.

23. K. Knie, G. Korschinek, T. Faestermann, E. A. Dorfi, G. Rugel, and A. Wallner. ^{60}Fe. *Phys. Rev. Lett.*, 93:171103, Oct 2004. doi: 10.1103/PhysRevLett.93.171103. URL `http://link.aps.org/doi/10.1103/PhysRevLett.93.171103`.

24. G. F. Knoll. *Radiation Detection And Measurement*. John Wiley & Sons, Inc., 4 edition, 2010.

25. T. P. Kohman and M. S. Robison. Iron-60 as a Possible Heat Source and Chronometer in the Early Solar System. In *11th Conference on Lunar and planetary science*, number 1202, page 564, 1980.

26. K. S. Krane. *Introductory Nuclear Physics*. John Wiley & Sons, Inc., 2 edition, 1988.

27. W. Kutschera. Progress in Isotope Analysis at Ultra-Trace Level by AMS. *International Journal of Mass Spectrometry*, 242:145–160, 2005.

28. W. Kutschera, P. J. Billquist, D. Frekers, W. Henning, K. J. Jensen, M. Xiuzeng, R. Pardo, M. Paul, K. E. Rehm, R. K. Smither, J. L. Yntema, and L. F. Mausner. Half-life of ^{60}Fe. *Nuclear Instruments and Methods in Physics Research Section B: Beam Interactions with Materials and Atoms*, 5(2):430 – 435, 1984. ISSN 0168-583X. doi: http://dx.doi.org/10.1016/0168-583X(84)90555-X. URL `http://www.sciencedirect.com/science/article/pii/0168583X8490555X`.

29. R. M. Lindstrom, D. J. Lindstrom, L. A. Slaback, and J. K. Langland. A low-background gamma-ray assay laboratory for activation analysis. *Nuclear Instruments and Methods in Physics Research Section A: Accelerators, Spectrometers, Detectors, and Associated Equipment*, 299:425–429, 1990.

30. C.-H. Lyu and F. C. Bruhweiler. Time-dependent Ionization of H and He in the Local Interstellar Medium. *Astrophyscial Journal*, 459:216, 1996.

31. I. V. Moskalenko, A. W. Strong, S. G. Mashnik, and J. F. Ormes. Challenging Cosmic-Ray Propagation with Antiprotons: Evidence for a 'Fresh' Nuclei Component? *The Astrophysical Journal*, 586(2):1050, 2003. URL `http://stacks.iop.org/0004-637X/586/i=2/a=1050`.

32. R. A. Muller. Radioisotope Dating with a Cyclotron. *Science*, 196:489–494, April 1977.

33. R. A. Muller, L. W. Alvarez, W. R. Holley, and E. J. Stephenson. Quarks with Unit Charge: A Search for Anomalous Hydrogen. *Science*, 196:521–523, April 1977.

34. G. S. K. Murty, M. V. S. C. Rao, N. V. Rao, S. B. Reddy, G. Satyanarayana, D. L. Sastry, M. R. Iyer, and S. G. Sahasrabhude. Measurement of Conversion Coefficients of M3 Transition in ^{60m}Co and M4 Transition in ^{90m}Y. *Journal of Physics G: Nuclear and Particle Physics*, 15(11):1769, 1989. URL `http://stacks.iop.org/0954-3899/15/i=11/a=019`.

35. J. L. Orrell, C. E. Aalseth, I. J. Arnquist, T. A. Eggemeyer, B. D. Glasgow, E. W. Hoppe, M. E. Keillor, S. M. Morley, A. W. Myers, C. T. Overman, S. M. Shaff,

and K. S. Thommasson. Assay method for ^{238}U, ^{232}Th, and ^{210}Pb in lead and calibration of ^{210}Bi bremsstrahlung emission from lead. *Journal of Radioanalytical and Nuclear Chemistry*, pages 1–11, 2016. doi: 10.1007/s10967-016-4732-6.

36. M. Paul, B. G. Glagola, W. Henning, J. G. Keller, W. Kutschera, Z. Liu, K. E. Rehm, B. Schneck, and R. H. Siemssen. Heavy Ion Separtion with a Gas-Filled Magnetic Spectrograph. *Nuclear Instruments and Methods in Physics Research A*, 277:418–430, 1989.

37. F. Pleiter. Subshell Conversion Ratios for the {M3} Isomeric Transitions in 58mCo and in 60mCo. *Nuclear Physics A*, 163(2):425 – 431, 1971. ISSN 0375-9474. doi: http://dx.doi.org/10.1016/0375-9474(71)90499-4. URL `http://www.sciencedirect.com/science/article/pii/0375947471904994`.

38. D. Robertson. *New Measurement for the Astrophysically Important $^{40}Ca(\alpha,\gamma)^{44}Ti$ Reaction*. PhD thesis, The University of Notre Dame, 2010.

39. J.-C. Roy and T. P. Kohman. Iron 60. *Canadian Journal of Physics*, 35(5):649–655, 1957. doi: 10.1139/p57-069. URL `http://dx.doi.org/10.1139/p57-069`.

40. G. Rugel, T. Faestermann, K. Knie, G. Korschinek, M. Poutivtsev, D. Schumann, N. Kivel, I. Günther-Leopold, R. Weinreich, and M. Wohlmuther. New Measurement of the ^{60}Fe Half-Life. *Phys. Rev. Lett.*, 103:072502, Aug 2009. doi: 10.1103/PhysRevLett.103.072502. URL `http://link.aps.org/doi/10.1103/PhysRevLett.103.072502`.

41. R. Sayer. Semi-Empirical Formulas for Heavy-Ion Stripping Data. *Revue de Physique Appliquee*, 12:1543, October 1977.

42. B. Singh. Nuclear Data Sheets for A=1. *Nuclear Data Sheets*, 106:601–618, 2005.

43. R. K. Smith and D. P. Cox. Multiple Supernova Remnant Models of the Local Bubble and the Soft X-Ray Background. *The Astrophysical Journal Supplement Series*, 134(2):283, 2001. URL `http://stacks.iop.org/0067-0049/134/i=2/a=283`.

44. C. Tuniz, J. R. Bird, D. Fink, and G. F. Herzog. *Accelerator Mass Spectrometry: Ultrasensitive Analysis for Global Science*. CRC Press, LLC, 1998.

45. E. Uberseder, R. Reifarth, D. Schumann, I. Dillmann, C. D. Pardo, J. Görres, M. Heil, F. Käppeler, J. Marganiec, J. Neuhausen, M. Pignatari, F. Voss, S. Walter, and M. Wiescher. Measuremnt of the ^{60}Fe, n, γ, ^{61}fe(C, r)oss Section at Stellar Temperatures. *Physical Review Letters*, 102(151101), 2009.

46. A. Wallner, M. Bichler, K. Buczak, D. Fink, O. Forstner, R. Golser, M. A. C. Hotchkis, A. Klix, A. Krasa, W. Kutschera, C. Lederer, A. Plompen, A. Priller, D. Schumann, V. Semkova, and P. Steier. High-sensitivity isobar-free AMS measurements and reference material for ^{5}Fe, ^{68}Ge, and ^{202g}Pb. *Nuclear Instruments*

and Methods in Physics Research Section B: Beam Interactions with Materials and Atoms, 294:374–381, 2013.

47. A. Wallner, M. Bichler, K. Buzcak, R. Dressler, L. Fifield, D. Schumann, J. Sterba, S. Tims, G. Wallner, and W. Kutschera. Settling the Half-Life of ^{60}Fe: Fundamental for a Versatile Astrophysical Chronometer. *Physical Review Letters*, 114, 2015.

48. A. Wallner, J. Feige, N. Kinoshita, M. Paul, L. K. Fifield, R. Golser, M. Honda, U. Linnemann, H. Matsuzaki, S. Merchel, G. Rugel, S. G. Tims, P. Steier, T. Yamagata, and S. R. Winkler. Recent near-Earth supernovae probed by global deposition of interstellar radioactive ^{60}Fe. *Nature*, 532:69–72, 2016. doi: 10.1038/nature17196.

49. W. Wang, M. J. Harris, R. Diehl, H. Halloin, B. Cordier, A. W. Strong, K. Kretschmer, J. Knödlseder, G. Lichti, J. P. Rogques, S. Schanne, A. von Kienlin, G. Weidenspointer, , and C. Wunderer. SPI observations of the diffuse 60Fe emission in the Galaxy. *Astronomy and Astrophysics*, 49(3):1005–1012, 2007.

This document was prepared & typeset with pdfLaTeX*, and formatted with* NDdiss2$_\varepsilon$ *classfile (v3.2013[2013/04/16]) provided by Sameer Vijay and updated by Megan Patnott.*